Geofluids

Evaluation of Flow Chemistry in Porous Media in Drilling and Oil Recovery Processes

Lead Guest Editor: Daoyi Zhu
Guest Editors: Ze Wang, Shixun Bai, Wai Li, and Shiling Zhang

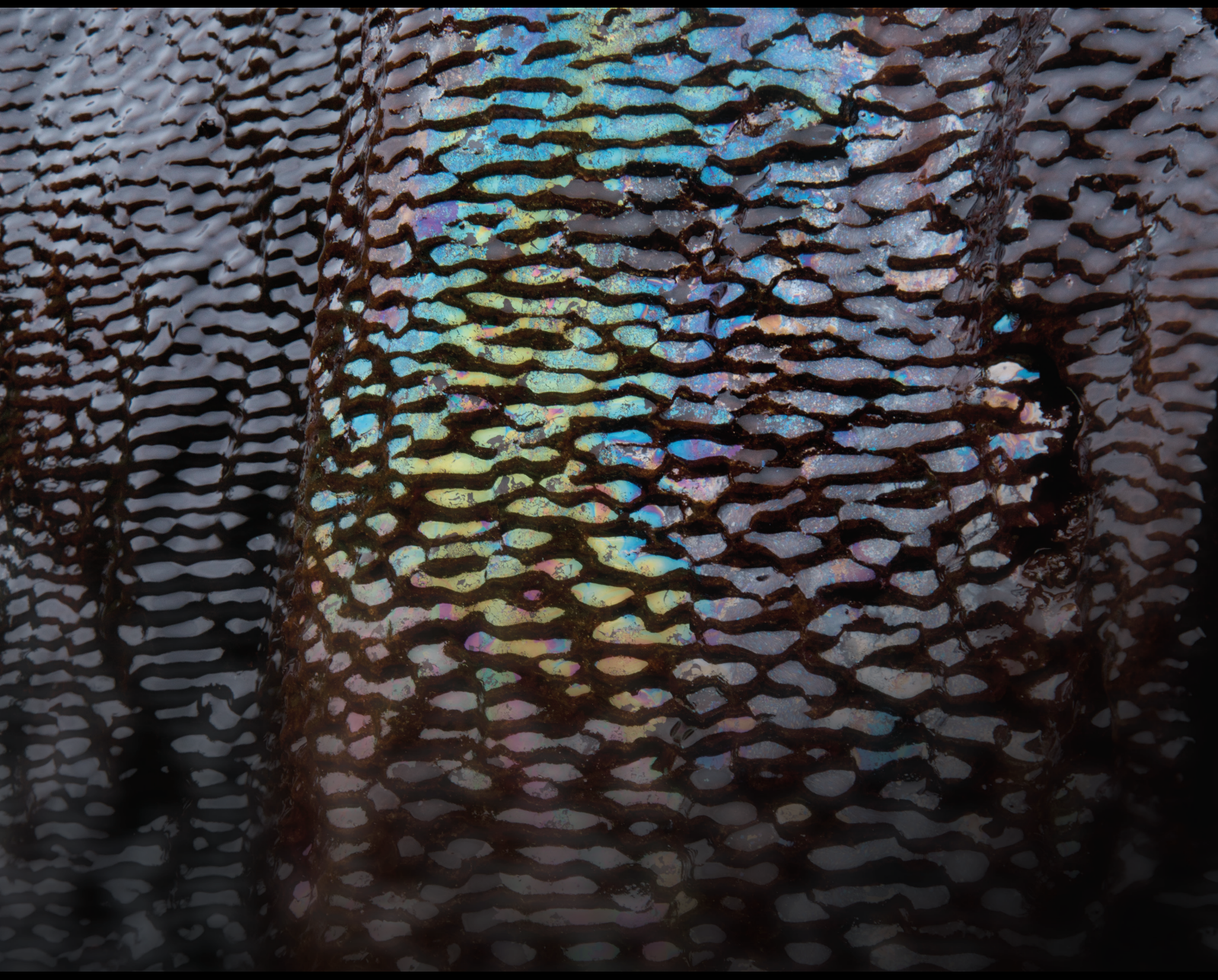

Evaluation of Flow Chemistry in Porous Media in Drilling and Oil Recovery Processes

Geofluids

Evaluation of Flow Chemistry in Porous Media in Drilling and Oil Recovery Processes

Lead Guest Editor: Daoyi Zhu
Guest Editors: Ze Wang, Shixun Bai, Wai Li, and Shiling Zhang

Chief Editor

Associate Editors

Academic Editors

Contents

Hindawi
Geofluids
Volume 2023, Article ID 9357711, 12 pages
https://doi.org/10.1155/2023/9357711

Research Article

Insights into Enhanced Oil Recovery by Coupling Branched-Preformed Particle Gel and Viscosity Reducer Flooding in Ordinary Heavy Oil Reservoir

Zongyang Li

Research Institute of Exploration and Development of Shengli Oilfield, SINOPEC, Dongying 257000, China

Correspondence should be addressed to Zongyang Li; lizongyang1108@163.com

Received 8 November 2022; Revised 16 December 2022; Accepted 27 March 2023; Published 30 June 2023

Academic Editor: Shixun Bai

Viscosity reducer flooding has been successfully applied in tertiary oil recovery of ordinary heavy oil reservoirs. However, lowering interfacial tension or reducing oil viscosity, which is more critical for viscosity reducer to improve oil recovery of ordinary heavy oil, has not yet formed a unified understanding, which restricts the further large-scale application of viscosity reducer flooding for ordinary heavy oil reservoir. Moreover, when the dominant water flow channel is formed in the reservoir, the sweep efficiency decreases sharply and can affect oil recovery efficiency of viscosity reducer. Therefore, in this study, the concept of branched-preformed particle gel (B-PPG) coupling viscosity reducer flooding is proposed. The oil-water interfacial tension performance, emulsification ability, and viscosity reduction performance of three different viscosity reducers were evaluated. The enhanced oil recovery ability of viscosity reducers, B-PPG, and viscosity reducer/B-PPG composite systems was investigated by performing sand pack flooding experiments. The results show that the oil-water interfacial tensions of the three viscosity reducers S1, S2, and S3 are 0.432 $mN{\cdot}m^{-1}$, 0.0112 $mN{\cdot}m^{-1}$, and 0.0031 $mN{\cdot}m^{-1}$, respectively. S1 with the highest interfacial tension has the best emulsification and viscosity reduction performance, S2 is the second, and S3 is the worst. The lower the interfacial tension, the worse the emulsification stability. The sand pack flooding results show that the incremental oil recovery of viscosity reducer S2 flooding is the largest, 7.5%, followed by S1, 7.3%, and S3, 5.6%. The viscosity reducer S2 with moderate interfacial tension and emulsifying capacity has the best ability to improve the recovery of ordinary heavy oil. The incremental oil recovery of B-PPG is 12.7%, which is significantly higher than that of viscosity reducer flooding. Compared with viscosity reducing flooding, the viscosity reducer/B-PPG composite systems have better enhanced oil recovery capacity. The findings of this study can help for better understanding of enhancing oil recovery for ordinary heavy oil reservoir.

1. Introduction

With the continuous development of petroleum industry, the proportion of heavy oil in the world's remaining oil resources is increasing. Heavy oil exploitation has a significant impact on the pattern of world oil production. However, heavy oil has the characteristics of high colloid and asphaltene content, high viscosity and density, and poor flow capacity, resulting in great difficulty and high production cost of recovering heavy oil [1–4]. For ordinary heavy oil reservoirs, due to adverse mobility ratio between water and oil, the fingering effect occurs and the oil recovery efficiency of conventional water flooding is low. To improve oil recovery efficiency of heavy oil reservoirs, thermal oil recovery technologies including steam huff and puff, steam flooding, and steam-assisted gravity drainage (SAGD) have been applied. The thermal oil recovery methods focus on reducing the viscosity of heavy oil by destroying the supramolecular structure between colloid and asphaltene in heavy oil and reducing the water-oil mobility ratio, which enlarges the sweep efficiency and improves oil recovery [5–11]. However, due to high consumption of energy and water to generate steam and severe heat loss, the thermal methods are economically nonprofitable for the deep and thin heavy oil

reservoirs [12–15]. Therefore, it is of great significance to change the development mode of ordinary heavy oil and achieve highly efficient development of ordinary heavy oil reservoir.

The nonthermal oil recovery technology, especially chemical flooding technology, has attracted more and more attention because of its wide reservoir application range and low economic cost, which has been successfully applied in many heavy oil reservoirs [16–23]. Viscosity reducing production is one of the most commonly used methods for recovering heavy oil in ordinary heavy oil reservoir. The main enhanced oil recovery (EOR) mechanisms for viscosity reducing production can be mainly divided into two aspects: On the one hand, through the emulsification of viscosity reducer under certain external force conditions, the heavy oil is dispersed into formation water and forms relatively stable O/W emulsion, which can greatly reduce the viscosity of heavy oil and improve its fluidity in porous media. On the other hand, it can effectively reduce the adhesion work by reducing the interfacial tension between oil and water, so as to reduce the flow resistance of crude oil and improve the oil displacement efficiency [24–26]. However, the two different EOR mechanisms including emulsifying viscosity reduction and lower oil-water interfacial tension, which is more critical for viscosity reducer to improve oil recovery of ordinary heavy oil, have not yet formed a unified understanding. Some researchers believe that the interfacial tension is the primary index to determine the performance of viscosity reducer. Lower interfacial tension can effectively reduce the residual oil saturation [27–30]. Some researchers also believe that the mechanism of emulsification and viscosity reduction is the key to greatly improve the recovery of ordinary heavy oil. The viscosity reducer with better emulsification ability and viscosity reduction performance has better EOR effect [31–33].

In addition, due to the high viscosity of heavy oil and water-oil mobility ratio, the viscosity reducer flooding is not satisfied. In order to reduce this deficiency, researchers have proposed combined flooding systems such as viscosity reducer/polymer or viscosity reducer/alkali [34–38]. Polymer can increase the viscosity of injection water and reduce water-oil mobility ratio and thus expand sweep volume. The alkali can react with crude oil to form in situ surfactant, which can promote the formation of O/W emulsion and reduce the viscosity. The formation of in situ surfactant can reduce oil-water interfacial tension and improve oil displacement efficiency. Alkali-containing systems often have serious scaling problems, which restricts the development of alkali/surfactant binary flooding [39–43]. The range of crude oil viscosity used in the conventional viscosity reducer/polymer combined system is limited, resulting in low recovery and unable to realize the efficient development of the conventional heavy oil reservoir. Moreover, when the dominant water flow channel is formed in the reservoir, the sweep efficiency decreases sharply and can affect the enhanced oil recovery ability.

Therefore, to improve the sweep efficiency, the branched-preformed particle gel (B-PPG) was developed by Shengli Oilfield, which has unique "partial crosslinking and partial branching" molecular structures. The B-PPG has viscoelastic properties, which can plug the dominant water flow channel, change the subsequent flow direction, and enlarge the swept volume. The B-PPG can have better sweep efficiency improvement ability than polymer solution [44–52]. Thus, in this study, the concept of branched-preformed particle gel (B-PPG) coupling viscosity reducer flooding is proposed firstly. To determine which mechanism dominates for viscosity reducer flooding and clarify EOR efficiency by coupling B-PPG and viscosity reducer, a series of experiments including physicochemical property evaluation of viscosity reducer and sand pack flooding experiments was systematically conducted in this study. Firstly, three different viscosity reducers with different interfacial tension and emulsification ability were collected. Then, the oil-water interfacial tension performance, emulsification performance, and viscosity reduction performance were studied. Finally, a series of sand pack flooding experiments was performed to investigate the EOR ability of three different viscosity reducers, B-PPG, and viscosity reducer/B-PPG composite systems. In general, we hope that this study can clarify the contribution of interfacial tension performance and emulsification performance of viscosity reducer to enhance oil recovery of common heavy oil and provide a new idea for enhancing oil recovery of common heavy oil.

Table 1: The ionic composition and concentration of formation brine.

Ionic composition	Na^+	Ca^{2+}	Mg^{2+}	Cl^-
Concentration ($mg{\cdot}L^{-1}$)	3667	292	65	6583

2. Materials and Methods

2.1. Materials. The viscosity reducers used in this study were nonionic surfactants (S1, S2, and S3) provided by Yangzhou Runda Co., Ltd. The B-PPG used in this study was the branched-preformed particle gel provided by Shengli Oilfield. The elastic modulus and median particle size (D50) of B-PPG were 4.3 Pa and 506.5 μm, respectively.

At 70°C, the density and viscosity of heavy oil obtained from Shengli Oilfield are 0.982 $g{\cdot}cm^{-3}$ and 2570 mPa·s, respectively. The ionic composition and concentration of simulated formation brine with TDS of 10607 $mg{\cdot}L^{-1}$ are listed in Table 1.

2.2. Methods

2.2.1. Oil-Water Interfacial Tension Measurement. The oil-water interfacial tension between three different viscosity reducers and degassed heavy oil in chen25 block of Shengli Oilfield was measured by spinning drop method on Texas-500c interface tension meter. The measured temperature was 70°C, and the rotating speed was 5000 $r{\cdot}min^{-1}$.

2.2.2. Emulsification Stability Evaluation. Emulsification stability is one of the important indexes to evaluate the performance of viscosity reducers. The emulsification stability is often determined by the water separating proportion referring to the percentage of the volume of water separated from

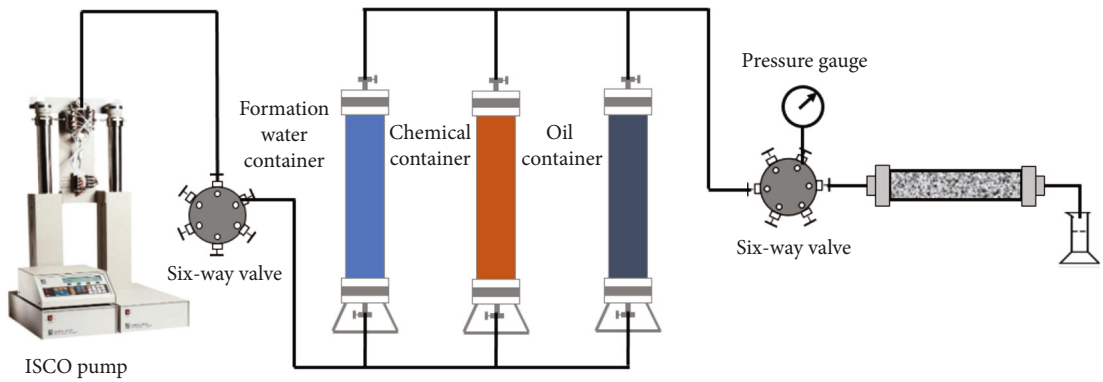

Figure 1: The schematic diagram of sand pack flooding experimental apparatus.

the emulsion. It is a commonly used quantitative evaluation index to evaluate the emulsification stability of viscosity reducers. The higher the water separating proportion, the worse the emulsification stability of viscosity reducer. The experimental procedures of emulsification stability evaluation were as follows: (1) The prepared viscosity reducer with concentration of 3000 mg·L^{-1} and heavy oil were placed in a 70°C oven for 2.0 h. (2) Then, according to the oil-water ratio of 3 : 7, the heavy oil and viscosity reducer solution were stirred with a homogenizer for 3 min at the speed of 3000 r·min^{-1} to form O/W emulsion. (3) The formed emulsion was placed in the 10 mL plugged test tube at 70°C constant temperature water bath and started timing at the same time. The position of oil-water interface and the volume of separated water in the test tube were recorded at regular intervals, and the water separating proportion of emulsion at different times was calculated according to the following equation:

$$f_1 = \frac{V_w}{V_0}, \quad (1)$$

where f_1 is the water separating proportion (%), V_w is the water separating volume (mL), and V_0 is the initial water volume (mL).

2.2.3. The Viscosity Reduction Ability Evaluation. Different viscosity reducer (S1, S2, and S3) solutions with concentration of 3000 mg·L^{-1} were prepared by simulated formation brine. Then, according to the oil-water ratio of 3 : 7, the predetermined amount of surfactant and heavy oil was stirred with a homogenizer for 3 min at different speeds of 500 r·min^{-1}, 1000 r·min^{-1}, and 3000 r·min^{-1} to form emulsion. At 70°C, the viscosity of formed emulsion was measured by Brookfield DV-II viscometer, and the viscosity reduction rate of heavy oil emulsification at this time was calculated according to the following equation:

$$f_2 = \frac{\mu_0 - \mu}{\mu_0}, \quad (2)$$

where f_2 is the viscosity reduction rate (%), μ_0 is the viscosity of heavy oil (mPa·s), and μ is the viscosity of formed emulsion (mPa·s).

Table 2: The porosity and permeability of sand packs used for flooding experiments.

No.	Chemical slug	Permeability (μm^2)	Porosity (%)
1#	3000 mg·L^{-1} S1	1.1	42.2
2#	3000 mg·L^{-1} S2	1.1	41.4
3#	3000 mg·L^{-1} S3	1.0	40.8
4#	800 mg·L^{-1} B-PPG	1.0	40.8
5#	3000 mg·L^{-1} S1+800 mg·L^{-1} B-PPG	1.0	40.8
6#	3000 mg·L^{-1} S2+800 mg·L^{-1} B-PPG	1.0	41.4
7#	3000 mg·L^{-1} S3+800 mg·L^{-1} B-PPG	0.9	40.8

2.2.4. The Morphology of Formed Emulsion Observation. To grasp a better understanding on the mechanism of surfactant emulsification and viscosity reduction, the morphology of formed emulsion at different rotating speeds was studied by optical microscope. The Axioskop 40 microscope (Carl Zeiss) enables us to analyze samples placed between slide and cover glass under ordinary light and polarized light.

The experimental procedures were as follows: (1) The viscosity reducer solution and crude oil were placed in an incubator water bath at 70°C for 3 h. (2) Then, heavy oil and viscosity reducer solution was mixed evenly according to the oil-water ratio of 3 : 7 and emulsified it with a dispersion homogenizer at different speeds of 500 r/min, 1000 r/min, and 3000 r/min for 3 min. In the emulsification process, the beaker was placed in a 70°C constant temperature water bath. (3) The formed emulsion was placed on the glass slide, and the morphology of the emulsion was observed by microscope.

2.2.5. Sand Pack Flooding Experiment. In order to investigate the EOR ability of three different viscosity reducers, B-PPG and coupling B-PPG, and viscosity reducers, a series of sand pack flooding experiments was carried out. Figure 1 depicts the schematic diagram of sand pack flooding oil

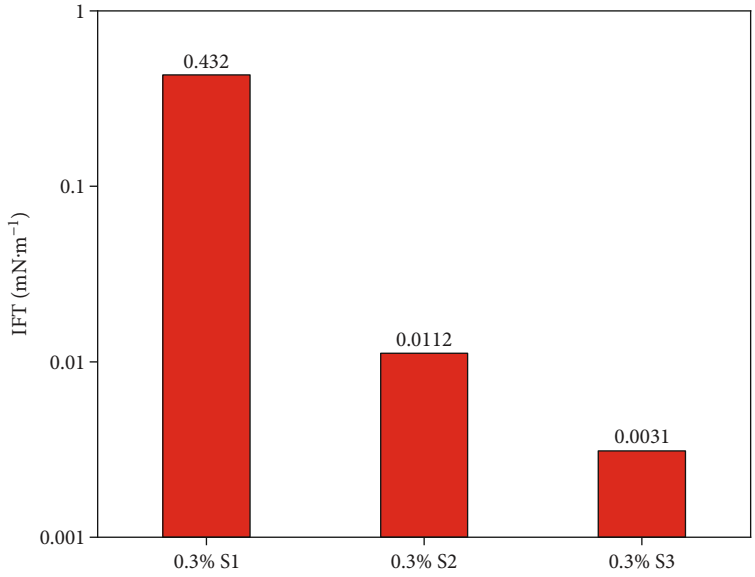

Figure 2: IFT between different viscosity reducers and heavy oil.

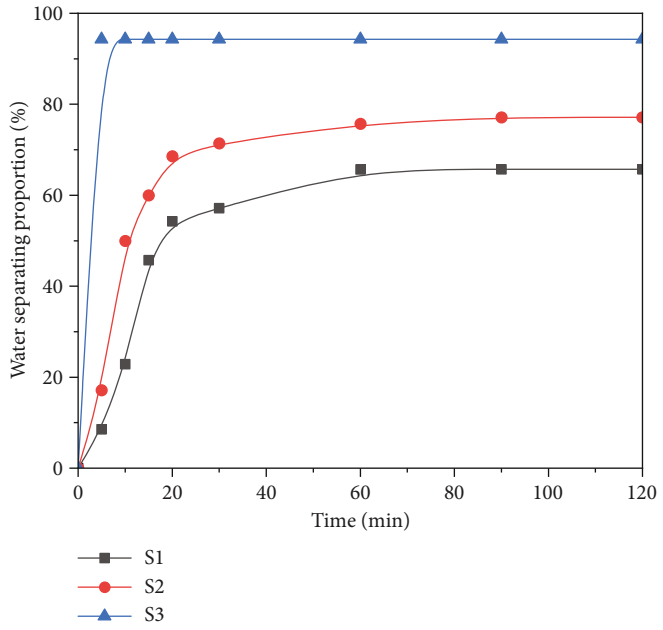

Figure 3: The water separating proportion of different viscosity reducers versus time.

experimental apparatus. The flooding experiments were carried out at 70°C and atmospheric pressure. The experimental processes were as follows: (1) sand pack preparation and the measurement of permeability: the sand pack was filled with 120~140 mesh quartz sand by wet packing method, and the liquid permeability was measured at the water flooding rate of 1.0 mL/min; (2) crude oil saturation period: the wet-packed sand pack was flooded with crude oil at the rate of 0.1 mL/min until complete oil production at 80°C. Then, the sand pack was sealed and put in the oven at 70°C for aging for 48 h after saturated oil; (3) water flooding and chemical flooding period: the initial water flooding was conducted until the water cut reached 95% at the flooding rate of 0.3 mL/min. Then, 0.4 PV different chemical slugs were injected into the sand packs; (4) subsequent water flooding period: the subsequent water flooding was conducted until the water cut reached 98%. Then, the flooding experiments were terminated. The injection pressure and volume of produced water and oil were recorded at different flooding periods. Table 2 shows the porosity and permeability properties of sand packs used for flooding experiments.

Table 3: Viscosity reduction rate of three viscosity reducers at different shear rates at 70°C.

Chemical slug	Oil-water volume ratio	Shear rate ($r \cdot min^{-1}$)	Crude oil viscosity (mPa·s)	Emulsion viscosity (mPa·s)	Viscosity reduction rate (%)
S1	3 : 7	500	2570	272	89.4
S1	3 : 7	1000	2570	187	92.7
S1	3 : 7	3000	2570	46	98.2
S2	3 : 7	500	2570	421	87.6
S2	3 : 7	1000	2570	241	90.6
S2	3 : 7	3000	2570	127	95.1
S3	3 : 7	500	2570	/	/
S3	3 : 7	1000	2570	1110	56.8
S3	3 : 7	3000	2570	318	83.6

3. Results and Discussion

3.1. Performance Evaluation of Viscosity Reducer

3.1.1. Oil-Water Interfacial Tension Property. Viscosity reducer can play a role in reducing interfacial tension between water and oil. Lower interfacial tension can effectively reduce the adhesion work and capillary force, which can reduce the crude oil flow resistance and improve the oil displacement efficiency. Therefore, it is very important to study the interfacial tension between viscosity reducer and heavy oil. Texas-500c interfacial tension meter was used to measure the oil-water interfacial tension between three different viscosity reducers and degassed heavy oil in chen25 block of Shengli Oilfield by spinning drop method. The concentration of S1, S2, and S3 is 3000 $mg \cdot L^{-1}$, respectively. The measurement results are shown in Figure 2. The equilibrium interfacial tension between viscosity reducer S1 and heavy oil is the largest, 0.432 $mN \cdot m^{-1}$; S2 is the second, 0.0112 $mN \cdot m^{-1}$; and S3 is the lowest, 0.0031 $mN \cdot m^{-1}$.

3.1.2. The Emulsification Stability Evaluation. The key to heavy oil recovery is to improve the water-oil mobility ratio and improve the flow capacity of heavy oil in porous media. Viscosity reducer can disperse heavy oil in formation water to form O/W emulsion and effectively reduce the viscosity of crude oil. The stability of formed O/W emulsion can influence the viscosity reducing effect. The emulsification stability of a viscosity reducer is determined by the water separating proportion. The water separating proportion versus time of different viscosity reducers is depicted in Figure 3.

For three viscosity reducers S1 (10^{-1} $mN \cdot m^{-1}$), S2 (10^{-2} $mN \cdot m^{-1}$), and S3 (10^{-3} $mN \cdot m^{-1}$) with different magnitudes of interfacial tension, the water separating proportion increases until it is stable with the increase of time. The higher the water separating proportion is, the worse the stability of the emulsion is. For viscosity reducer S3, the water separating proportion exceeded 90% within 5 minutes, indicating that the stability of the emulsion is very poor, while the water separating proportion of S1 and S2 is significantly lower than that of S3, which has good stability. Moreover, the emulsifying stability of S1 is better than that of S2. The lower the interfacial tension is, the worse the emulsification stability is.

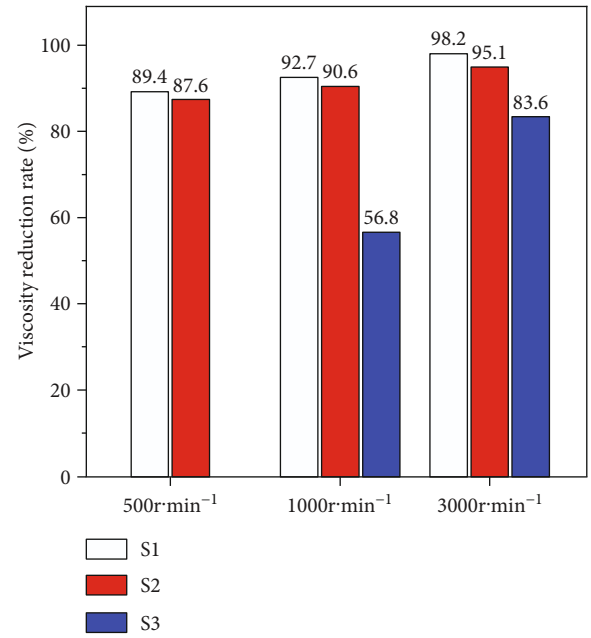

Figure 4: Viscosity reduction rate of three viscosity reducers at different shear rates at 70°C.

3.1.3. The Viscosity Reducing Ability Evaluation. Heavy oil is a typical non-Newtonian fluid; its viscosity is greatly affected by shear rate. Therefore, the viscosity reduction performance of the three viscosity reducers at different stirring speeds (500 $r \cdot min^{-1}$, 1000 $r \cdot min^{-1}$, and 3000 $r \cdot min^{-1}$) was evaluated. Table 3 and Figure 4 describe the viscosity reduction rates of the three viscosity reducers S1, S2, and S3 at different stirring speeds. The concentration of S1, S2, and S3 is 3000 $mg \cdot L^{-1}$, respectively.

When the stirring speed is 500 $r \cdot min^{-1}$, the emulsification stability of S3 emulsion is poor, and its viscosity reduction rate cannot be measured. When the viscosity reducer is constant, the viscosity reduction rate increases with the increase of stirring speed. When the stirring speed is constant, the viscosity reduction rates of S1 and S2 are significantly higher than that of S3. In general, the viscosity reduction rates of S1 and S2 at different stirring speeds are greater than 80%, while the viscosity reduction rate of S3 is more affected by the stirring speed.

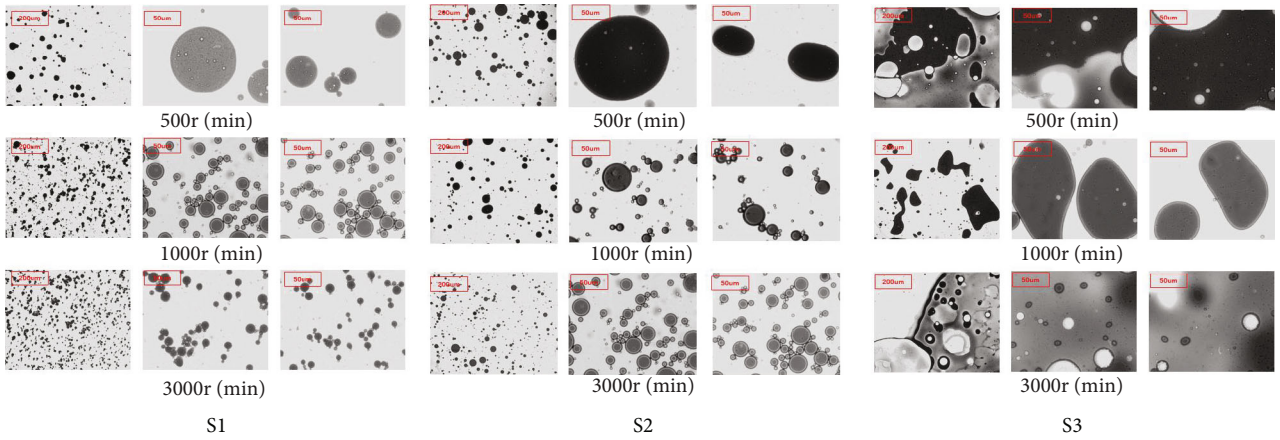

Figure 5: Microscopic images of heavy oil after emulsification by S1, S2, and S3.

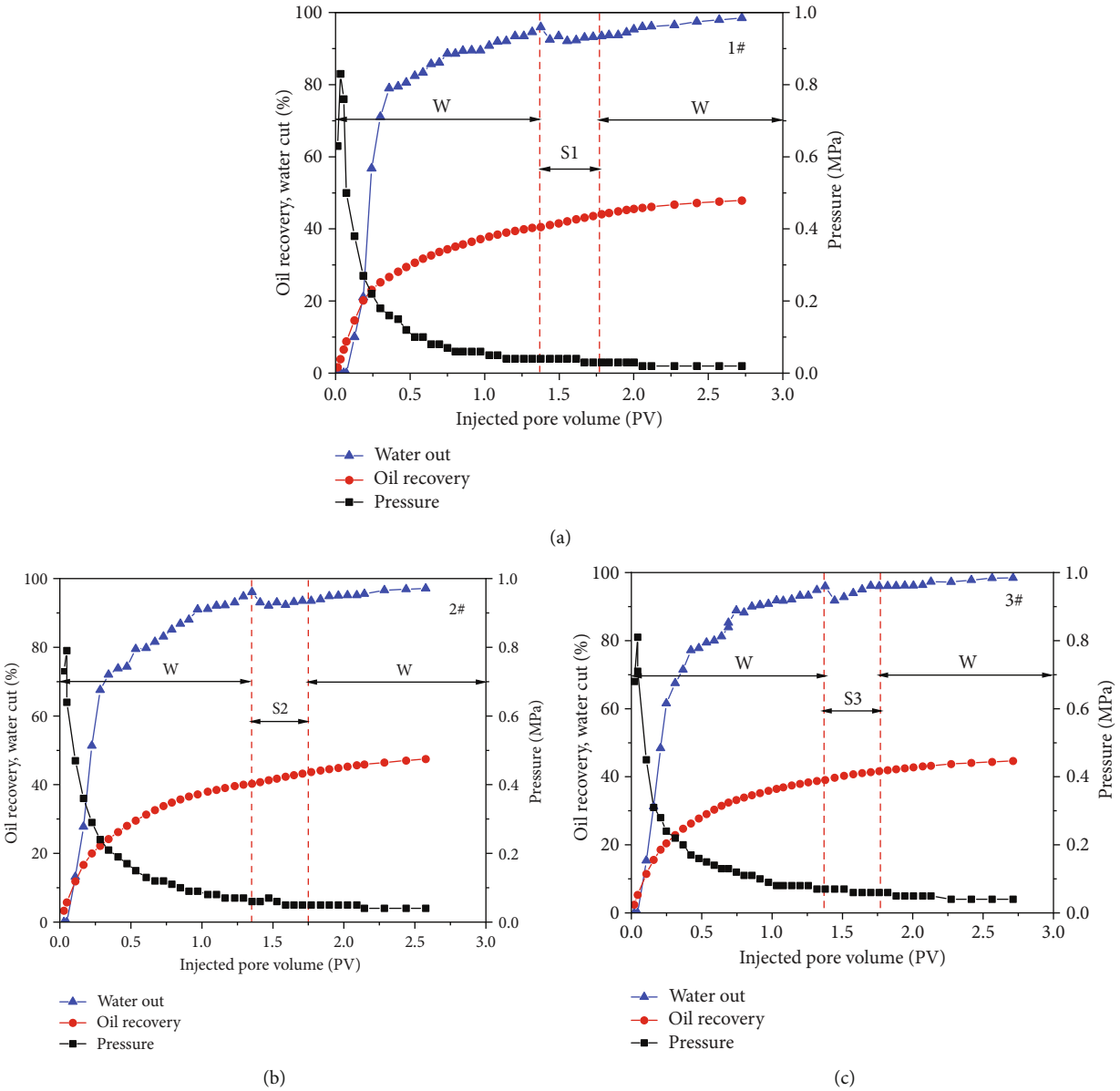

Figure 6: The oil recovery, water cut, and injection pressure versus pore volume: (a) S1 flooding; (b) S2 flooding; (c) S3 flooding.

Table 4: The incremental oil recovery results of viscosity reducer flooding at different flooding stages.

No.	Chemical slug	Water flooding recovery (%)	Chemical flooding recovery (%)	Incremental oil recovery (%)
1#	S1	40.6	47.9	7.3
2#	S2	40.3	47.8	7.5
3#	S3	39.1	44.7	5.6

3.1.4. The Morphology of Formed Emulsion Observation. The morphology of formed emulsion at different rotating speeds was studied by optical microscope. The microscopic images of emulsions formed by three viscosity reducers with different interfacial tensions are shown in Figure 5.

When the oil-water ratio is 3 : 7, 3000 mg·L^{-1} viscosity reducer S1 or S2 and heavy oil can form stable O/W emulsion under the conditions of 500 r·min^{-1}, 1000 r·min^{-1}, and 3000 r·min^{-1}, and the oil droplet size in the emulsion decreases with the increase of shear rate. Under the same shear rate, the oil droplet size in S1 emulsion is larger than that in S2. It shows that the emulsification and viscosity reduction performance of viscosity reducer S1 is better than S2, which is also consistent with the measurement results of the viscosity reduction rate in Section 3.1.2.

However, after fully mixing S3 and heavy oil at low shear rate, the morphology still showed oil block, oil mass, and oil-water separation. Until the shear rate reached 3000 r·min^{-1}, oil droplets can be observed in S3 emulsion, but the surface is still wrapped by an oil film, indicating that S3 has poor emulsifying ability and cannot make heavy oil reach a better emulsifying state.

Overall, the size of emulsion droplets varies significantly with the increase of stirring speed, and the size decreases with the increase of stirring speed. From the observation results, except S3, both S1 and S2 can form stable O/W emulsion, and the size of S2 is larger than S1, indicating that the emulsifying performance of S1 is better than S2 and S3, which is consistent with the evaluation results in Section 3.1.2. With the increase of stirring speed, the size decreases significantly and the number of small droplets increases, so that the dispersed phase is more evenly dispersed in the continuous phase. Therefore, compared with the viscosity of crude oil, the apparent viscosity of emulsion decreases sharply. The droplet size and dispersion effect of S1 and S2 emulsion are obviously better than that of S3, and the viscosity reduction effect of S3 is also the worst, which is consistent with the evaluation results of viscosity reduction rate in Section 3.1.3.

3.2. Enhanced Oil Recovery Ability

3.2.1. Analysis of Experimental Results of Viscosity Reducer Flooding. In order to study the ability of viscosity reducers with different interfacial tensions to improve the recovery of common heavy oil, a series of sand pack flooding experiments was carried out. The flooding curves of S1, S2, and S3 viscosity reducers are shown in Figure 6. The changes of injection pressure, water cut, and recovery with injection pore volume during viscosity reducer flooding with different interfacial tensions were analyzed.

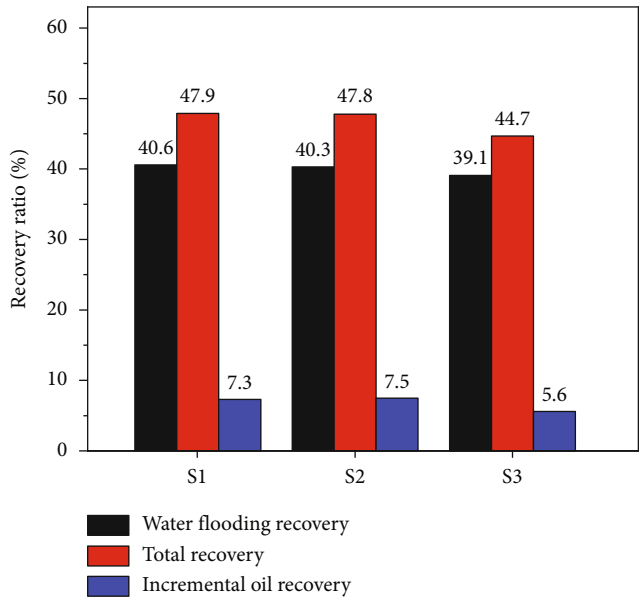

Figure 7: The incremental oil recovery results of viscosity reducer flooding at different flooding stages.

The flooding process is mainly divided into three stages: early water flooding stage, different chemical agent flooding stage, and subsequent water flooding stage. As shown in Figure 6, during the water flooding development stage, with the increase of injection pore volume, the injection pressure increases firstly and then decreases rapidly until it is stable after reaching the breakthrough pressure. The maximum pressure is in the range of 0.79 and 0.83 MPa, and the stable pressure of water flooding is in the range of 0.04~0.07 MPa. Moreover, with the increase of injected pore volume, the growth rate of water cut is fast in the early stage and slow in the later stage. When the injected pore volume is about 1.35 PV, the water cut reached 95%. The water flooding recovery is about 40%.

At the chemical flooding and subsequent water flooding stages, during the injection of three viscosity reducers with different interfacial tensions and subsequent water flooding, the injection pressure does not rise and decrease slowly until stable, and there is no decline funnel in the water cut curve. The final pressures of viscosity reducer flooding with different interfacial tensions of S1, S2, and S3 are 0.02 MPa, 0.03 MPa, and 0.04 MPa, respectively. In the process of viscosity reducer flooding, the pressure of S3 is slightly higher than that of S2 and S1, because S3 has the worst viscosity reduction performance and emulsification stability and the weakest ability to improve water-oil mobility ratio, so the flow resistance is also the largest in the flow process.

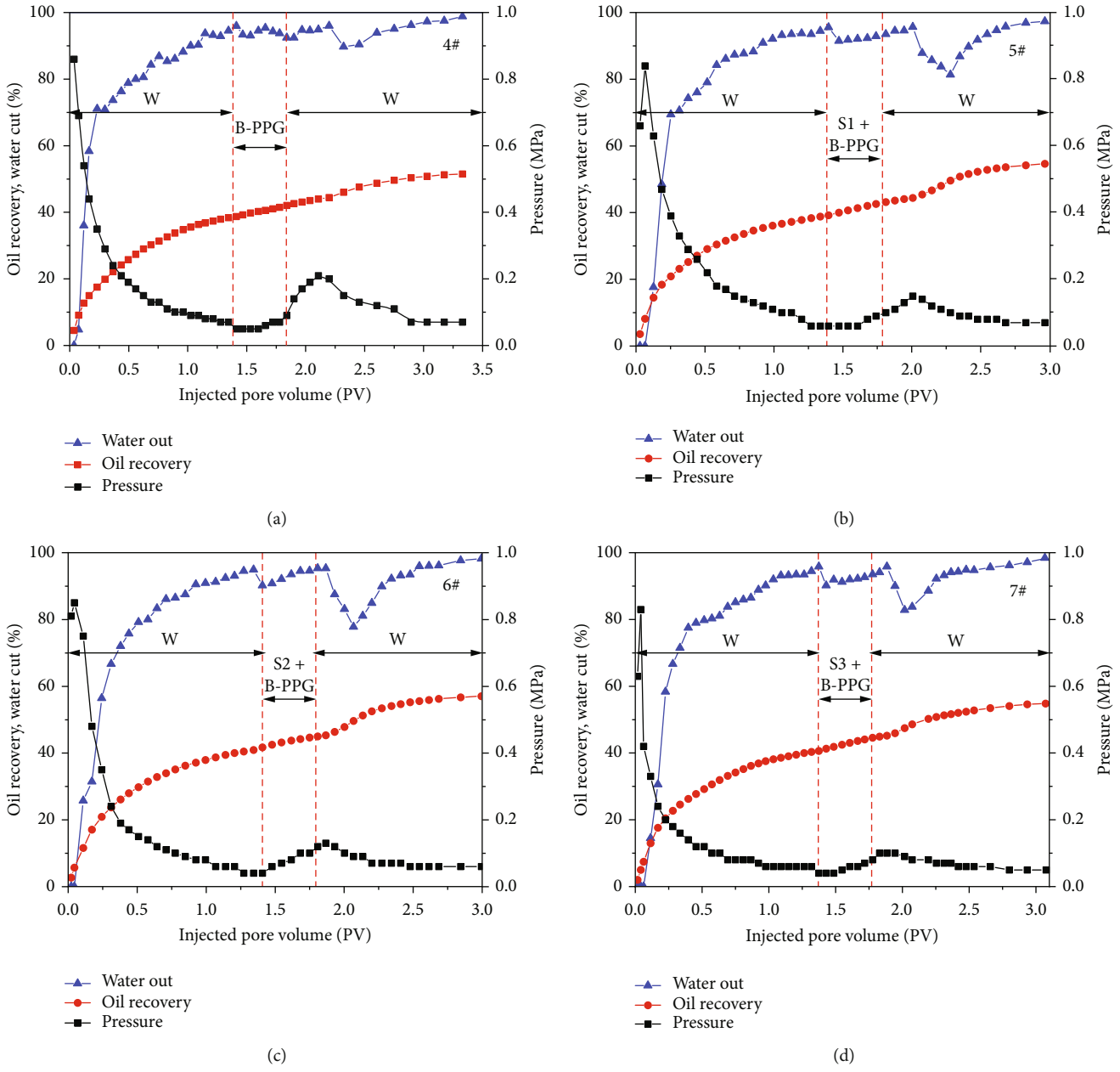

Figure 8: The oil recovery, water cut, and injection pressure versus pore volume: (a) B-PPG flooding; (b) S1/B-PPG flooding; (c) S2/B-PPG flooding; (d) S3/B-PPG flooding.

In order to further compare the EOR efficiency of three viscosity reducers with different interfacial tension, the incremental oil recovery of viscosity reducer flooding is analyzed, as shown in Table 4. The histogram of incremental oil recovery is drawn as shown in Figure 7. The incremental oil recovery of viscosity reducer S2 flooding is the largest, 7.5%, followed by S1, 7.3%, and S3, 5.6%. The results show that viscosity reducer S2 has the best ability to improve the recovery of common heavy oil. Viscosity reducer S2 not only has low interfacial tension and can effectively reduce adhesion work and improve oil displacement efficiency but also has good emulsification and viscosity reduction ability, can improve oil-water flow rate, and can enhance oil recovery.

3.2.2. Analysis of Experimental Results of B-PPG Flooding and Viscosity Reducer/B-PPG Composite Flooding. In the process of viscosity reducer flooding, water channeling is easy to occur, and most of the injected fluid flows out along the dominant channel, so the ability to improve the water-oil mobility ratio is limited. Therefore, the ability to improve the recovery of ordinary heavy oil for viscosity reducer flooding with different interfacial tensions is limited. In order to further compare the ability of three different interfacial tension viscosity reducers to enhance the recovery of ordinary heavy oil, a series of B-PPG flooding and viscosity reducer/B-PPG composite flooding experiments was carried out.

Table 5: The incremental oil recovery results of flooding at different flooding stages.

No.	Chemical slug	Water flooding recovery (%)	Chemical flooding recovery (%)	Incremental oil recovery (%)
4#	B-PPG	38.8	51.5	12.7
5#	S1+B-PPG	39.2	54.9	15.7
6#	S2+B-PPG	40.9	57.1	16.2
7#	S3+B-PPG	40.7	54.8	14.1

Figure 8(a) is the B-PPG flooding curve. Figures 8(b)–8(d) are the flooding curves of viscosity reducer with different interfacial tensions and B-PPG composite system. The flooding process is also divided into three parts. In the early stage of water injection development, the flooding curves are not significantly different. However, in the chemical flooding and subsequent water flooding stages, after injecting B-PPG or composite system, the injection pressure firstly increases and then decreases and finally tends to be stable. The water cut curve shows a downward funnel phenomenon, and the decline range of water cut curve of viscosity reducer/B-PPG composite flooding is more obvious. The reasons for this difference are as follows: In the process of viscosity reducer flooding, the viscosity reducer can enter along the dominant seepage channel formed by water flooding, and the injection pressure does not rise. Moreover, the viscosity reducer can peel off the remaining oil contacted after water flooding and reduce the seepage resistance, resulting in the slow reduction to stability of the injection pressure. In the process of B-PPG flooding or composite flooding, B-PPG will block the dominant seepage channel formed by water flooding. With the continuous injection of B-PPG and composite system, the injection pressure increases slowly. When the pressure rises to a certain extent, B-PPG will break or deform, and the subsequent pressure will decrease.

Moreover, during the subsequent water flooding stage, the peak pressure of the composite system is between 0.10 and 0.15 MPa, which is less than 0.21 MPa of the B-PPG flooding system. The reasons for this difference are that the emulsification and viscosity reduction performance of the viscosity reducer can reduce the flow resistance of heavy oil and reduce the pressure.

Table 5 and Figure 9 depict the incremental oil recovery of B-PPG flooding or viscosity reducer/B-PPG composite flooding at different stages. As shown in the figure, during the chemical flooding stage, the incremental oil recovery of B-PPG is 12.7%, while that of composite flooding is between 14.1 and 16.2%.

Compared with viscosity reducer flooding, B-PPG flooding has better EOR efficiency. In the process of viscosity reducer flooding, water channeling is easy to occur, most of the injected fluid flows out along the dominant channel, and the ability to improve the water-oil mobility ratio is limited. B-PPG can increase the viscosity of injection fluid and improve the water-oil mobility ratio. It can block the dominant seepage channel generated in the process of water flooding and expand the swept volume. The results show that the effect of improving water-oil mobility ratio and increasing sweep volume is greater than that of emulsification, viscosity reduction, and oil displacement efficiency.

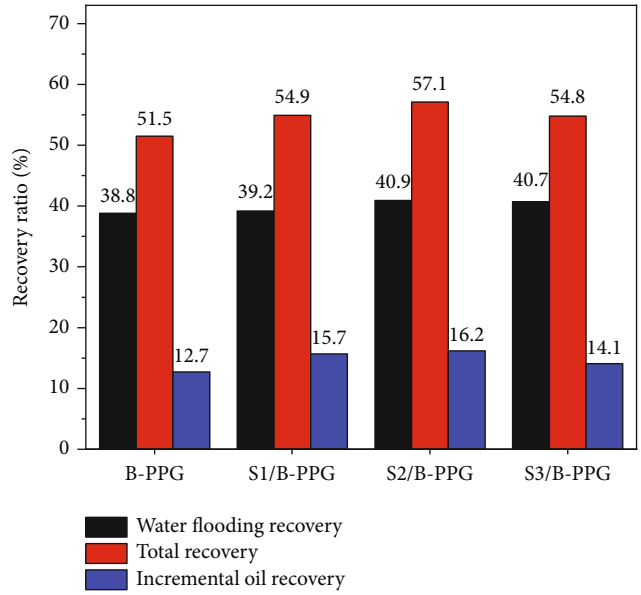

Figure 9: The incremental oil recovery results of flooding at different flooding stages.

Whether it is viscosity reducer flooding or viscosity reducer/B-PPG composite flooding, the ability of emulsion oriented S1 to improve the recovery of ordinary heavy oil is significantly better than that of low interfacial tension viscosity reducer S3, indicating that the mechanism of emulsion viscosity reduction and displacement is more critical than low interfacial tension for recovering ordinary heavy oil reservoir. The incremental oil recovery of S2 is higher than that of emulsified viscosity reducer S1, which shows that the viscosity reducer with low interfacial tension has better EOR effect when the emulsifying capacity and viscosity reducing performance are similar.

4. Conclusions

In this study, a series of experiments including physicochemical property evaluation of viscosity reducer and B-PPG and sand pack flooding experiments was systematically conducted to investigate the EOR ability of three different viscosity reducers, B-PPG, and viscosity reducer/B-PPG composite systems. Some main conclusions can be drawn as follows:

(1) The oil-water interfacial tensions of the three viscosity reducers S1, S2, and S3 are 0.432 $mN \cdot m^{-1}$, 0.0112 $mN \cdot m^{-1}$, and 0.0031 $mN \cdot m^{-1}$, respectively. S1 with the highest interfacial tension has the best

emulsification and viscosity reduction performance, S2 is the second, and S3 is the worst. The lower the interfacial tension, the worse the emulsification stability and the worse the viscosity reduction performance

(2) S2 with moderate interfacial tension and emulsifying capacity has the best EOR efficiency, followed by S1 with the highest interfacial tension and the best emulsifying performance and the recovery increment of S3 with the lowest interfacial tension, and the worst emulsification performance is the smallest. The emulsion viscosity reduction is more important than lowering interfacial tension for viscosity reducer to improve oil recovery of ordinary heavy oil

(3) The incremental oil recovery of B-PPG is 12.7%, which is significantly higher than that of viscosity reducer flooding. Compared with viscosity reducer flooding, the viscosity reducer/B-PPG composite systems have better EOR capacity. For enhancing oil recovery of ordinary heavy oil reservoir, the effect of improving water-oil mobility ratio and increasing sweep volume is greater than that of emulsification, viscosity reduction, and oil displacement efficiency

Data Availability

All data used to support the findings of this study are available from the corresponding author on request.

Conflicts of Interest

The author declares that there are no conflicts of interest.

Acknowledgments

The research was financially supported by the Research Institute of Exploration and Development of Shengli Oilfield, SINOPEC.

References

[1] A. Mai, J. Bryan, N. Goodarzi, and A. Kantzas, "Insights into non-thermal recovery of heavy oil," *Journal of Canadian Petroleum Technology*, vol. 48, no. 3, pp. 27–35, 2009.

[2] V. Alvarado and E. Manrique, "Enhanced oil recovery: an update review," *Energies*, vol. 3, no. 9, pp. 1529–1575, 2010.

[3] B. Su and Y. Fujimitsu, "Research on heavy oil thermal recovery by CO_2 steam flooding with help of combination of borehole-surface electric potential and cross-borehole electric potential," *Energy Exploration and Exploitation*, vol. 29, no. 6, pp. 797–815, 2011.

[4] T. Babadagli and B. Ozum, "BioDiesel as additive in high pressure and temperature steam recovery of heavy oil and bitumen," *Oil & Gas Science and Technology – Revue d'IFP Energies nouvelles*, vol. 67, no. 3, pp. 413–421, 2012.

[5] S. Huang, M. Cao, and L. Cheng, "Experimental study on the mechanism of enhanced oil recovery by multi-thermal fluid in offshore heavy oil," *International Journal of Heat and Mass Transfer*, vol. 122, pp. 1074–1084, 2018.

[6] O. A. Alomair and A. F. Alajmi, "A novel experimental nanofluid-assisted steam flooding (NASF) approach for enhanced heavy oil recovery," *Fuel*, vol. 313, article 122691, 2022.

[7] S. Li, Z. Li, and X. Sun, "Effect of flue gas and n-hexane on heavy oil properties in steam flooding process," *Fuel*, vol. 187, pp. 84–93, 2017.

[8] G. Z. Liao, H. Z. Wang, Z. M. Wang et al., "Oil oxidation in the whole temperature regions during oil reservoir air injection and development methods," *Petroleum Exploration and Development*, vol. 47, no. 2, pp. 357–364, 2020.

[9] W. F. Pu, H. Gao, Y. B. Li, and Q. Luo, "Performance and mechanisms of enhanced oil recovery via CO_2 assisted steam flooding technique in high heterogeneity heavy oil reservoir: PVT and 3D experimental studies," *Petroleum Science and Technology*, vol. 38, no. 15, pp. 823–835, 2020.

[10] G. Feng, Y. Li, and Z. Yang, "Performance evaluation of nitrogen-assisted steam flooding process in heavy oil reservoir via numerical simulation," *Journal of Petroleum Science and Engineering*, vol. 189, article 106954, 2020.

[11] Z. Pang, Y. Jiang, B. Wang, G. Cheng, and X. Yu, "Experiments and analysis on development methods for horizontal well cyclic steam stimulation in heavy oil reservoir with edge water," *Journal of Petroleum Science and Engineering*, vol. 188, article 106948, 2020.

[12] E. Luo, Z. Fan, Y. Hu et al., "An efficient optimization framework of cyclic steam stimulation with experimental design in extra heavy oil reservoirs," *Energy*, vol. 192, article 116601, 2020.

[13] L. Shi, X. Li, C. Xi, Z. Qi, and P. Liu, "Analytical modeling of the oil steam ratio during the lifetime steam-assisted gravity drainage process in extra-heavy oil reservoirs," *Journal of Petroleum Science and Engineering*, vol. 203, article 108616, 2021.

[14] D. W. Zhao, J. Wang, and I. D. Gates, "Optimized solvent-aided steam-flooding strategy for recovery of thin heavy oil reservoirs," *Fuel*, vol. 112, pp. 50–59, 2013.

[15] Y. Zhao, "Laboratory experiment and field application of high pressure and high quality steam flooding," *Journal of Petroleum Science and Engineering*, vol. 189, article 107016, 2020.

[16] P. Li, F. Zhang, T. Zhu, C. Zhang, G. Liu, and X. Li, "Synthesis and properties of the active polymer for enhanced heavy oil recovery," *Colloids and Surfaces A: Physicochemical and Engineering Aspects*, vol. 626, article 127036, 2021.

[17] A. O. Ezzat, A. M. Atta, H. A. al-Lohedan, and A. I. Hashem, "Synthesis and application of new surface active poly (ionic liquids) based on 1,3-dialkylimidazolium as demulsifiers for heavy petroleum crude oil emulsions," *Journal of Molecular Liquids*, vol. 251, pp. 201–211, 2018.

[18] A. M. Hassan, M. Ayoub, M. Eissa, H. Bruining, and P. Zitha, "Study of surface complexation modeling on a novel hybrid enhanced oil recovery (EOR) method; smart-water assisted foam-flooding," *Journal of Petroleum Science and Engineering*, vol. 195, article 107563, 2020.

[19] L. Shi, C. Liu, M. Chen, Z. Hua, and J. Zhang, "Synthesis and evaluation of a hyperbranched copolymer as viscosity reducer for offshore heavy oil," *Journal of Petroleum Science and Engineering*, vol. 196, article 108011, 2021.

[20] Y. Gong and Y. Gu, "Miscible CO_2 simultaneous water-and-gas (CO_2-SWAG) injection in the Bakken formation," in *SPE*

CSUR Unconventional Resources Conference, Calgary, Alberta, Canada, 2015.

[21] Y. Gong and Y. Gu, "Experimental study of water and CO_2 flooding in the tight main pay zone and vuggy residual oil zone of a carbonate reservoir," *Energy & Fuels*, vol. 29, no. 10, pp. 6213–6223, 2015.

[22] L. Xue, P. Liu, and Y. Zhang, "Development and Research Status of Heavy Oil Enhanced Oil Recovery," *Geofluids*, vol. 2022, Article ID 5015045, 13 pages, 2022.

[23] X. Wang, W. Liu, L. Shi et al., "Application of a novel amphiphilic polymer for enhanced offshore heavy oil recovery: mechanistic study and core displacement test," *Journal of Petroleum Science and Engineering*, vol. 215, article 110626, 2022.

[24] X. Gu, Y. Li, J. Yan, J. Zhang, and G. Chen, "Synthesis and investigation of a spiro diborate as a clean viscosity-reducer and pour point depressor for crude oil," *Petroleum Chemistry*, vol. 59, no. 6, pp. 570–574, 2019.

[25] F. Zhang, Y. Liu, Q. Wang, Y. Han, and Y. Tan, "Fabricating a heavy oil viscosity reducer with weak interaction effect: synthesis and viscosity reduction mechanism," *Colloids and Interface Science Communications*, vol. 42, article 100426, 2021.

[26] H. Sun, Z. Wang, Y. Sun, G. Wu, B. Sun, and Y. Sha, "Laboratory evaluation of an efficient low interfacial tension foaming agent for enhanced oil recovery in high temperature flue-gas foam flooding," *Journal of Petroleum Science and Engineering*, vol. 195, article 107580, 2020.

[27] X. Jiang, M. Liu, X. Li, L. Wang, S. Liang, and X. Guo, "Effects of surfactant and hydrophobic nanoparticles on the crude oil-water interfacial tension," *Energies*, vol. 14, no. 19, p. 6234, 2021.

[28] A. K. Manshad, M. Rezaei, S. Moradi, I. Nowrouzi, and A. H. Mohammadi, "Wettability alteration and interfacial tension (IFT) reduction in enhanced oil recovery (EOR) process by ionic liquid flooding," *Journal of Molecular Liquids*, vol. 248, pp. 153–162, 2017.

[29] X. Wang, H. Zhang, X. Liang, L. Shi, and Z. Ye, "New amphiphilic macromolecule as viscosity reducer with both asphaltene dispersion and emulsifying capacity for offshore heavy oil," *Energy & Fuels*, vol. 35, no. 2, pp. 1143–1151, 2021.

[30] S. J. D. Sofla, M. Sharifi, and A. H. Sarapardeh, "Toward mechanistic understanding of natural surfactant flooding in enhanced oil recovery processes: the role of salinity, surfactant concentration and rock type," *Journal of Molecular Liquids*, vol. 222, pp. 632–639, 2016.

[31] O. S. Alade, D. Al Shehri, M. Mahmoud et al., "A novel technique for heavy oil recovery using poly vinyl alcohol (PVA) and PVA-NaOH with ethanol additive," *Fuel*, vol. 285, article 119128, 2021.

[32] H. Azarhava, A. Jafari, F. Vakilchap, and S. M. Mousavi, "Stability and performance of poly γ-(glutamic acid) in the presence of sulfate ion for enhanced heavy oil recovery," *Journal of Petroleum Science and Engineering*, vol. 196, article 107688, 2021.

[33] Y. Chen, H. He, Q. Yu, H. Liu, and W. Liu, "Insights into enhanced oil recovery by polymer-viscosity reducing surfactant combination flooding in conventional heavy oil reservoir," *Geofluids*, vol. 2021, Article ID 7110414, 12 pages, 2021.

[34] L. F. Lamas, V. E. Botechia, D. J. Schiozer, M. L. Rocha, and M. Delshad, "Application of polymer flooding in the revitalization of a mature heavy oil field," *Journal of Petroleum Science and Engineering*, vol. 204, article 108695, 2021.

[35] W. Song and D. G. Hatzignatiou, "On the reduction of the residual oil saturation through the injection of polymer and nanoparticle solutions," *Journal of Petroleum Science and Engineering*, vol. 208, article 109430, 2021.

[36] K. Medica, R. Maharaj, D. Alexander, and M. Soroush, "Evaluation of an alkali-polymer flooding technique for enhanced oil recovery in Trinidad and Tobago," *Journal of Petroleum Exploration and Production Technology*, vol. 10, no. 8, pp. 3947–3959, 2020.

[37] P. Ghosh and K. K. Mohanty, "Study of surfactant-polymer flooding in high-temperature and high-salinity carbonate rocks," *Energy & Fuels*, vol. 33, no. 5, pp. 4130–4145, 2019.

[38] F. Rezaeiakmal and R. Parsaei, "Visualization study of polymer enhanced foam (PEF) flooding for recovery of waterflood residual oil: effect of cross flow," *Journal of Petroleum Science and Engineering*, vol. 203, article 108583, 2021.

[39] M. Kokubun, F. A. Radu, E. Keilegavlen, K. Kumar, and K. Spildo, "Transport of polymer particles in oil-water flow in porous media: enhancing oil recovery," *Transport in Porous Media*, vol. 126, no. 2, pp. 501–519, 2019.

[40] R. Farajzadeh, A. Ameri, M. J. Faber, D. W. van Batenburg, D. M. Boersma, and J. Bruining, "Effect of continuous, trapped, and flowing gas on performance of alkaline surfactant polymer (ASP) flooding," *Industrial & Engineering Chemistry Research*, vol. 52, no. 38, pp. 13839–13848, 2013.

[41] M. A. Kalbani, M. Jordan, E. Mackay, K. Sorbie, and N. Long, "Modelling the impact of alkaline-surfactant and alkaline-surfactant-polymer flooding processes on scale precipitation and management," *Journal of Petroleum Science and Engineering*, vol. 205, article 108777, 2021.

[42] A. Davarpanah and B. Mirshekari, "Numerical simulation and laboratory evaluation of alkali–surfactant–polymer and foam flooding," *International journal of Environmental Science and Technology*, vol. 17, no. 2, pp. 1123–1136, 2020.

[43] A. Aitkulov and K. K. Mohanty, "Investigation of alkaline-surfactant-polymer flooding in a quarter five-spot sandpack for viscous oil recovery," *Journal of Petroleum Science and Engineering*, vol. 175, pp. 706–718, 2019.

[44] Z. Li, Y. Wang, H. He, F. Yuan, and Y. Chen, "Insights into the effects of salinity on the transport behavior of polymer-enhanced branched-preformed particle gel suspension in porous media," *Energy & Fuels*, vol. 35, no. 2, pp. 1104–1112, 2021.

[45] H. He, W. Liu, Y. Chen, H. Liu, H. Liu, and G. Luo, "Synergistic mechanism of well pattern adjustment and heterogeneous phase combined flooding on enhancing oil recovery in mature fault-block reservoirs," *Journal of Petroleum Exploration and Production Technology*, vol. 12, no. 12, pp. 3387–3398, 2022.

[46] W. Liu, H. He, F. Yuan et al., "Influence of the injection scheme on the enhanced oil recovery ability of heterogeneous phase combination flooding in mature waterflooded reservoirs," *ACS Omega*, vol. 7, no. 27, pp. 23511–23520, 2022.

[47] W. Zhu, B. Li, Y. Liu, H. Song, M. Yue, and N. Wu, "A new calculating method for relative permeability of branched preformed particle gel flooding in multiphase composite system," *Special Topics & Reviews in Porous Media*, vol. 10, no. 1, pp. 89–98, 2019.

[48] Q. J. Du, G. M. Pan, J. Hou, L. L. Guo, R. R. Wang, and Z. Z. Xia, "Study of the mechanisms of streamline-adjustment-

assisted heterogeneous combination flooding for enhanced oil recovery for post-polymer-flooded reservoirs," *Petroleum Science*, vol. 16, no. 3, pp. 606–618, 2019.

[49] H. He, J. Fu, B. Hou et al., "Investigation of injection strategy of branched-preformed particle gel/polymer/surfactant for enhanced oil recovery after polymer flooding in heterogeneous reservoirs," *Energies*, vol. 11, no. 8, p. 1950, 2018.

[50] M. O. Elsharafi and B. Bai, "Effect of weak preformed particle gel on unswept oil zones/areas during conformance control treatments," *Industrial & Engineering Chemistry Research*, vol. 51, pp. 11547–11554, 2013.

[51] B. Bai, L. Li, Y. Liu, H. Liu, Z. Wang, and C. You, "Preformed particle gel for conformance control: factors affecting its properties and applications," *SPE Reservoir Evaluation & Engineering*, vol. 10, no. 4, pp. 415–422, 2007.

[52] L. Xu, Z. Qiu, H. Gong et al., "Synergy of microbial polysaccharides and branched-preformed particle gel on thickening and enhanced oil recovery," *Chemical Engineering Science*, vol. 208, article 115138, 2019.

Hindawi
Geofluids
Volume 2023, Article ID 3701163, 9 pages
https://doi.org/10.1155/2023/3701163

WILEY | Hindawi

Research Article

Pore Structure and Permeability Variations during Gas Displacement in Unconsolidated Sandstone Reservoirs through CT Reconstruction Analysis

Yuqiang Zha, Bao Cao, Fengying Li, Qing Ye, Shaopeng Zhu, Wei Zhou, and Runfu Xiong

CNOOC China Limited, Hainan Branch, Haikou 570311, China

Correspondence should be addressed to Yuqiang Zha; zhayq@cnooc.com.cn

Received 14 February 2023; Revised 15 March 2023; Accepted 21 April 2023; Published 29 May 2023

Academic Editor: Shiling Zhang

The continuous gas displacement in unconsolidated sandstone gas reservoirs will necessarily result in the pore structure and rock permeability variations, which cannot be neglected in the gas development process. However, the variations have not been comprehensively addressed yet, especially for the rock structure in pore scale. This work presented the quantitative results of pore structure in microscale and permeability variations during gas displacement in unconsolidated sandstone reservoirs through computed tomography (CT) reconstruction analysis. The results indicated that a more than 3% increase in porosity after gas displacement resulted from the enlargement of the pore and throat with a diameter of more than 20 μm and 3 μm, respectively, owing to the release and migration of clay and fine particles, in spite of the distribution frequency decline of both pore and throat with a small diameter. The pore connectivity would be enhanced by the increase of the connected pores as well as the enlargement of the pore and throat sizes. However, the pore-throat coordination number could only change with slight improvement. In terms of permeability and relative permeability changes with pore structure, the improvement of permeability after gas displacement was higher than that of porosity, and the continuous gas displacement would broaden gas-water flow region and lower irreducible water saturation and residual gas saturation, and then, the equal phase relative permeability point would shift to the right. These investigations will contribute to more accurate reserve evaluation and productivity prediction.

1. Introduction

Natural gas as a clean energy resource has been wildly applied in various fields, including heating, power generation, automobile fuel, food processing, steel industry, chemical refining, hydrogen production, and synthetic ammonia [1–3]. More attention has been paid to the exploration and development of natural gas. How to get a better development effect becomes crucial to extracting more resources. Among all types of natural gas reservoirs in China, the development of unconsolidated sandstone gas reservoirs such as the gas fields in the Qaidam Basin, western South China Sea, and Baoshan Basin [4–6] has been confronted with kinds of problems including sand production, water channeling, and more serious heterogeneity [7–9], further affecting the productivity. These problems result from the changes in the petrophysical properties of the unconsolidated sandstone, especially the changes in the pore structure and permeability [10, 11].

The changes are primarily on account of the release and migration of rock mineral particles including clay and fine particles in the long-term flow of gas and water [12, 13]. The continuous fluid flow in porous media, especially in the unconsolidated sandstone, will enlarge and also block the pore throat, further changing the permeability [14, 15]. The pore structure and permeability variations should be comprehensively addressed so as to get a better understanding of them. However, the research to date mostly concentrates on the macroscopic time-dependent porosity and permeability evolution in core and field scale including physical and numerical simulation [16–18], especially for oil reservoirs [19–22]. And the macroscopic investigation

Table 1: Mineralogical compositions of the core.

Quartz (%)	Potassium feldspar (%)	Plagioclase (%)	Calcite (%)	Montmorillonite (%)	Illite (%)	Kaolinite (%)	Chlorite (%)
55.5	8.1	14.4	1.3	4.60	6.00	5.84	4.26

Table 2: Petrophysical properties of the core samples.

Sample no.	Gas permeability (mD)	Porosity (%)	Length (cm)	Diameter (cm)	Pore volume (cm^3)
$1^{\#}$	/	35.71	1.10	0.60	0.11
$2^{\#}$	39.24	34.22	6.01	2.49	10.01

will not provide a revealing insight into the microscope evolution. The general ways to investigate the pore structure include centrifuge, mercury intrusion, nitrogen adsorption, nuclear magnetic resonance (NMR), and computed tomography (CT) [23–27]. All of them can reflect the pore size distribution but cannot physically present the spatial pore structure except CT [28]. With the rapid development of experimental detection technology, the CT technology with higher scanning precision and better reconstruction algorithm makes it easy to provide a deep insight into the changes in pore scale [29, 30]. It has been increasingly utilized in the fluid distribution and pore structure reconstruction [31, 32]. By the CT reconstruction analysis, the parameters can be characterized in pore scale, including the number and geometry of pore and throat, 3D pore structure, and pore connectivity [33, 34]. The changes in pore scale can further clarify the changes in macroscopic porosity and permeability. However, rare research has been conducted to investigate pore structure and permeability variations during gas displacement through CT reconstruction analysis.

Therefore, this work conducted the quantitative evaluations of pore structure in microscale and permeability variations during gas displacement in unconsolidated sandstone reservoirs by means of CT reconstruction analysis. Firstly, the number and size distribution of the pore and throat were evaluated to probe into the pore structure variations after gas displacement. Then, the pore connectivity was investigated from the aspects of the changes of connected pores and pore-throat coordination number. Eventually, the changes in the macroscopic porosity and permeability including relative permeability were further evaluated and clarified by the variations of the structure and connectivity in the pore scale. The comprehensive investigations will provide a deeper insight into the rock petrophysical property changes in the gas displacement process in unconsolidated sandstone gas reservoirs and contribute to more accurate reserve evaluation and productivity prediction.

2. Experimental Section

2.1. Materials. The rock cores used in the experiments were obtained with a water saturation of 0.46 from the unconsolidated sandstone gas reservoir at a depth of 1414.73 m. The XRD analysis was carried out on an X-ray diffractometer (TD-3500, Tongda Science & Technology Co., Ltd., China) to determine the compositions of the core as shown in Table 1. Due to the loose structure of the rock sample, the core samples were drilled out by liquid nitrogen freezing technology rather than the common treatment. Two types of the core samples were drilled out to investigate the pore structure by CT reconstruction and clarify the gas-water permeability. The permeability and porosity of each sample were tested using an automated permeameter-porosimeter (AP-608, Coretest Systems, USA). The petrophysical properties of the core samples are listed in Table 2.

2.2. Instruments. The instruments used in the displacement experiments mainly included an ISCO pump, intermediate container, flow meter, pressure sensor, nitrogen bottle, confining pressure system, high-resolution micronano CT scanner (nanoVoxel-4000, Tianjin Sanying Precision Instrument Co., Ltd., China), and core holder as shown in Figure 1. The XRD analysis was carried out on an X-ray diffractometer (TD-3500, Tongda Science & Technology Co., Ltd., China) to determine the compositions of the core. The porosity and permeability of the core sample were tested using an automated permeameter-porosimeter (AP-608, Coretest Systems, USA).

2.3. Methods and Procedures

2.3.1. Gas Displacement Experiments. The displacement experiments were carried out using the instruments as shown in Figure 1. The experimental procedures can be described as follows: (1) the core sample was cleaned and dried. (2) The core sample was saturated by the 3.0 wt.% KI solution, further aged for 24 h at 85°C. And then, it was scanned by micronano CT to reconstruct the pore structure. (3) The gas displacement was conducted with the gas injected into the sample along the longitudinal axis at an inlet pressure of 0.2 MPa at a flow rate of 5~7 mL/min with a confining pressure of 0.8 MPa. (4) The sample was scanned by micronano CT to reconstruct the pore structure after injecting a certain pore volume (PV) (500 PV and 1000 PV). (5) According to the CT scanning results, the reconstruction analysis was carried out to obtain the pore and throat parameters before and after gas displacement.

Additionally, the gas-water relative permeability measurements were conducted by a nonsteady state method using the same instruments except the CT scanner as the literature [35].

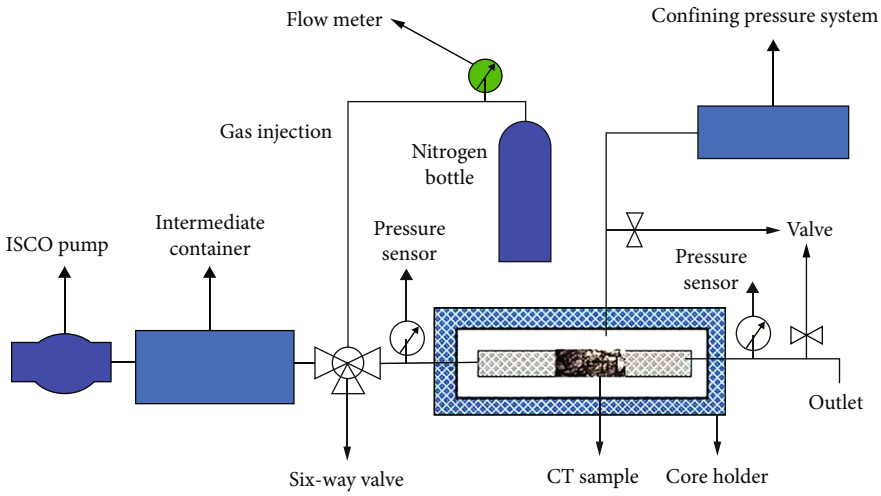

Figure 1: Instruments and procedures of displacement experiments.

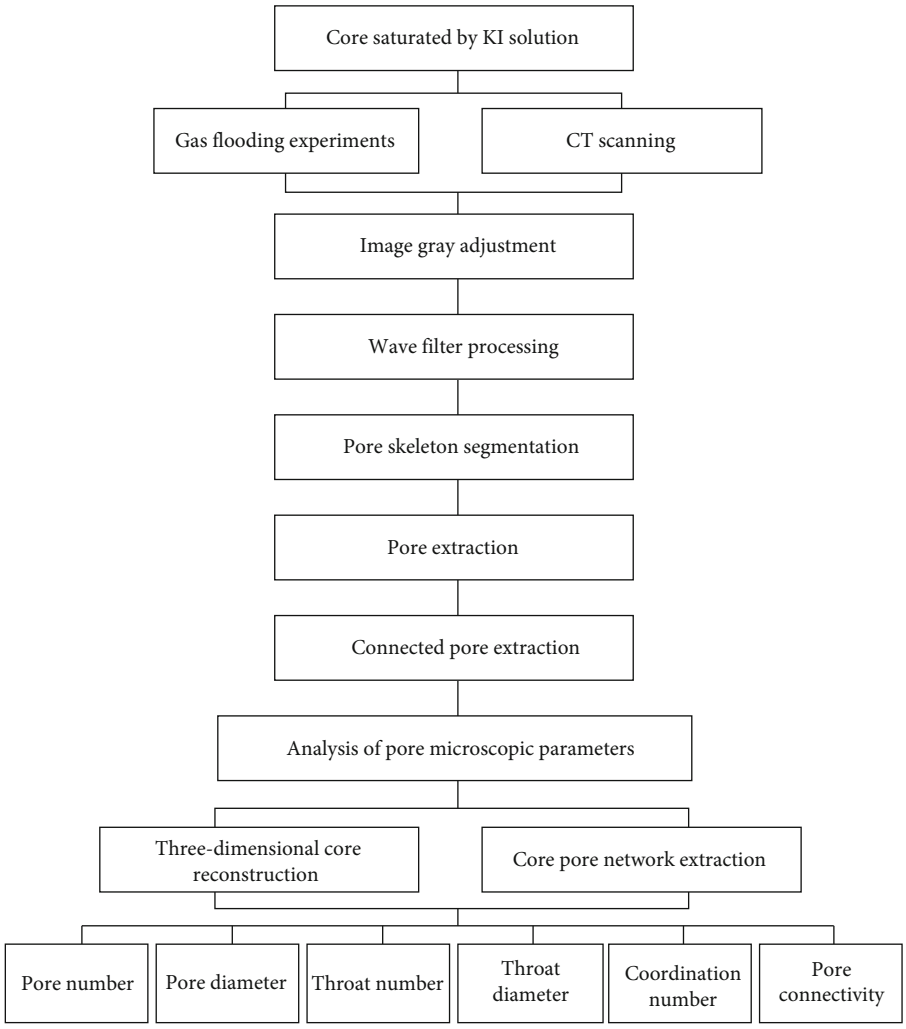

Figure 2: Procedures of CT reconstruction analysis.

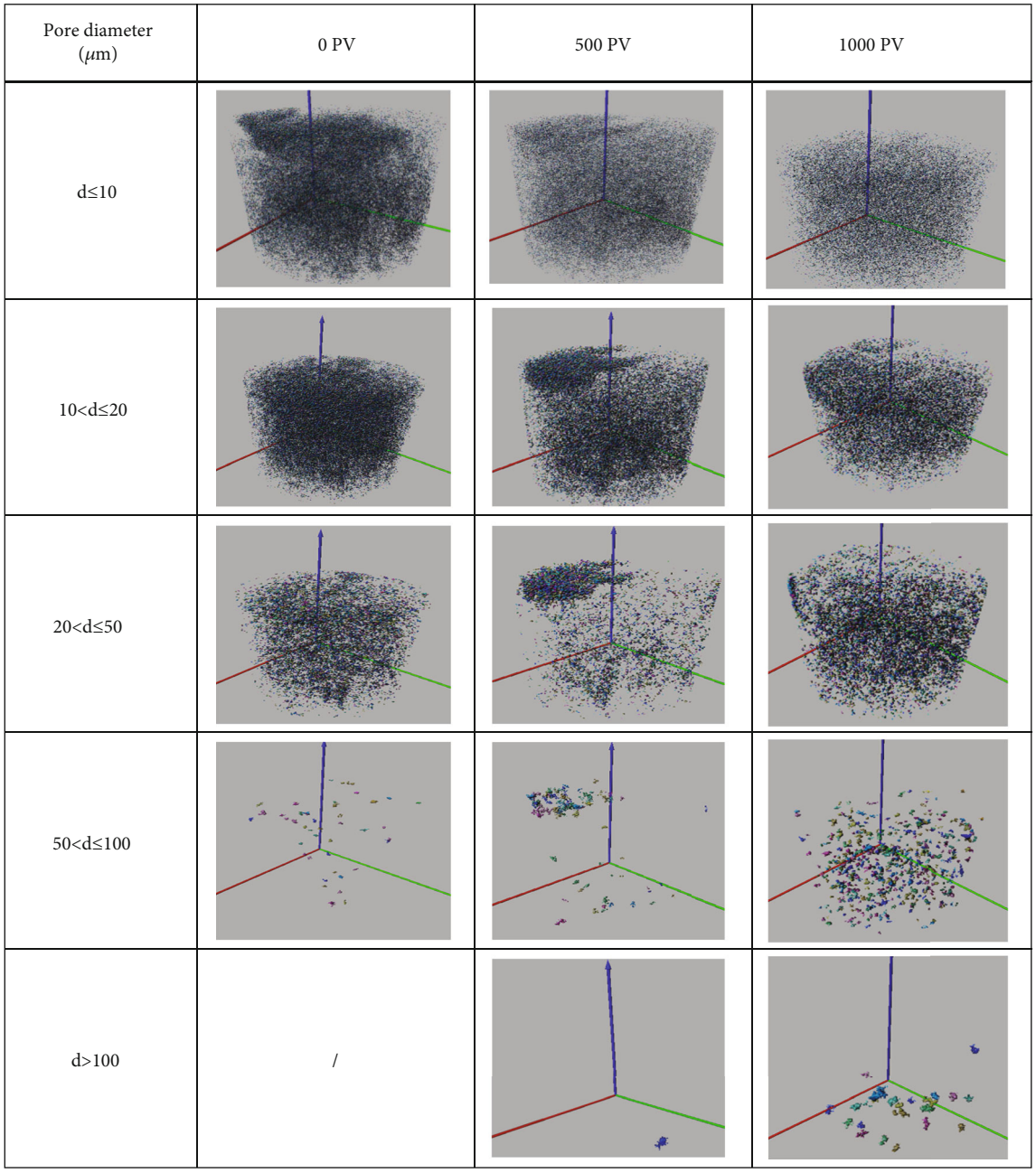

Figure 3: Structure variations of pores of different sizes before and after gas displacement.

2.3.2. CT Reconstruction Analysis. The pore structure was analyzed by CT reconstruction. The reconstruction analysis procedures for the core sample before and after gas displacement are just as shown in Figure 2, mainly including several procedures as follows:

(1) *CT Scanning*. The core sample was scanned by the nanoVoxel-4000 to obtain the high-resolution images

(2) *Data Reconstruction*. The scanning data was processed by algorithm reconstruction and image rectification using the reconstruction software Voxel Studio Recon, including image gray adjustment and wave filter processing

(3) *Data Analysis*. The reconstructed data was then analyzed by the image analysis software such as Volume Graphics Studio Max, FEI Avizo, SYPI-core, and Voxel Studio Render. The analyzed parameters mainly included the number and size of pore and throat, coordination number, and pore and throat connectivity

3. Results and Discussions

3.1. Effects of Gas Displacement on Pore Size. The core sample $1^{\#}$ was used to investigate the pore structure variations. The structures of pores of different sizes in the core sample before and after gas displacement were reconstructed

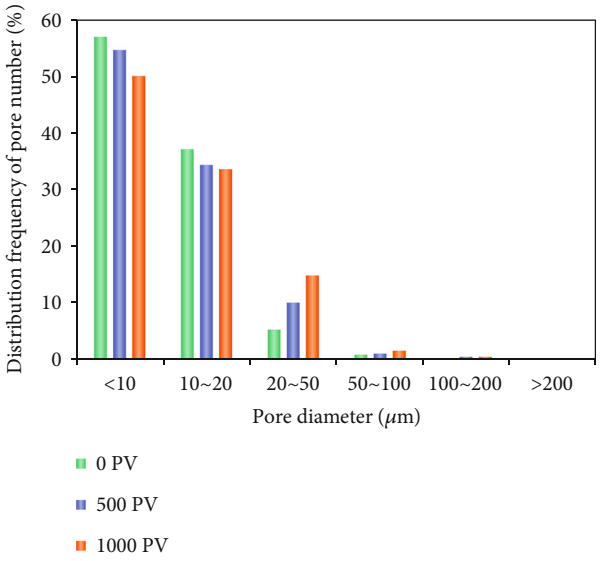

Figure 4: Number distribution frequencies of pores of different sizes before and after gas displacement.

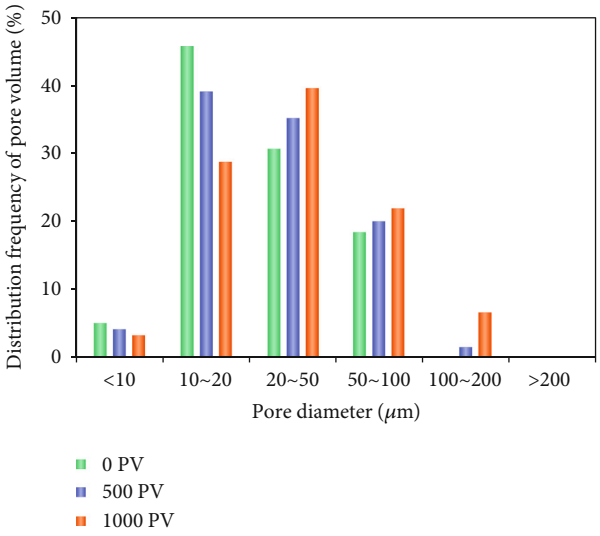

Figure 5: Volume distribution frequencies of pores of different sizes before and after gas displacement.

through CT scanning analysis, which is shown in Figure 3. And then, the distribution frequencies of the number and volume of pores of different sizes before and after gas displacement were calculated according to the 3D pore reconstruction analysis, and the results are shown in Figures 4 and 5. It suggested that the small pores and large pores changed in different ways. In general, the small pores outnumbered the large pores, but the volume of pores of different sizes was in normal distribution. With the gas injection, both the number and volume of the pores with a diameter less than 20 μm accounted for lower levels, while these of the larger pores accounted for higher levels. Among the pores, the number and volume distribution frequencies of the pores with a diameter from 20 μm to 50 μm increased significantly, and the pores with a diameter of more than

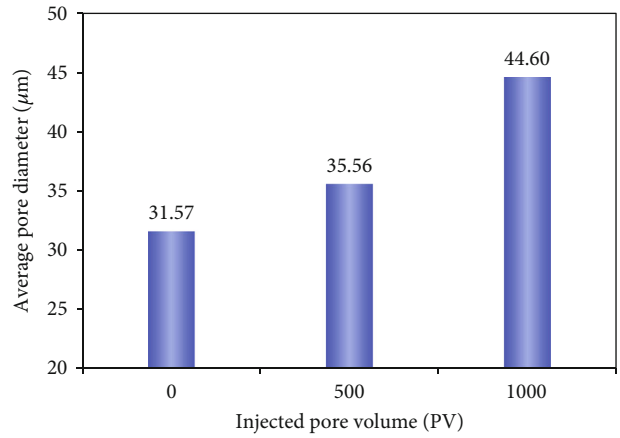

Figure 6: Average pore diameter before and after gas displacement.

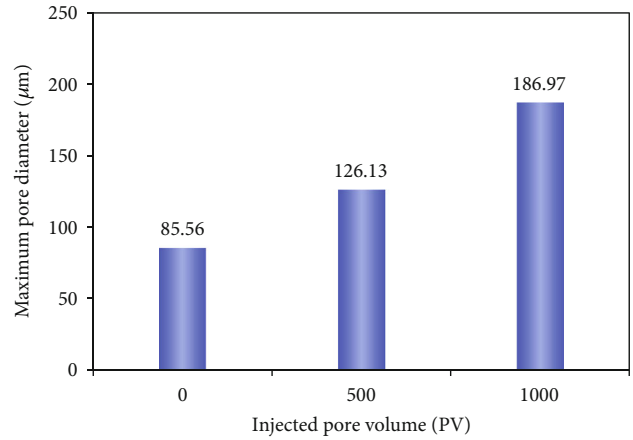

Figure 7: Maximum pore diameter before and after gas displacement.

100 μm came into existence after 500 PV gas was injected. It was calculated that the average and maximum pore diameter before and after gas displacement improved from 31.57 μm to 44.60 μm and 85.56 μm to 186.97 μm, respectively, as shown in Figures 6 and 7, which increased by 118.53% and 41.27%. Therefore, the continuous gas injection would lead to an apparent enlargement of pore size owing to the release and migration of unconsolidated sandstone particles [12, 14].

3.2. Effects of Gas Displacement on Pore-Throat Size. The number distribution frequencies of pore throats of different sizes before and after gas displacement were also calculated as shown in Figure 8 to investigate the pore-throat structure variations. It suggested that the number distribution frequencies of pore throats exhibited the same changes as these of the pores. The small pore throat outnumbered the large pore throat, and the number distribution frequencies of the pore throat with a diameter of less than 3 μm decreased from 56.2% to 49.7%, while these of the pore throat with a diameter of more than 3 μm increased that led to the increase of

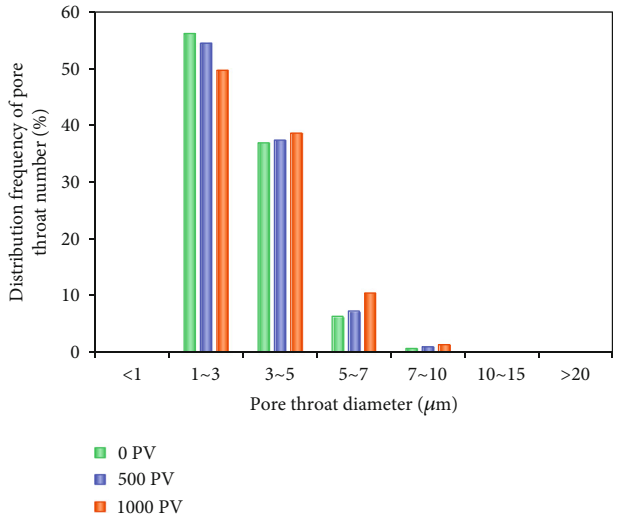

Figure 8: Number distribution frequencies of pore throats of different sizes before and after gas displacement.

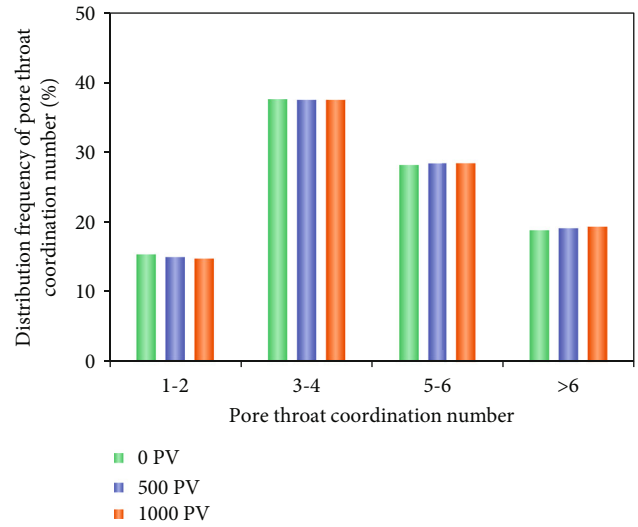

Figure 10: Distribution frequencies of pore-throat coordination number before and after gas displacement.

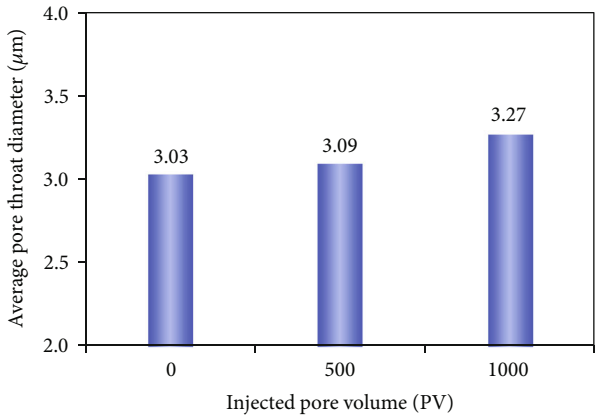

Figure 9: Average pore-throat diameter before and after gas displacement.

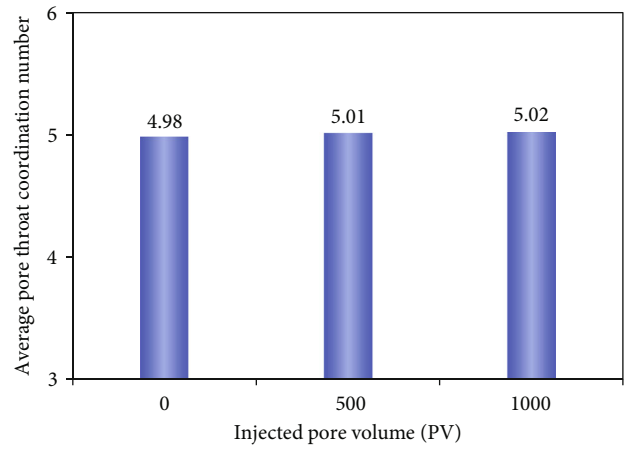

Figure 11: Average pore-throat coordination number before and after gas displacement.

the average pore-throat diameter before and after gas displacement from 3.03 μm to 3.27 μm as shown in Figure 9. The enlargement of the pore-throat diameter due to the rock mineral particle migration would enhance the pore connectivity and then improve the core permeability [36].

3.3. Effects of Gas Displacement on Pore-Throat Coordination Number. In order to investigate the pore-throat connectivity, the distribution frequencies of pore-throat coordination number before and after gas displacement were calculated as shown in Figure 10. And then, the average of the pore-throat coordination number was also calculated as shown in Figure 11. It suggested that the pore-throat coordination number from 3 to 6 accounted for the majority with a proportion of approximately 66%, and the average pore-throat coordination number came to be about 5. In terms of results before and after gas displacement, both the distribution and the average pore-throat coordination number changed slightly with few frequency declines of small pore-throat coordination number and few frequency increases of large pore-throat coordination number. The frequency decline might result from the particle blocking in the pore throat with a small diameter and low coordination number. Thus, it could be seen that the gas injection would enlarge the pore-throat diameter but have little effect on the coordination number between the pores and the throats.

3.4. Effects of Gas Displacement on Pore Connectivity. The pore structures of the CT core sample before and after gas displacement were reconstructed through CT scanning analysis, which is shown in Figure 12. And then, the porosities of both connected and isolated pores were calculated according to the 3D pore reconstruction analysis, and the results are shown in Figure 13. It suggested that the connected pores

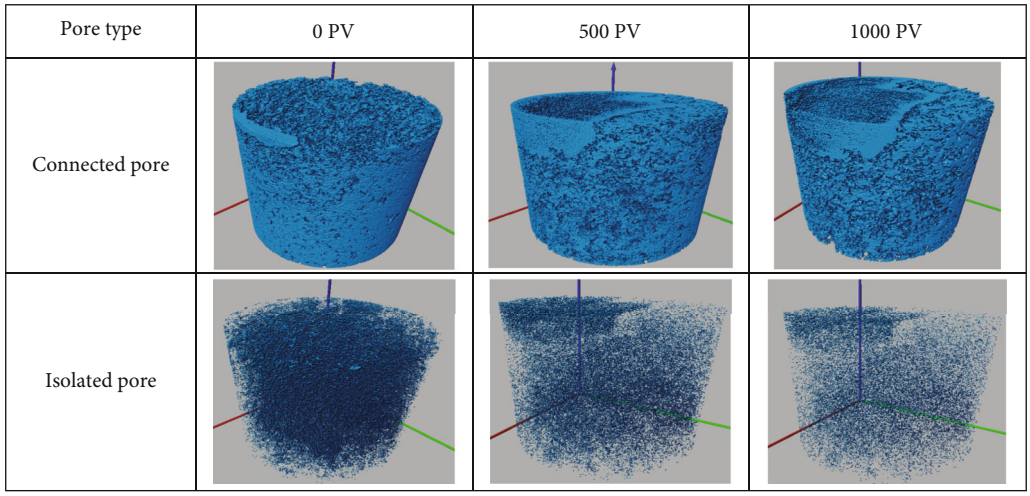

Figure 12: 3D structures of both connected and isolated pores before and after gas displacement.

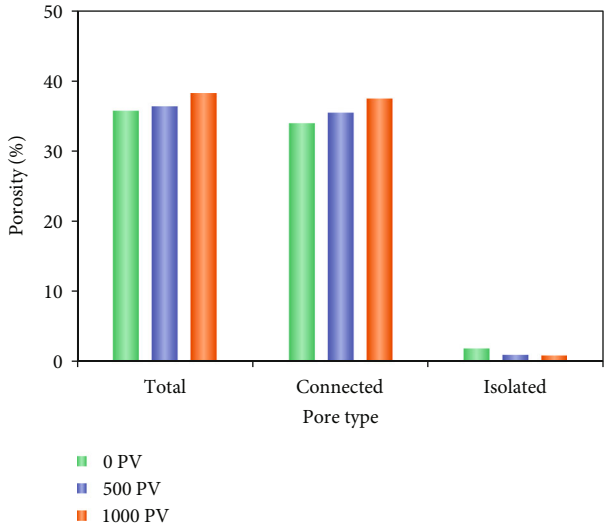

Figure 13: Porosities of both connected and isolated pores before and after gas displacement.

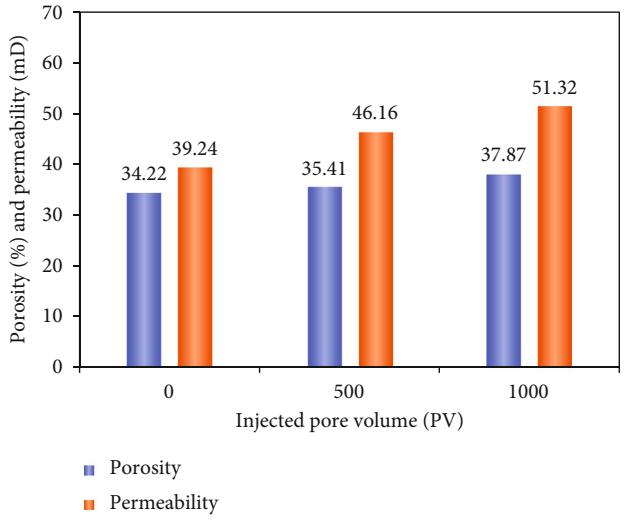

Figure 14: Porosity and permeability before and after gas displacement.

constituted the majority of the total pores with a proportion of more than 95%. After gas displacement, the porosity of the isolated pores declined, while the porosity of the connected pores increased by 10.3% from 33.9% to 37.4%, which brought about an increase of 2.5% from 35.7% to 38.2% in the total porosity. It can be seen from the results that the pore connectivity would be strengthened as a whole in spite of the pore blocking owing to the particle migration in the unconsolidated sandstone, and the reconnected pores outnumbered the reisolated pores in the gas injection process.

3.5. Effects of Gas Displacement on Porosity and Permeability. The core sample 2# was saturated by 3.0 wt.% KI solution and then flooded by gas (N_2) to 1000 PV. The porosity and permeability of the core sample were measured in different injected pore volumes, and the results are shown in Figure 14. It showed that both the porosity and permeability of the core sample increased apparently from 34.22% to 37.87% and 39.24 mD to 51.32 mD, respectively, which went up by 10.67% and 30.78%. The growth rate of the permeability was greater than that of the porosity [36]. The rock permeability was primarily based on the larger pores. The increase of the permeability of the core in unconsolidated sandstone mainly resulted from the enlargement of the pore and throat with larger sizes as well as the enhancement of the pore connectivity due to the particle migration as found above. Therefore, the porosity and permeability variations would not be neglected in the continuous gas displacement process in unconsolidated sandstone gas reservoirs, which could lead to the evident changes in the gas reserves as well as the well injectivity and productivity.

3.6. Effects of Gas Displacement on Relative Permeability. In gas reservoirs with edge and bottom water, gas and water

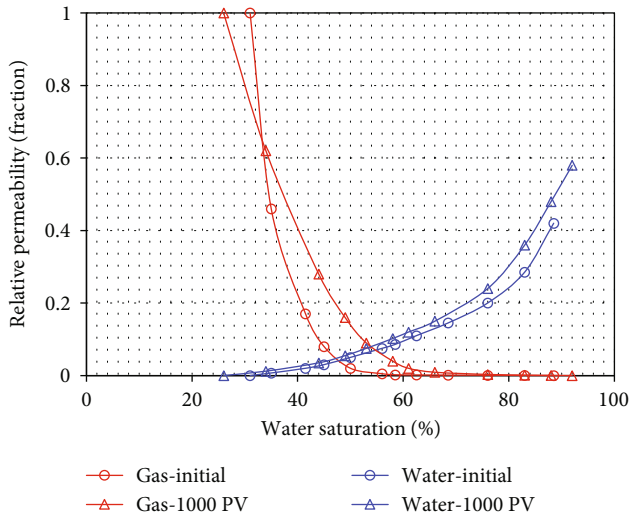

Figure 15: Gas and water relative permeability before and after gas displacement.

flow in the same place. The pore structure variations in the gas displacement process will necessarily result in the changes in phase relative permeability [37]. In order to investigate the gas and water flow principle, the gas-water relative permeability curves were measured before and after gas displacement as shown in Figure 15. From the measurement results, the initial gas and water relative permeability before gas injection were low sunken curves, and then, both the gas and water relative permeability increased after 1000 PV gas injection. The irreducible water saturation and the residual gas saturation dropped from 31.2% to 26.1% and 11.5% to 8.0%, which broadened the two-phase flow region. Additionally, the equal phase relative permeability point shifted to the right from 47.3% to 54.0%. The improvement of the phase relative permeability also got benefit from the enlargement of the pore and throat size as well as the enhancement of the pore connectivity. Compared with the water relative permeability, the gas relative permeability had a higher improvement.

4. Conclusions

In the current investigation, we present the quantitative results of pore structure and permeability variations during gas displacement in unconsolidated sandstone reservoirs through CT reconstruction analysis. Useful conclusions drawn from our research results are listed as follows:

(1) The continuous gas displacement would bring about an increase of more than 2.5% in the total porosity and enhance the pore connectivity, which primarily resulted from the enlargement of the pore and throat with larger sizes owing to the release and migration of clay and fine particles in unconsolidated sandstone reservoirs. The porosity of the connected pores constituted the majority of the total pores with a proportion of more than 95% and increased by 10.3% after gas displacement

(2) The continuous gas displacement not only improved the porosity and permeability from 34.22% to 37.87% and 39.24 mD to 51.32 mD, respectively, but also broadened the two-phase flow region. The irreducible water saturation and the residual gas saturation dropped, and the equal phase relative permeability point shifted to the right. Both the gas and water relative permeability could be enhanced after gas displacement in unconsolidated sandstone reservoirs

Abbreviations

CT: Computed tomography
NMR: Nuclear magnetic resonance
PV: Pore volume.

Data Availability

The data that support the findings of this study are available from the corresponding author, Zha Y., upon reasonable request.

Conflicts of Interest

The authors declare that they have no conflicts of interest.

Acknowledgments

This work was supported by the Hainan Branch and the Zhanjiang Branch of CNOOC China Limited, China.

References

[1] I. O. Stanley, "Gas-to-liquid technology: prospect for natural gas utilization in Nigeria," *Journal of Natural Gas Science & Engineering*, vol. 1, no. 6, pp. 190–194, 2009.

[2] J. A. Velasco, L. Lopez, M. Velásquez, M. Boutonnet, S. Cabrera, and S. Järås, "Gas to liquids: a technology for natural gas industrialization in Bolivia," *Journal of Natural Gas Science & Engineering*, vol. 2, no. 5, pp. 222–228, 2010.

[3] S. H. Mohr and G. M. Evans, "Long term forecasting of natural gas production," *Energy Policy*, vol. 39, no. 9, pp. 5550–5560, 2011.

[4] Y. C. Xu, W. H. Liu, P. Shen et al., "Carbon and hydrogen isotopic characteristics of natural gases from the Luliang and Baoshan basins in Yunnan Province, China," *Science in China Series D: Earth Sciences*, vol. 49, no. 9, pp. 938–946, 2006.

[5] C. H. Ou, X. Wang, C. C. Li, and Y. He, "Three-dimensional modelling of a multi-layer sandstone reservoir: the Sebei gas field, China," *Acta Geologica Sinica (English Edition)*, vol. 90, no. 1, pp. 209–221, 2016.

[6] C. Yan, J. Deng, Y. Cheng, X. Yan, J. Yuan, and F. Deng, "Rock mechanics and wellbore stability in Dongfang 1-1 gas field in South China Sea," *Geomechanics and Engineering*, vol. 12, no. 3, pp. 465–481, 2017.

[7] J. Deng, L. Wang, P. Li, and W. Zhao, "The critical pressure difference prediction of sand production in deepwater sandstone gas reservoirs," *Petroleum Science and Technology*, vol. 31, no. 19, pp. 1925–1932, 2013.

[8] J. Ren, L. Zhang, J. Ezekiel, S. Ren, and S. Meng, "Reservoir characteristics and productivity analysis of tight sand gas in

upper Paleozoic Ordos Basin China," *Journal of Natural Gas Science & Engineering*, vol. 19, pp. 244–250, 2014.

[9] R. Zhang, X. Shi, R. Zhu et al., "Critical drawdown pressure of sanding onset for offshore depleted and water cut gas reservoirs: modeling and application," *Journal of Natural Gas Science & Engineering*, vol. 34, pp. 159–169, 2016.

[10] Y. Wang, Y. Yang, K. Wang et al., "Changes in relative permeability curves for natural gas hydrate decomposition due to particle migration," *Journal of Natural Gas Science and Engineering*, vol. 84, article 103634, 2020.

[11] L. Jia, S. J. Peng, J. Xu, F. Yan, J. Chen, and B. Wu, "Investigation on gas drainage effect under different borehole layout via 3D monitoring of gas pressure," *Journal of Natural Gas Science and Engineering*, vol. 101, article 104522, 2022.

[12] T. Nguyen, A. Zeinijahromi, and P. Bedrikovetsky, "Fines-migration-assisted improved gas recovery during gas field depletion," *Journal of Petroleum Science and Engineering*, vol. 109, pp. 26–37, 2013.

[13] C. Wei, M. Zou, Y. Sun, Z. Cai, and Y. Qi, "Experimental and applied analyses of particle migration in fractures of coalbed methane reservoirs," *Journal of Natural Gas Science and Engineering*, vol. 23, pp. 399–406, 2015.

[14] A. Zeinijahromi, A. Vaz, and P. Bedrikovetsky, "Well impairment by fines migration in gas fields," *Journal of Petroleum Science & Engineering*, vol. 88-89, pp. 125–135, 2012.

[15] J. Q. Li, G. Zhao, Z. L. Qi et al., "Stress sensitivity of formation during multi-cycle gas injection and production in an underground gas storage rebuilt from gas reservoirs," *Petroleum Exploration and Development*, vol. 48, no. 4, pp. 968–977, 2021.

[16] T. Zhou, W. Yan, J. Su et al., "The influence of injected fluids on microscopic pore structures in the intersalt dolomitic shale oil reservoirs," *Geofluids*, vol. 2019, Article ID 4923173, 13 pages, 2019.

[17] Y. A. Sazali, W. M. L. Sazali, J. M. Ibrahim, G. Graham, and S. Gödeke, "Investigation of fines migration for a high-pressure, high-temperature carbonate gas reservoir offshore Malaysia," *Journal of Petroleum Exploration and Production Technology*, vol. 10, no. 6, pp. 2387–2399, 2020.

[18] W. Zhang, Q. Zhao, X. Guan, Z. Wang, and Z. Wang, "Experiment and model of conductivity loss of fracture due to fine-grained particle migration and proppant embedment," *Energies*, vol. 15, no. 7, p. 2359, 2022.

[19] Y. Hao, M. Smith, Y. Sholokhova, and S. Carroll, "CO_2-induced dissolution of low permeability carbonates. Part II: numerical modeling of experiments," *Advances in Water Resources*, vol. 62, no. 12, pp. 388–408, 2013.

[20] Z. Li, W. Zhang, Y. Tang, B. Li, Z. Song, and J. Hou, "Formation damage during alkaline-surfactant-polymer flooding in the Sanan-5 block of the Daqing oilfield, China," *Journal of Natural Gas Science & Engineering*, vol. 35, no. Part A, pp. 826–835, 2016.

[21] X. Huang and Y. P. Zhao, "Characterization of pore structure, gas adsorption, and spontaneous imbibition in shale gas reservoirs," *Journal of Petroleum Science & Engineering*, vol. 159, pp. 197–204, 2017.

[22] R. Jiang, W. Zhang, P. Zhao et al., "Characterization of the reservoir property time-variation based on 'surface flux' and simulator development," *Fuel*, vol. 234, pp. 924–933, 2018.

[23] S. Karimi and H. Kazemi, "Characterizing pores and pore-scale flow properties in middle Bakken cores," *SPE Journal*, vol. 23, no. 4, pp. 1343–1358, 2018.

[24] S. Karimi, H. Kazemi, and A. S. Gary, "Capillary pressure and wettability indications of middle Bakken core plugs for improved oil recovery," *SPE Reservoir Evaluation & Engineering*, vol. 22, no. 1, pp. 310–325, 2019.

[25] B. Cao, P. Wei, F. Tian et al., "Experimental investigation on cyclic huff-n-puff with surfactants based on complex fracture networks in water-wet oil reservoirs with extralow permeability," *Geofluids*, vol. 2021, Article ID 6898581, 10 pages, 2021.

[26] B. Cao, X. Lu, K. Xie et al., "The pore-scale mechanisms of surfactant-assisted spontaneous and forced imbibition in water-wet tight oil reservoirs," *Journal of Petroleum Science & Engineering*, vol. 213, article 110371, 2022.

[27] M. C. Ribeiro, J. G. Filgueiras, A. Souza, P. M. Vianna, R. B. V. de Azeredo, and R. Leiderman, "Image-based simulation of molecular diffusion on NMR pulsed-field gradient experiments: feasibility to estimate tortuosity and permeability of porous media," *Journal of Petroleum Science and Engineering*, vol. 219, article 111064, 2022.

[28] C. H. Arns, F. Bauget, A. Limaye et al., "Pore-scale characterization of carbonates using X-ray microtomography," *SPE Journal*, vol. 10, no. 4, pp. 475–484, 2005.

[29] R. Taghizadeh, K. Goshtasbi, A. K. Manshad, and K. Ahangari, "Geomechanical and thermal reservoir simulation during steam flooding," *Structural Engineering & Mechanics*, vol. 66, no. 4, pp. 505–513, 2018.

[30] Q. Cao, Y. Gong, T. Fan, and J. Wu, "Pore-scale simulations of gas storage in tight sandstone reservoirs for a sequence of increasing injection pressure based on micro-CT," *Journal of Natural Gas Science and Engineering*, vol. 64, pp. 15–27, 2019.

[31] J. Chaves and R. Moreno, "Low- and high-resolution X-ray tomography helping on petrophysics and flow-behavior modeling," *SPE Journal*, vol. 26, no. 1, pp. 206–219, 2021.

[32] A. Hanafy, H. A. Nasr-El-Din, and H. Zoya, "A novel method to assess stimulation of sandstone cores damaged by fines migration," *SPE Journal*, vol. 27, no. 1, pp. 682–704, 2022.

[33] H. Sun, J. Yao, Y.-c. Cao, D.-y. Fan, and L. Zhang, "Characterization of gas transport behaviors in shale gas and tight gas reservoirs by digital rock analysis," *International Journal of Heat and Mass Transfer*, vol. 104, pp. 227–239, 2017.

[34] S. Saraf and A. Bera, "A review on pore-scale modeling and CT scan technique to characterize the trapped carbon dioxide in impermeable reservoir rocks during sequestration," *Renewable and Sustainable Energy Reviews*, vol. 144, article 110986, 2021.

[35] C. Li, X. Li, S. Gao et al., "Experiment on gas-water two-phase seepage and inflow performance curves of gas wells in carbonate reservoirs: a case study of Longwangmiao Formation and Dengying Formation in Gaoshiti-Moxi block, Sichuan Basin, SW China," *Petroleum Exploration and Development*, vol. 44, no. 6, pp. 983–992, 2017.

[36] M. S. Sabo and L. E. Beckingham, "Porosity-permeability evolution during simultaneous mineral dissolution and precipitation," *Water Resources Research*, vol. 57, no. 6, pp. 1–15, 2021.

[37] C. Van der Land, R. Wood, K. J. Wu et al., "Modelling the permeability evolution of carbonate rocks," *Marine and Petroleum Geology*, vol. 48, no. 48, pp. 1–7, 2013.

Hindawi
Geofluids
Volume 2023, Article ID 9271981, 7 pages
https://doi.org/10.1155/2023/9271981

Research Article

Numerical Simulation of Superheated Steam Flow and Heat Transfer in a Balanced Steam Injection Flow Control Device

Qiuying Du,[1] **Mingzhong Li**,[1] **Chenwei Liu**,[1] **and Sanbao Dong**[2]

[1]*School of Petroleum Engineering, China University of Petroleum, Qingdao 266580, China*
[2]*College of Chemistry and Chemical Engineering, Xi'an Shiyou University, Xian 710065, China*

Correspondence should be addressed to Mingzhong Li; limingzhong_upc@hotmail.com

Received 17 November 2022; Revised 2 January 2023; Accepted 13 April 2023; Published 12 May 2023

Academic Editor: Daoyi Zhu

Dual-string steam injection pipe is widely used in the production of superheated steam injection in heavy oil horizontal wells. Due to the nonuniform steam injection volume at the heel end and the existence of an interlayer and other factors in the reservoir, the distribution of steam cavity is not uniform, so it is necessary to control the flow of the steam injection well. Based on the basic principles of fluid mechanics and heat transfer, a three-phase nozzle outflow control device model is established in this paper. The steam flow and heat transfer law in the flow control device is numerically simulated, and the outflow dynamic law of horizontal well OCD completion in heavy oil reservoir is obtained. On this basis, the influence of OCD aperture parameters, steam injection pressure, and steam injection velocity on OCD throttling effect is studied. The results show that OCD has a good control effect on balancing pressure drop and improving steam injection uniformity. When the throttle aperture occupies 1/3 of the pipe diameter, the throttle effect is the best and the heat loss is low. Increasing the steam injection pressure can rapidly enhance the pressure reduction rate of the throttle hole. The throttling effect of increasing steam injection volume is not obvious, and the energy loss becomes higher. The study of this paper provides a reference for parameter optimization and prediction of steam distribution in the flow control device of horizontal wells.

1. Introduction

In recent years, after the large-scale implementation of steam injection technology in horizontal wells of heavy oil reservoirs, due to the influence of reservoir heterogeneity and variable mass flow in the horizontal wellbore [1], uneven production of horizontal reservoirs generally exists in the process of general steam injection [2, 3]. A large number of horizontal well monitoring data show that 80% of horizontal wells are unevenly utilized, and only 1/3 to 1/2 of the total well sections are well utilized [4].

To solve the above problems, double-pipe steam injection string is widely used in horizontal wells, namely, one long steam injection string at the heel end and one short steam injection string at the toe end of the steam injection well, to effectively improve the uneven steam injection phenomenon caused by the loss along the well and the heterogeneity of the reservoir.

However, the dual-steam injection string creates a dumbbell-shaped steam chamber, so the flow control devices [5–7] can be installed as part of a sand screen assembly in either a steam injection well or a production well, or in both wells at the same time, resulting in more uniform steam chamber expansion. The outflow control device, or OCD for short [8, 9], is mainly deployed in steam injection wells, and the direction of fluid flow is from the horizontal wellbore to the reservoir.

By adding an outflow control device (as shown in Figure 1) between the heel and toe of the injection well, the injection points can be evenly distributed, alleviating the bell-shaped steam cavity caused by the traditional dual injection tube design [10–12]. In addition, the OCD completion promotes the consistency of the steam injection profile with the height of the oil layer, promotes the growth of the steam cavity, and improves the oil-steam ratio [13].

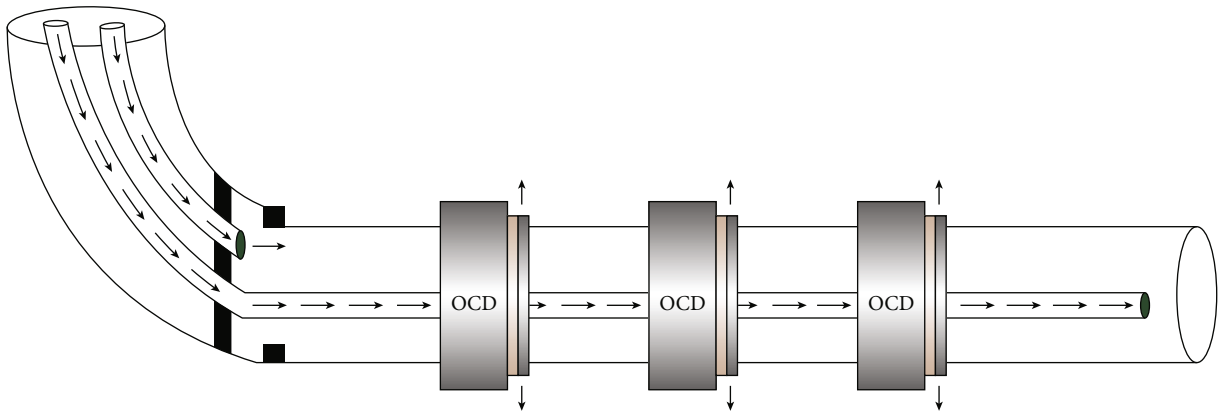

Figure 1: Schematic diagram of outflow control device.

2. Model Description

2.1. OCD Completion Parameter Calculation Model of Horizontal Well. Assume that the steam injection volume of the horizontal well element is as follows:

$$q_{i\mathrm{OCD}} = \frac{\sum q_{\mathrm{is}}}{L}, \tag{1}$$

where $q_{i\mathrm{OCD}}$ is the formation suction velocity, q_{is} is the steam suction velocity in the microsection under conventional completion, and L is the length of horizontal well [14–16].

If $q_{i\mathrm{OCD}}$ of the microsegment is smaller than q_i in conventional completion mode, it indicates that the microsegment has a larger steam output, and OCD device should be installed to take flow-limiting measures.

By putting $q_{i\mathrm{OCD}}$ into Equation (1), the steam injection pressure $P_{i\mathrm{OCD}}$, steam temperature $T_{i\mathrm{OCD}}$, and steam dryness $X_{i\mathrm{OCD}}$ in wellbore under OCD well mode can be obtained [17, 18]. Meanwhile, the annular steam pressure between screen tube and reservoir can be obtained as follows:

$$P_{i\mathrm{ann}} = \frac{-q_{i\mathrm{OCD}} \times I_s}{J_L} + P_r, \tag{2}$$

where $P_{i\mathrm{ann}}$ is the annular steam pressure between screen tube and reservoir, J_L is the microsegment extraction index, I_s is the reservoir inspiration index of microsegment (dimensionless), and P_r is the original formation pressure.

The calculation formula of J_L and I_s is shown as follows:

$$J_L = \frac{2\pi\sqrt{K_h/K_v}K_v\alpha\left(\left(K_{ro}/B_o\mu_o\right) + \left(K_{rw}/B_w\mu_w\right)\right)}{\ln\left(r_{eh}/r_w\right) - 0.75 + S}, \tag{3}$$

$$I_s = \frac{2\ln\left(A_O/r_w^2\right) - 3.86}{\ln\left(A_O/r_w^2\right) - 2.71}, \tag{4}$$

where K_h is the horizontal permeability of reservoir, K_v is the vertical permeability of reservoir, K_{ro} is the relative permeability of crude oil, K_{rw} is the relative permeability of the formation water, μ_o is the formation oil, μ is the formation water viscosity, B_o is the formation crude volume coefficient, B_w is the formation water volume coefficient, α is the unit conversion factor, r_{eh} is the drain radius of the horizontal parallel segment, S is the horizontal wellbore skin factor, A_o is the microsegment drainage area of horizontal well, and r_w is the sieve tube diameter [19–23].

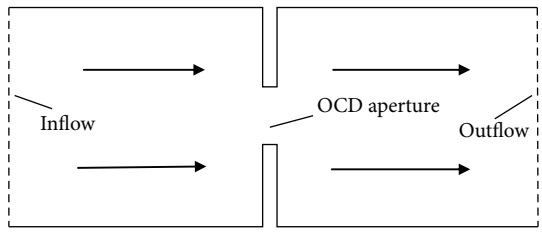

Figure 2: Simplified model of nozzle-type OCD structure.

Table 1: OCD structure basic data.

Name	Value	Unit
Initial reservoir pressure	1.5	MPa
Initial reservoir temperature	297	K
Steam injection pressure	2	MPa
Superheated steam temperature	500	K
Tubing diameter	240	mm
OCD's port size	50	mm
Steam injection volume	100	m^3/d
Steam dryness	100	%

According to the pressure drop balance relationship, the additional drop $P_{i\mathrm{add}}$ of OCD in each segment can be obtained.

$$P_{i\mathrm{OCD}} - P_{i\mathrm{ann}} = P_{i\mathrm{add}}. \tag{5}$$

2.2. Additional Pressure Drops of OCD. The nozzle type-OCD is used to calculate the attached pressure drop of the OCD by using the Bernoulli equation [24, 25].

$$P_{\mathrm{add}} = \frac{8\rho Q^2}{\pi^2 d^4 n^2 C_D^2}, \tag{6}$$

where P_{add} is the additional pressure drops, ρ is the fluid density, Q is the fluid volume flow, d is the diameter of

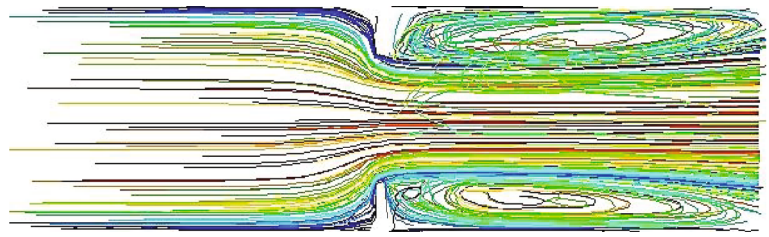

Figure 3: Streamline of steam flow through OCD nozzle.

nozzle orifice, n is the number of nozzle orifices, and C_D is the flow coefficient.

2.3. Calculation Model of Pressure Drop in Horizontal Wellbore. The calculation model of the pressure drop in the tubing of horizontal wells is as follows (ignoring the gravity pressure drop) [26–28]:

$$A_2X_2 = b_2,$$

$$\begin{bmatrix} 1 & & & 0 \\ -1 & 1 & & \\ & \ddots & \ddots & \\ 0 & & -1 & 1 \end{bmatrix} \begin{bmatrix} p_{t,1} \\ p_{t,2} \\ \vdots \\ p_{t,N} \end{bmatrix} = \begin{bmatrix} \frac{32\rho f_1}{\pi^2 d_w^5} q_{w,1}^2 L_1 + \frac{32\rho q_{\text{in},1}}{\pi^2 d_w^4} q_{w,1} + P_{wf} \\ \frac{32\rho f_2}{\pi^2 d_w^5} q_{w,2}^2 L_2 + \frac{32\rho q_{\text{in},2}}{\pi^2 d_w^4} q_{w,2} \\ \vdots \\ \frac{32\rho f_N}{\pi^2 d_w^5} q_{w,N}^2 L_N + \frac{32\rho q_{\text{in},N}}{\pi^2 d_w^4} q_{w,N} \end{bmatrix}, \quad (7)$$

where f_j is the friction factor in section j, $P_{t,j}$ is the tubing pressure in section j, $q_{\text{in},j}$ is the inlet flow rate of section j into the tubing, and $q_{w,j}$ is the flow rate in the microelement pipe of section j.

The boundary conditions of tubing pressure distribution are shown in

$$p_{t,0} = p_{wf}, \quad (8)$$

where $p_{t,0}$ is the wellhead pressure and p_{wf} is the pressure in the tubing at the heel end, namely, the bottomhole flow pressure [29–32].

3. OCD Simulation Analysis

3.1. The Basic Parameters. Based on the structural characteristics of the horizontal well OCD and numerical simulation accuracy requirements of the completed section, a three-dimensional model of the nozzle flow control device is established (see Figure 2) [33]. Related calculation parameters are shown in Table 1.

3.2. Analysis on Dynamic Characteristics of OCD Outflow in Horizontal Wells. Based on the actual mine parameters, the superheated steam flow in the flow control device is numerically simulated by using a multiphase flow model. The flow diagram of the steam flow is shown in Figure 3. As shown in the figure, steam flows smoothly before entering the hole, and annular flow will be generated near the edge of the pipe wall after passing through the hole. The velocity near the wall decreases, and the velocity in the center reaches the maximum, which is higher than that before entering the hole.

The main factors influencing the flow control device are the throttling effect with OCD aperture, steam injection rate, and steam injection pressure. Based on the frictional pressure drop and heat loss calculation, the flow control device of the three-dimensional numerical model is established. The contrast analysis of the influence of various parameters on the flow control effect is changed, to establish uniform steam injection OCD structure parameters and a steam injection parameter optimization method.

3.3. Influence of Changing OCD Aperture on Current-Limiting Effect. Pore size is the key parameter of OCD design, which has an important influence on the pressure drop, heat loss, and steam cavity development and expansion along the steam injection horizontal well. Considering the same steam injection pressure, steam injection volume, and other parameters, the influence of different OCD apertures on the throttling effect was studied, and the throttling effect of steam valve was simulated under five pore sizes of 20 mm, 50 mm, 80 mm, 110 mm, and 140 mm. The variation of temperature field and pressure field in OCD with different pore sizes is shown in Figure 4.

As can be seen from the Figure 4, with the increase of the steam injection pore size, the pressure sweep range is larger and the pressure drop range is more obvious. At this time, the pressure gradient gradually decreases, forming a low-pressure area between the outlet edge of the aperture and the pipe wall, and the pressure near the edge of the aperture gradually increases. As can be seen from the temperature cloud map, the increase of pore size makes the heat loss smaller, the heat diffusion faster, and the heat coverage area more. The temperature and pressure changes on the pipeline axis line are shown in Figures 5 and 6.

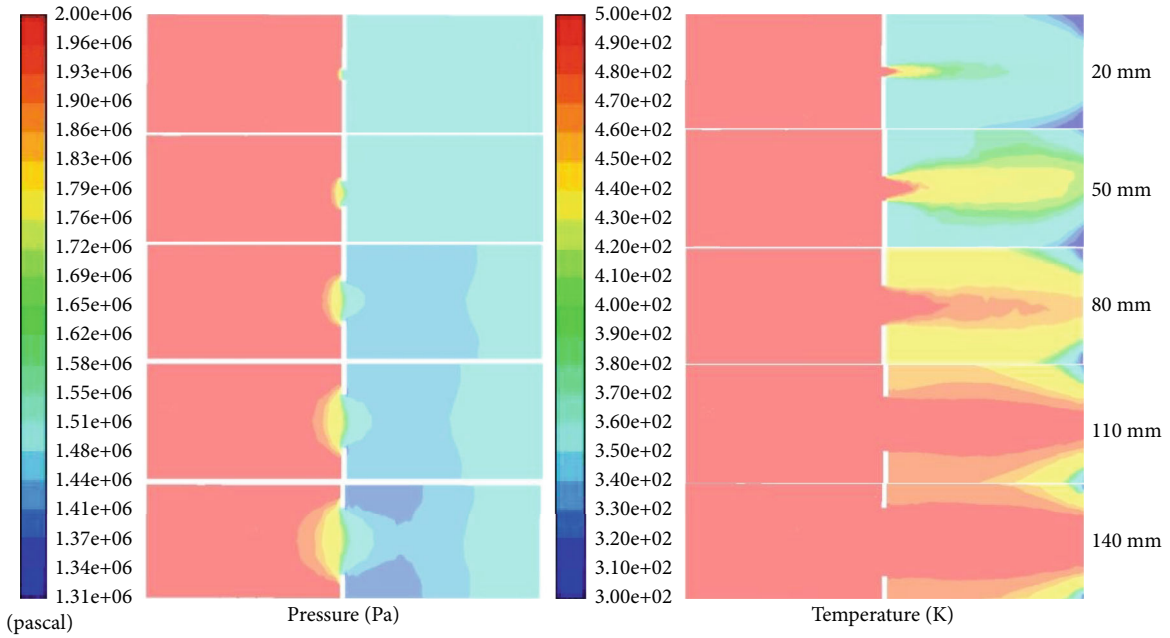

Figure 4: Pressure field and temperature field distribution of steam flow in OCD.

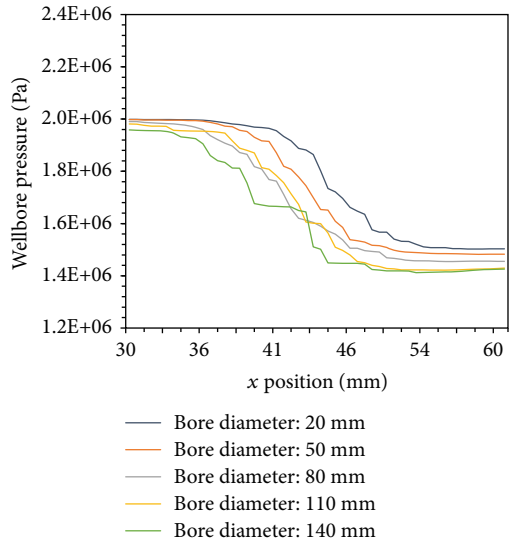

Figure 5: The relationship between pressure and pore size in OCD.

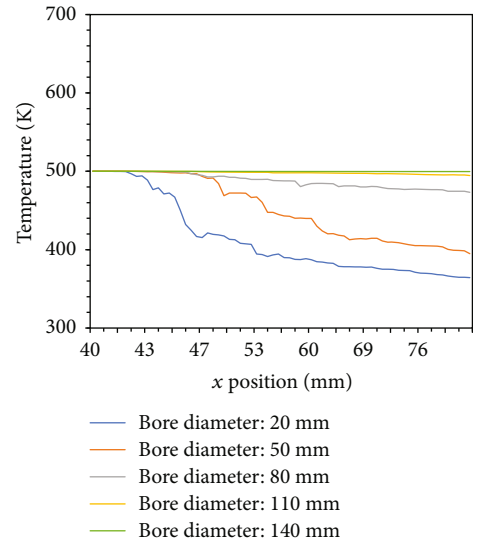

Figure 6: The relationship between temperature and pore size in OCD.

Figure 5 shows the aperture used to increase the flow control device for the pressure drop of the OCD. From the figure, it can be seen that as the pore size increases, the pressure drop increases. Among the pore sizes, for diameters of 110 mm and 140 mm under pressure fluctuations, the change of the throttling effect is smaller, and the simulation result difference is not large. Figure 6 shows that for diameters of 110 mm and 80 mm for the temperature change under different apertures, with the increase of the aperture, the heat loss becomes smaller. When the aperture is between 20 and 50 mm, the heat energy loss is intense and the temperature difference is large. When the aperture is between 80 mm and 140 mm, the temperature drop is not obvious. Therefore, when the aperture is 80 mm, better throttling effect can be achieved.

3.4. Effect of Steam Injection Pressure Change on Outflow Control Device. Taking the steam injection speed of 100 m^3/d, steam dryness of 0.95, steam injection temperature of 500 K, and OCD aperture of 80 mm as design parameters, the steam flow in the flow control device with steam injection pressure of 2 MPa, 2.5 MPa, and 3 MPa, respectively, was simulated. The simulation results are shown in Figures 7 and 8.

As can be seen from Figure 7, increasing the steam injection pressure can increase the throttling strength, and the steam pressure drop through the pore is more obvious. Figure 8 shows the variation of steam flow velocity through the hole with steam injection pressure. It can be seen from

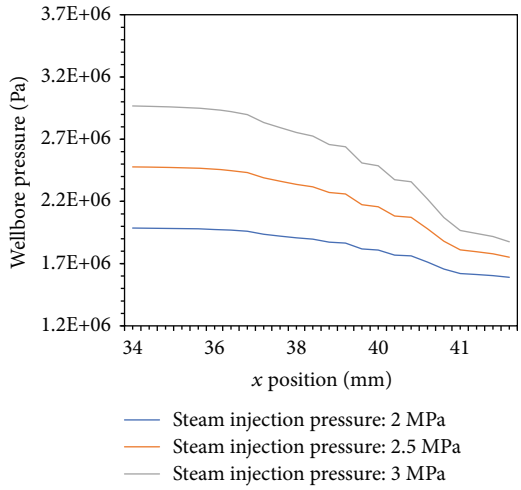

Figure 7: The relationship between OCD internal pressure and steam injection pressure.

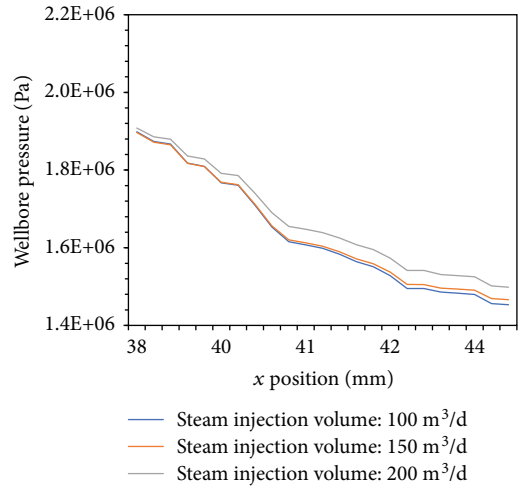

Figure 9: The relationship between pressure variation and steam injection volume in OCD.

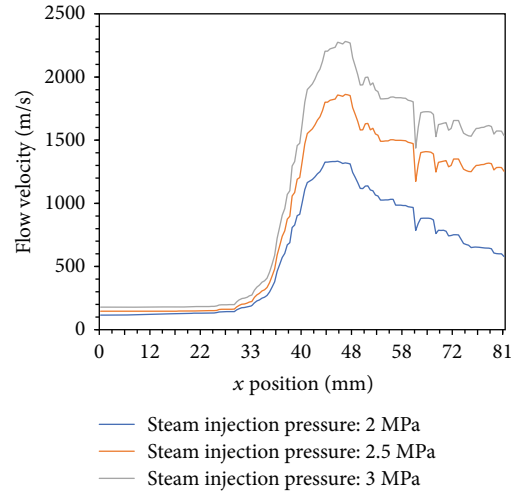

Figure 8: The relationship between OCD velocity and steam injection pressure.

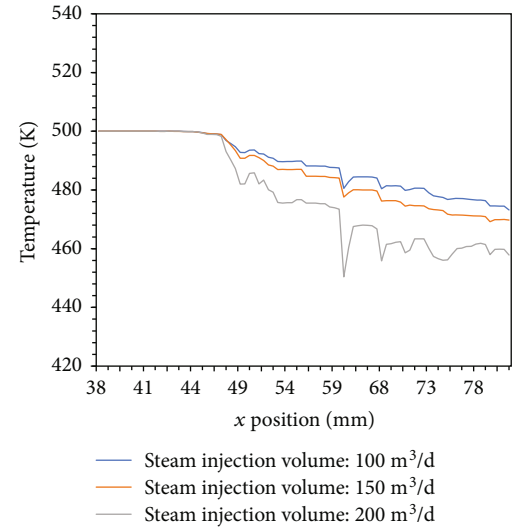

Figure 10: The relationship between temperature variation and steam injection volume in OCD.

the figure that the increase of steam injection pressure will lead to a larger increase of flow velocity near the valve hole and a smaller decrease of velocity after passing the valve.

3.5. Effect of Steam Injection Volume Change on Outflow Control Device. In order to explore the influence of steam injection speed on OCD throttling effect, the steam injection pressure is set as 1.9 MPa, the temperature of superheated steam is 500 K, the pore size is 80 mm, and the internal throttling effect of the outflow control device is simulated when the steam injection volume is 100 m^3/d, 150 m^3/d, and 200 m^3/d, respectively. The simulation results are shown in Figures 9 and 10.

Figure 9 shows the pressure change curve in the flow control device under different steam injection volumes. With the increase of injection volume, the pressure drop decreases faster, and the pressure drop changes of 150 m^3/d and 200 m^3/d are close to each other. Figure 10 shows the temperature variation curve in the flow control device under different steam injection volumes. The temperature fluctuates greatly near the throttle hole. With the increase of steam injection volume, the heat loss is accelerated and the temperature drop is increased.

4. Summary and Conclusions

In this paper, the dynamic outflow law of dual-pipe steam injection OCD completion of the horizontal well in heavy oil reservoir is studied, mainly simulating the outflow control effect of OCD on the target section of the horizontal well with steam injection, as well as the influence of changing steam injection parameters and OCD structural parameters on the throttling control effect. The following conclusions are drawn from the study:

(1) OCD can effectively alleviate the horizontal well completion method in the process of steam injection in the steam cavity of development that is not a balanced phenomenon, through the OCD device installed on the screen, and adjust the OCD nozzle diameter, steam injection pressure, and steam injection rate on the steam injection volume larger through your fingers with the client and the implementation of current limit, reducing the cause of excessive amount of vapor variable mass flow pressure drop loss. The attenuation range of the steam pressure in the wellbore is delayed, so that the steam pressure in the middle of the horizontal well is increased, and the steam injection volume and heating radius are increased, so that the formation along the horizontal section is evenly heated, and the production degree of the reservoir is improved

(2) Changing the nozzle aperture has a significant impact on the current-limiting effect. By comparing the inner diameters of the five groups of nozzles with different sizes, it is found that the larger the aperture, the lower the heat loss. When the aperture is 80 mm, that is, the ratio of the aperture to the pipe diameter is 1 : 3, the better the throttling effect and the lower the heat loss are, which can be used as a priority reference design scheme

(3) Changing the steam injection pressure has a great influence on the flow-limiting effect. With the increase of steam injection pressure, both the pressure drop range and the steam injection speed become larger. Uniform development of the steam cavity can be achieved by appropriately changing the steam injection pressure. The increase of steam injection volume has little effect on the current-limiting effect, and the heat loss range increases with the increase of steam injection speed

The simulation results in this paper can provide a reference for the optimization of the uniform steam injection. Since there is no comparison of various types of FCD throttling effects, relevant research work will be continued in the future.

Data Availability

Data can be obtained from corresponding author.

Conflicts of Interest

The authors declare that there is no conflict of interest regarding the publication of this paper.

Acknowledgments

This work was supported by the National Science and Technology Major Project (no. 2016ZX05031-002) and National Natural Science Foundation of China (no. 51704190).

References

[1] A. Sidahmed, S. Nejadi, and A. Nouri, "A workflow for optimization of flow control devices in SAGD," *Energies*, vol. 12, no. 17, p. 3237, 2019.

[2] D. Zhu, "A dual-directional flow control device for cyclic steam stimulation applications," *SPE Production & Operations*, vol. 37, no. 1, pp. 151–158, 2022.

[3] M. Medina, "Design and field evaluation of tubing-deployed passive outflow-control devices in steam-assisted-gravity-drainage injection wells," *SPE Production & Operations*, vol. 30, no. 4, pp. 283–292, 2015.

[4] P. Liu, Y. Zhou, P. Liu, L. Shi, and L. Li, "Numerical study of herringbone injector-horizontal producer steam assisted gravity drainage (HI-SAGD) for extra-heavy oil recovery," *Journal of Petroleum Science and Engineering*, vol. 181, article 106227, 2019.

[5] S. Banerjee, T. Abdelfattah, and H. Nguyen, "Benefits of passive inflow control devices in a SAGD completion," in *Paper presented at the SPE Heavy Oil Conference-Canada*, Calgary, Alberta, Canada, 2013.

[6] A. Riel, R. C. Burton, G. P. Vachon, T. J. Wheeler, and M. Heidari, "An innovative modeling approach to unveil flow control devices' potential in SAGD application," in *Paper presented at the SPE Heavy Oil Conference-Canada*, Calgary, Alberta, Canada, 2014.

[7] B. Least, S. Greci, R. Huffer, R. V. Rajan, and H. Golbeck, "Steam flow tests for comparing performance of nozzle, tube, and fluidic diode autonomous ICDs in SAGD wells," in *Paper presented at the SPE Heavy Oil Conference-Canada*, Calgary, Alberta, Canada, 2014.

[8] T. Abdelfattah, B. Fisher, and J. Snitkoff, "Design process of inflow control technologies-from inception to application," in *Paper presented at the SPE Thermal Well Integrity and Design Symposium*, Banff, Alberta, Canada, 2016.

[9] M. Javaheri, M. Tran, R. S. Buell, T. L. Gorham, and J. D. Munoz, "Flow profiling using fiber optics in a horizontal steam injector with liner-deployed flow control devices," *SPE Journal*, vol. 26, no. 5, pp. 3136–3150, 2021.

[10] M. Sivagnanam, J. Wang, and I. D. Gates, "On the fluid mechanics of slotted liners in horizontal wells," *Chemical Engineering Science*, vol. 164, pp. 23–33, 2017.

[11] S. Banerjee and B. Hascakir, "Design of flow control devices in steam-assisted gravity drainage (SAGD) completion," *Journal of Petroleum Exploration and Production Technology*, vol. 8, no. 3, pp. 785–797, 2018.

[12] Y. Zhang, P. Li, X. Sun, H. Chen, and Y. Liu, "Steam conformance investigation of flow control devices deployed in SAGD injection and production horizontal wells," *Journal of Petroleum Science and Engineering*, vol. 205, article 108907, 2021.

[13] K. C. Hong and S. Griston, "Best practice for the distribution and metering of two-phase steam," *SPE Production & Facilities*, vol. 12, no. 3, pp. 173–180, 1997.

[14] M. Irani, "On subcool control in SAGD producers—part II: localized-hot-spots effects and optimization of flow-control devices," *SPE Journal*, vol. 24, no. 4, pp. 1613–1629, 2019.

[15] F. A. N. Zifei, H. E. Congge, and X. U. Anzhu, "Calculation model for on-way parameters of horizontal wellbore in the superheated steam injection," *Petroleum Exploration and Development*, vol. 43, no. 5, pp. 798–805, 2016.

[16] H. Gu, L. Cheng, S. Huang, B. Bo, Y. Zhou, and Z. Xu, "Thermophysical properties estimation and performance analysis of superheated-steam injection in horizontal wells considering phase change," *Energy Conversion and Management*, vol. 99, pp. 119–131, 2015.

[17] F. Sun, Y. Yao, M. Chen et al., "Performance analysis of superheated steam injection for heavy oil recovery and modeling of wellbore heat efficiency," *Energy*, vol. 125, pp. 795–804, 2017.

[18] L. A. Nasyrova, I. R. Rakhmatullin, and V. S. Shagapov, "Hydrodynamic and thermal fields in a porous medium with injection of superheated steam," *Fluid Dynamics*, vol. 40, no. 4, pp. 600–612, 2005.

[19] F. Sun, Y. Yao, X. Li, P. Yu, G. Ding, and M. Zou, "The flow and heat transfer characteristics of superheated steam in offshore wells and analysis of superheated steam performance," *Computers & Chemical Engineering*, vol. 100, pp. 80–93, 2017.

[20] R. Yuan, Z. Yang, B. Guo, X. Wang, L. Zhang, and R. Lin, "Potential analysis of enhanced oil recovery by superheated steam during steam-assisted gravity drainage," *Energy Technology*, vol. 9, no. 7, article 2100135, 2021.

[21] Q. Zheng, H. Q. Liu, Z. X. Pang, and F. Li, "A study on effect evaluating and parameters sensitivity analyzing of superheated steam soak in heavy oil reservoirs," *Advanced Materials Research*, vol. 239-242, pp. 3069–3073, 2011.

[22] F. Sun, Y. Yao, and X. Li, "Numerical simulation of superheated steam flow in dual-tubing wells," *Journal of Petroleum Exploration and Production Technology*, vol. 8, no. 3, pp. 925–937, 2018.

[23] P. Li, Y. Zhang, X. Sun, H. Chen, and Y. Liu, "A numerical model for investigating the steam conformance along the dual-string horizontal wells in SAGD operations," *Energies*, vol. 13, no. 15, p. 3981, 2020.

[24] M. Li, H. Chen, Y. Zhang, W. Li, Y. Wang, and M. Yu, "A coupled reservoir/wellbore model to simulate the steam injection performance of horizontal wells," *Energy Technology*, vol. 3, no. 5, pp. 535–542, 2015.

[25] P. Li, Y. Zhang, X. Sun, H. Chen, and Y. Liu, "A coupled model for predicting thermophysical properties of saturated steam in dual-tubing SAGD horizontal wells with toe-point injection technique," *Petroleum Science and Technology*, vol. 40, no. 16, pp. 1925–1944, 2022.

[26] H. Q. Liu, Z. H. Shi, J. Zhu, and Z. Ma, "Optimized design and research on technology parameters of concentric dual-tube steam injection horizontal well," *Applied Mechanics and Materials*, vol. 675-677, pp. 1505–1511, 2014.

[27] T. W. Stone, G. Brown, B. Guyaguler, W. J. Bailey, and D. H. Law, "Practical control of SAGD wells with dual-tubing strings," *Journal of Canadian Petroleum Technology*, vol. 53, no. 1, pp. 32–47, 2014.

[28] F. Sun, Y. Yao, and X. Li, "The heat and mass transfer characteristics of superheated steam in horizontal wells with toe-point injection technique," *Journal of Petroleum Exploration and Production Technology*, vol. 8, no. 4, pp. 1295–1302, 2018.

[29] H. J. Chen, M. Z. Li, Y. Y. Zhang, and W. W. Li, "Steam injection performance of horizontal wells completed with slotted liners," *Applied Mechanics and Materials*, vol. 423-426, pp. 674–678, 2013.

[30] X. Lyu, H. Liu, J. Tian, Q. Zheng, and W. Zhao, "Influence of top water on SAGD steam chamber growth in heavy oil reservoirs: an experimental study," *Journal of Petroleum Science and Engineering*, vol. 208, no. 1, article 109372, 2021.

[31] X. X. Zhu, S. F. Xue, and X. H. Tong, "A new method of improving steam injection profile distribution used in thermal horizontal well and experimental study," *Advanced Materials Research*, vol. 516-517, pp. 228–231, 2012.

[32] Y. Wang, S. Ren, and L. Zhang, "Mechanistic simulation study of air injection assisted cyclic steam stimulation through horizontal wells for ultra heavy oil reservoirs," *Journal of Petroleum Science and Engineering*, vol. 172, pp. 209–216, 2019.

[33] S. Huang, M. Cao, Y. Xia, X. Chen, and M. Yang, "Heat and mass transfer characteristics of steam in a horizontal wellbore with multi-point injection technique considering wellbore stock liquid," *International Journal of Heat and Mass Transfer*, vol. 127, pp. 949–958, 2018.

Hindawi
Geofluids
Volume 2023, Article ID 2197400, 8 pages
https://doi.org/10.1155/2023/2197400

Research Article

Experimental Study on Water-Rock Interaction Characteristics of Unconsolidated Sandstone during CO_2 Multicomponent Thermal Fluid Injection

Mingzhe Guo,[1,2] **Zengmin Lun**,[1] **Bing Zhou**,[1] **Lianguo Wang**,[2] **and Huiqing Liu**[1,2]

[1]*Petroleum Exploration & Production Research Institute, Sinopec, Beijing, China*
[2]*State Key Laboratory of Petroleum Resources and Prospecting, China University of Petroleum (Beijing), Beijing 102249, China*

Correspondence should be addressed to Zengmin Lun; lunzm.syky@sinopec.com

Received 28 September 2022; Revised 7 December 2022; Accepted 31 March 2023; Published 25 April 2023

Academic Editor: Ze Wang

According to the reservoir characteristics and the current situation of CO_2 utilization during thermal recovery in an unconsolidated sandstone heavy oil reservoir, the mechanism and law of porosity and permeability change in an unconsolidated sandstone heavy oil reservoir during CO_2+steam and CO_2+steam+ sodium alpha-olefin sulfonate (AOS) injection were studied by combining a static monomineral water-rock reaction and a dynamic polymineral sand pack displacement experiment. In the static water-rock reaction between CO_2 and monomineral of reservoir rock, the dissolution degree of monomineral at 200°C is greater than that at 100°C and 300°C, and the order of mineral dissolution is illite, montmorillonite, kaolinite, and quartz. Besides, the dissolution rate of single rock minerals decreased significantly in the system of CO_2 with AOS. In the polymineral sand pack displacement experiment, the porosity gradually decreases by CO_2 multicomponent thermal fluid, and the permeability first decreases and then increases by CO_2 multicomponent thermal fluid, but the permeability change is only about 0.5% by CO_2+steam+ AOS, which is mainly attributed to the adsorption of AOS on the rock surface, and it is confirmed in the infrared spectrum of unconsolidated sand after displacement. This also shows that CO_2+steam+AOS can stabilize the rock skeleton structure of the reservoir and prevent the deterioration of heterogeneity in the subsequent development of thermal recovery of heavy oil reservoirs; therefore, the CO_2 multicomponent thermal fluid with chemical agents can improve the damage of a single CO_2 thermal fluid to the reservoir.

1. Introduction

Presently, the increasingly severe climate crisis is another serious test in front of all mankind, requiring all sectors of the world to work together to deal with it, of which fossil energy combustion contributes nearly 67% of the global greenhouse gases [1]. For heavy oil, which is the main supply of fossil energy, the CO_2 multicomponent thermal fluid injection method will be one of the main technologies to reduce carbon dioxide emissions [2, 3]. The carbon dioxide injection is not only to reduce carbon emissions but also to increase crude oil production, which will be the ultimate goal of the CO_2 multicomponent thermal fluid injection method in heavy oil reservoirs [4, 5]. During thermal recovery, the dissolution and transformation of minerals such as quartz and clay near the wellbore occur under a pressure of 12 MPa and a temperature of 300°C [6].

In comparison, the influence of temperature and pH on mineral corrosion is stronger than that of ionic strength and pressure under dynamic conditions, so the coinjection of CO_2 and steam will cause the dissolution of reservoir quartz and the transformation of clay minerals [7, 8]. The chemical changes in reservoir rock structure and composition cause the cementation strength of the weakly consolidated rock to weaken again, so that the reservoir framework fines can migrate under a little shearing action [9, 10]. With the increase of CO_2 and steam injection volume, the skeleton fines continue to peel off, migrate, and flow out, which expands the pore throat radius of the reservoir and further causes steam channelling. As shown in Figure 1, the

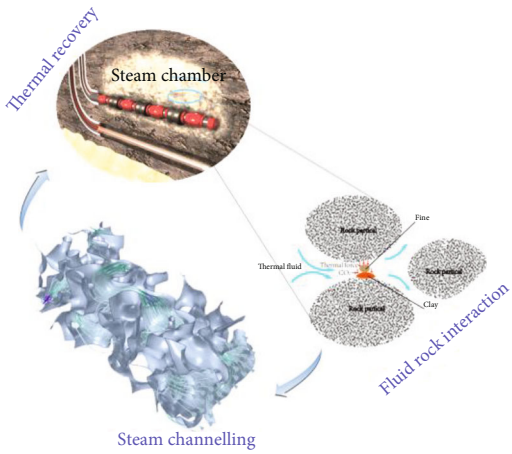

Figure 1: Schematic diagram of reservoir damage during thermal fluid flooding.

Table 1: Initial experimental parameters.

Name	Value	Unit
Salinity of formation water	12000	Mg/L
Pressure after steam injection	4.2	MPa
Crude oil viscosity	996	mPa·s
Average content of clay	12%	
Average reservoir porosity	32.7%	
Average permeability	729.1	mD

formation of the reticulate steam thief region will affect production and make CO_2 storage and utilization less than expected. Previous studies have shown that CO_2 foam can reduce interlayer and intralayer interference and improve the steam displacement effect of a heterogeneous reservoir [11–13]. And foam can slow down the rapid breakthrough of CO_2 to achieve the purpose of thermal CO_2 flooding. Although studies on the physical properties of reservoir rocks caused by the interaction of steam+CO_2 with reservoir rocks have been reported, the study did not mention the effects of thermal force, chemical agent, and gas on the skeleton of the reservoir rock. It is particularly important to study the variation law of reservoir porosity and permeability during multicomponent thermal fluid injection [14, 15].

The CO_2 multicomponent thermal fluid injection method is an enhanced oil recovery technology after single steam injection in weakly consolidated sand reservoirs. With the application of the CO_2 multicomponent thermal fluid injection method, steam channelling intensifies, and sand production near the well area is serious [16, 17]. In addition, the time effect of the water shutoff and controlling profile is short during controlling steam channelling [18]. Thus, we need to understand the porosity and permeability of unconsolidated sandstone using the CO_2 multicomponent thermal fluid injection method. Then, we should study further the interaction between the CO_2 multicomponent thermal fluid and reservoir rock minerals to analyse the mechanism causing the result. According to the physical properties and rock composition of the Zheng 364 reservoir in Shengli Oilfield, the change rules of the reservoir physical properties in CO_2 multicomponent thermal fluid were studied through the water-rock experiment of monomineral, and the mechanism of reservoir physical property change in CO_2 multicomponent thermal fluid was analysed to supplement the mechanism of enhanced oil recovery of the CO_2 multicomponent thermal fluid injection method.

2. Materials and Methods

The experimental instruments were a high-temperature and high-pressure reactor, QBZY-2 interfacial tension meter, Zeiss Sigma 500 field emission scanning electron microscope, Bruke V70 Fourier transform infrared spectrometer, MS603TS/02 electronic balance and ISCO pump, and other displacement equipment.

The surfactant used in the experiment is an anionic surfactant, sodium α-alkenyl sulfonate (AOS) of analytical grade provided by Sinopharm Chemical Reagent Co., Ltd. The monolithic minerals quartz, montmorillonite, illite, and kaolinite are all provided by Hebei Mineral Powder Processing Factory to provide rock blocks and ore powder, including 80 meshes of quartz and 200 meshes of montmorillonite, illite, and kaolinite.

The formation water in the study area is of the $CaCl_2$ type, and the Ca^{2+} concentration is 288 mg/L; the Mg^{2+} concentration is 75 mg/L. The initial parameters of the experiment are shown in Table 1.

2.1. Determination of Optimal Concentration of Surfactant. The oil-water interfacial tension was measured by using the QBZY-2 interfacial tension meter stabilized at a room temperature of 25°C for 20 min, and the foaming volume of AOS at different concentrations was observed for a comprehensive determination of the optimal concentration.

2.2. Monolithic Mineral Hydrothermal Reactions. The surface of the monolithic mineral rock block is polished with a grinding wheel and then rinsed with distilled water; then, the rock block is dried in a drying box at 80°C, and then the four mineral rock blocks are soaked in formation water for 24 hours. Take out the rock blocks and put them into the reaction kettle and fill the whole chamber with distilled water, then adjust the pressure of the reaction kettle to 4.2 MPa, set the temperature to 100°C, 200°C, and 300°C, respectively, and reciprocate the cycle of heating and cooling and introducing CO_2. After 72 hours of reaction, the rock blocks were taken out, rinsed with distilled water, dried at 80°C, weighed, and the percentage of mass change was calculated, which was recorded as the amount of dissolution. Similarly, the distilled water was replaced with the AOS solution at the optimum concentration for the above operations.

2.3. Dynamic Reaction Evaluation. The rock skeleton volume is calculated according to the porosity of the reservoir. Then the quartz density is used to estimate the mass of quartz sand required to achieve this porosity, and finally, a sand pack model with a diameter of 16 mm and a length of 50 mm is made by mixing and filling according to the clay

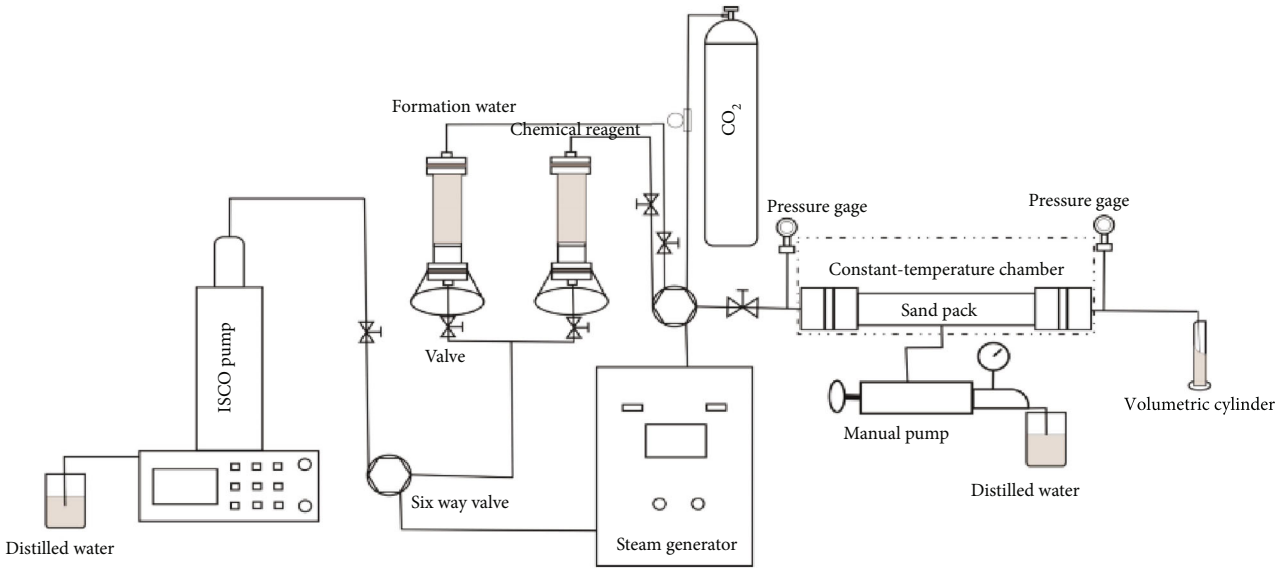

Figure 2: CO_2 multicomponent thermal fluid flooding process.

content contained. Install the instrument as shown in Figure 2, dry the sand pack model, weigh it, vacuum it to saturate the simulated formation water for 8 hours, and weigh it again to calculate the porosity and pore volume. Different temperature steam+CO_2 and steam+CO_2+surfactant AOS flooding experiments were conducted at 0.1 mL/min and inject 200 PV volume multiples. Then, open the nitrogen gas to remove the air in the pipeline, ventilate for 5 minutes to discharge the air and steam condensed water in the sand-filling model, select the inlet and outlet pressure values that meet the conditions of Darcy's law, and then record the atmosphere through the soap film flowmeter. Finally, the gas permeability was calculated by Darcy's formula; the porosity was still measured by saturation weighing. After the flooding, collect the sand sample for scanning with an electron microscope.

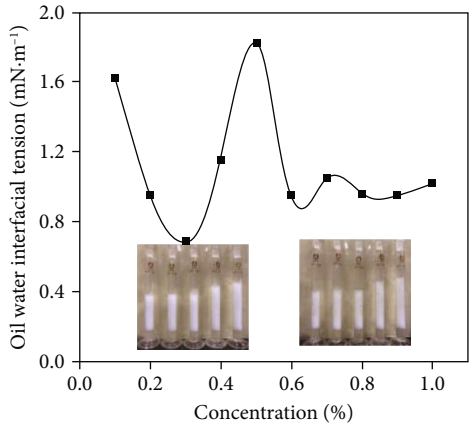

Figure 3: Oil-water interfacial tension of AOS solution at different concentrations.

3. Results and Discussion

3.1. Primary Selection of Surfactant Concentration. Anionic surfactant AOS has good salt resistance, acid and alkali resistance, and temperature resistance characteristics and is a good material for auxiliary chemical agents for thermal recovery. In order to express the experimental effect, parameters such as the foaming effect of aqueous solutions with different concentrations of AOS and the oil-water interfacial tension were evaluated. Ten mass concentrations of 0.1%, 0.2%, 0.3%, 0.4%, 0.5%, 0.6%, 0.7%, 0.8%, 0.9%, and 1% were selected for evaluation, and the results are shown in Figure 3.

With the increase of the concentration, the foaming effect of AOS is getting better and better, and the foam volume increases gradually, but the changing trend of the oil-water interfacial tension is to decrease first and then increase, from 0.1% to 0.3%; the oil-water interfacial tension decreases rapidly. According to the mechanism of surfactant reducing oil-water interfacial tension, the number of AOS molecules adsorbed at the oil-water interface also increases with the increase of concentration and spreads out at the interface one by one, so the interfacial tension decreases [19]. The critical micelle concentration is reached when the molecules spread across the interface, and as the concentration of AOS increases, the number of molecules also begins to increase. At the same temperature, the AOS molecules continue to compete with the AOS molecules at the interface for adsorption, resulting in a change in the interface spreading morphology. This affects the interfacial energy, so the oil-water interfacial tension increases when the concentration exceeds 0.3% [20]. So, the optimal concentration of AOS is 0.3%.

3.2. Static Single Rock Water-Rock Reaction. As shown in Figure 4(a), at 100°C, the mass loss of illite in the CO_2 and distilled water medium is the largest, followed by montmorillonite and kaolinite, and quartz is the least. Although CO_2 is an acid gas, the surface reaction of this mineral is extremely slow. However, the dissolution degree of each

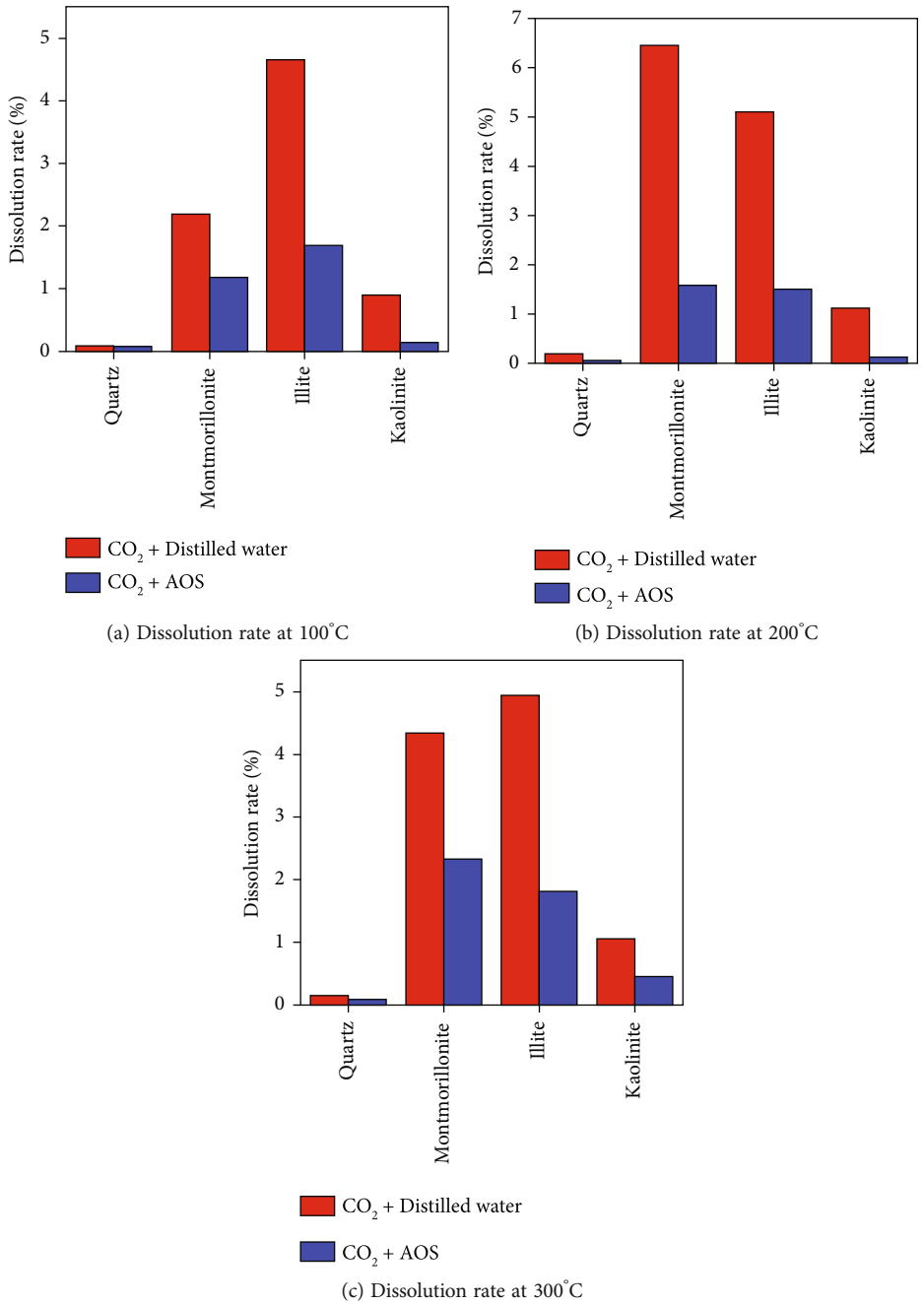

Figure 4: The dissolution rate of minerals at different temperature conditions.

mineral decreases after adding AOS, which indicates that the effect of thermal and CO_2 decreases. As shown in Figure 4(b), when the temperature reaches 200°C, the corrosion amount of illite and montmorillonite is significantly higher than that at 100°C, and the dissolution degree of montmorillonite is higher than that of illite. This is probably because the transformation degree of montmorillonite to the illite mixed layer is higher than that of illite at 200°C. In contrast, the response of kaolinite to temperature is not strong, and AOS has an inhibitory effect on mineral dissolution [21–24]. As shown in Figure 4(c), the corrosion amount of montmorillonite and illite is also the highest, but the corrosion amount of quartz and kaolinite increases slightly. The temperature of mineral dissolution is temperature-responsive, but the response is very slow. In general, the corrosion temperature response of minerals to CO_2 is very obvious, especially clay minerals, and quartz is weaker than that. The inflection points of CO_2 corrosion and AOS inhibition of mineral dissolution at high temperatures appeared at 200°C, which may be related to the temperature response of mineral surface adsorption energy [25, 26].

3.3. Dynamic Hydrothermal Effect. Figure 5 shows the infrared spectra of scattered sand after displacement in different ways.

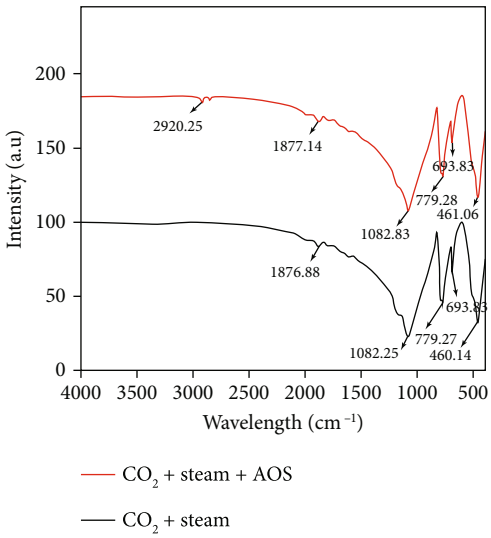

Figure 5: Infrared spectrum of sand with clay.

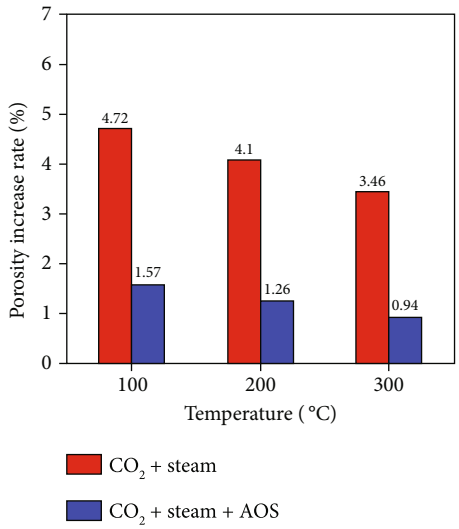

Figure 6: Results for the changes of porosity.

There is a weak C=O absorption vibration peak at 1870 cm^{-1}, and the absorption peak near 1082 cm^{-1} is the stretching vibration of the silicon-oxygen bond and the aluminium-oxygen bond. The absorption peak around 600-800 cm^{-1} is the symmetrical stretching vibration of Al-O and Si-O bonds, and the 460 cm^{-1} is the vibration and bending of the Si-O bond in-plane. However, the bending vibration peak of Si-O-Al, which should have appeared near 500 cm^{-1}, did not appear, so it was concluded that bond breaking occurred under the dual action of high temperature and CO_2. The antisymmetric stretching vibration of the methylene group appeared near 2900 cm^{-1} in the infrared spectrum after CO_2+steam+AOS. This indicates that there is organic matter adsorption in the scattered sand, i.e., AOS is adsorbed on the scattered sand.

The method for measuring porosity is the weighing method, and the benefit of this method is that it can directly reflect fines production or not and the amount of fines production. As shown in Figure 6, the rate of increase in porosity decreases with increasing temperature. The increase in porosity indicates that the volume of the framework decreases. The loss of fines decreases with the increase in temperature, which may be due to the fact that the pores of the rock are compressed at high temperatures, and the pore size decreases, so that some migrating fines cannot flow out [27, 28]. When AOS was added, the response of the porosity change was not obvious with temperature. Besides, the difference in temperature response to porosity change during CO_2+steam injection is 0.63% on average, while the difference in temperature response to porosity change during CO_2+steam+AOS injection is 0.315% on average. It can be seen that the temperature response to porosity change is reduced by half after AOS injection.

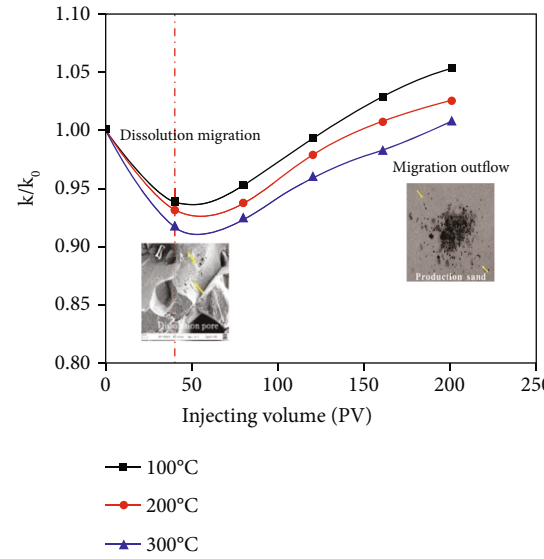

Figure 7: Changes in permeability of CO_2+steam.

3.3.1. Permeability Change. As shown in Figure 7, the permeability of the sand pack model at different temperatures first decreased and then increased, and the raise speed decreases gradually. With the increase in temperature, the degree of migration blockage increases, and the permeability recovery becomes slow. The permeability decreases within the injected volume of 40 PV, which may be due to the displacement of fines caused by fluid shear or the reduction of pore radius due to the expansion of clay due to water absorption; this effect is greater than that of fines production, thereby reducing permeability. It can be seen from the quartz electron microscope pictures of CO_2 treatment at 200°C that local pitting does occur, and the degree is not high, but it is enough to reduce the interaction force between particles. Under the action of fluid drag force, fines are easy to migrate. In general, the permeability results are reduced within the injected volume of 40 PV, and the permeability will recover and continue to increase when the fluid is continuously injected. It may be because the fines production effect is greater than the internal fines migration and expansion of clay. In addition, this permeability "recovery" is not

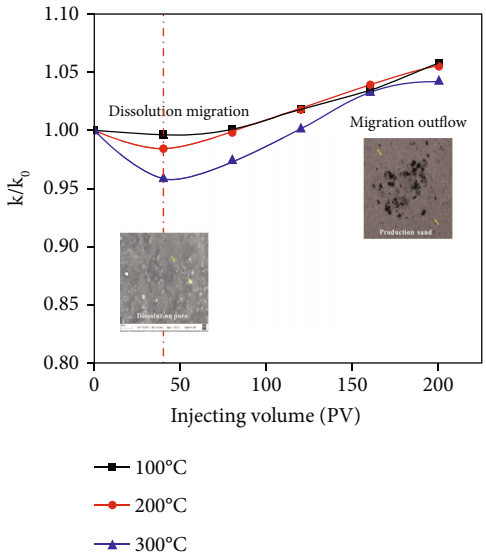

Figure 8: Changes in permeability of CO_2+steam+AOS.

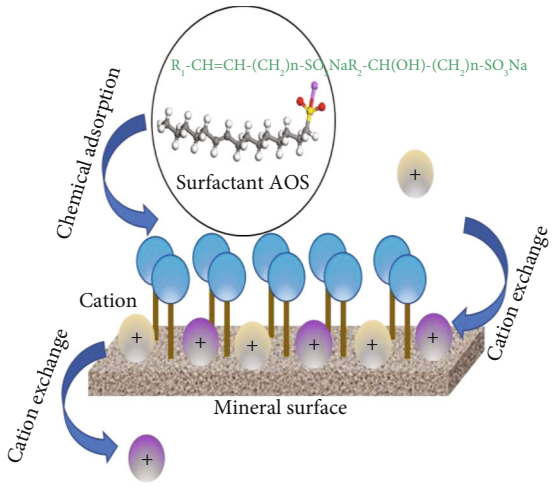

Figure 9: Rock protects the mechanism of CO_2+steam+AOS.

only negative but also means channelling of injection fluid, which can even aggravate the sand production degree near the well. The permeability "recovery" becomes slower with increasing temperature, which may be due to a decrease in fluid viscosity and a decrease in drag force with increasing temperature [29].

As shown in Figure 8, after adding AOS, the degree of migration in the migration stage is significantly reduced, and the overall permeability changes little; the permeability changes by about 0.5%, so the protective effect of surfactant AOS on the reservoir is obvious. Although the degree of migration increases with the increase in temperature, it is improved compared with that when AOS is not added, and it can be seen from the quartz electron microscope pictures treated with CO_2+AOS at 200°C that the degree of corrosion is much smaller. From the figure and the number of fines produced, it can also be shown that the chemical agent has a certain effect on the stability of the rock particles. From the infrared spectrum in Figure 5, it can be seen that the anionic surfactant AOS is adsorbed on the rock surface of the reservoir, and it shows the stability of porosity and permeability in rock physical properties as shown in Figure 8, while the porosity and permeability of the rock not adsorbed by AOS change greatly as shown in Figure 7, indicating that the role of chemical reagents in the tertiary oil recovery mechanism of CO_2 multicomponent thermal fluid is to act on the fluid on the one hand and stabilize the rock skeleton on the other hand. Its mechanism is shown in Figure 9. The ion exchange between rock mineral ions and cations in formation water makes the mineral surface absorb a large number of cations, which provides conditions for anionic surfactants to form a "protective layer."

4. Conclusions

Different minerals have different temperature responses to CO_2. It is difficult for CO_2 to dissolve quartz in a short time at high temperatures, and the dissolution rate is only about 0.1%, but the dissolution of clay is very strong. The degree of dissolution from large to small is illite, montmorillonite, and kaolinite, and the dissolution rate is above 1%. When AOS is added, this interaction is slowed down, and the dissolution rate becomes smaller.

During CO_2+steam injection, the porosity of the sand pack is inversely proportional to the temperature. AOS reduces the temperature response of the difference in porosity by half compared with that of CO_2+steam so that the reservoir porosity can be guaranteed not to change much during the superheated steam injection process. The change in permeability shows a trend of first decreasing and then increasing, which reflects the two migration stages of framework fines in the reservoir. Dissolution and migration as a leading factor or the migration of outflowing sand production become chief factors. The adsorption of AOS on the rock surface significantly slows down the damage of CO_2 to the rock under high-temperature steam, thereby improving the sudden change in permeability. Although there is still corrosion in steam+CO_2+AOS, this ensures that a part of CO_2 is stored in the reservoir, which also achieves the purpose of reducing CO_2 emissions.

The CO_2 multicomponent thermal fluid injection method is feasible in the subsequent development of thermal recovery of heavy oil reservoirs. On the basis of the fluid action mechanism, the CO_2 multicomponent thermal fluid injection method is supplemented to enhance the oil recovery mechanism. Especially, the steam+CO_2+AOS compound method can effectively alleviate the permeability heterogeneity in the unconsolidated sandstone and effectively reduce the degree of steam channelling.

Data Availability

The raw data used to support the conclusions of this study are available from the corresponding author upon request.

Conflicts of Interest

The authors declare that they have no conflicts of interest to report regarding the present study.

Acknowledgments

This work was financially supported by the National Natural Science Foundation of China (U20B6003).

References

[1] J. Hillier, C. Walter, D. Malin, T. Garcia-Suarez, L. Mila-i-Canals, and P. Smith, "A farm-focused calculator for emissions from crop and livestock production," *Environmental Modelling & Software*, vol. 26, no. 9, pp. 1070–1078, 2011.

[2] M. Adam, H. Anbari, A. Hart, J. Wood, J. P. Robinson, and S. P. Rigby, "In-situ microwave-assisted catalytic upgrading of heavy oil: experimental validation and effect of catalyst pore structure on activity," *Chemical Engineering Journal*, vol. 413, article 127420, 2021.

[3] M. L. Godec, V. L. Kuuskraa, and P. Dipietro, "Opportunities for using anthropogenic CO2for enhanced oil recovery and CO2 storage," *Energy & Fuels*, vol. 27, no. 8, pp. 4183–4189, 2013.

[4] Y. Z. Liu, Z. Rui, T. Yang, and B. Dindoruk, "Using propanol as an additive to CO_2 for improving CO_2 utilization and storage in oil reservoirs," *Applied Energy*, vol. 311, p. 118640, 2022.

[5] Y. Liu and Z. Rui, "A storage-driven CO2 EOR for a net-zero emission target," *Engineering*, vol. 18, pp. 79–87, 2022.

[6] X. Dong, H. Liu, Z. Chen, K. Wu, N. Lu, and Q. Zhang, "Enhanced oil recovery techniques for heavy oil and oilsands reservoirs after steam injection," *Applied Energy*, vol. 239, pp. 1190–1211, 2019.

[7] X. Dong, X. Jiang, W. Zheng et al., "Discussion on the sweep efficiency of hybrid steam–chemical process in heavy oil reservoirs: an experimental study," *Petroleum Science*, vol. 19, no. 6, pp. 2905–2921, 2022, in press.

[8] G. Bird, J. Boon, and T. Stone, "Silica transport during steam injection into oil sands: 1. Dissolution and precipitation kinetics of quartz: new results and review of existing data," *Chemical Geology*, vol. 54, no. 1-2, pp. 69–80, 1986.

[9] S. E. Taylor, "Interfacial chemistry in steam-based thermal recovery of oil sands bitumen with emphasis on steam-assisted gravity drainage and the role of chemical additives," *Colloids and Interfaces*, vol. 2, no. 2, p. 16, 2018.

[10] R. G. S. Araújo, J. L. A. O. Sousa, and M. Bloch, "Experimental investigation on the influence of temperature on the mechanical properties of reservoir rocks," *International Journal of Rock Mechanics and Mining Sciences*, vol. 34, no. 3-4, pp. 298.e1–298.e16, 1997.

[11] X. Dong, H. Liu, and Z. Chen, "Existing problems for steam-based enhanced oil recovery processes in heavy oil reservoirs," in *Hybrid Enhanced Oil Recovery Processes for Heavy Oil Reservoirs*, vol. 73 of Developments in Petroleum Science, , pp. 47–98, Elsevier, 2021.

[12] J. Fan, J. Yang, X. Fan, and L. Wu, "Experimental study on the mechanism of enhanced oil recovery by noncondensable gas-assisted steam flooding process in extra-heavy oil reservoir," *Energy Sources, Part A: Recovery, Utilization, and Environmental Effects*, vol. 43, no. 4, pp. 444–460, 2021.

[13] M. Guo, H. Liu, Y. Wang, H. Zhang, J. Wang, and X. Dong, "Sand production by hydraulic erosion during multicycle steam stimulation: an analytical study," *Journal of Petroleum Science and Engineering*, vol. 201, article 108424, 2021.

[14] X. I. Changfeng, Q. I. Zongyao, Y. Zhang et al., "CO_2 assisted steam flooding in late steam flooding in heavy oil reservoirs," *Petroleum Exploration and Development*, vol. 46, no. 6, pp. 1242–1250, 2019.

[15] Y. Liu, R. B. Grigg, and B. Bai, "*Salinity, pH, and surfactant concentration effects on CO2-foam*," Paper presented at the SPE International Symposium on Oilfield Chemistry, The Woodlands, Texas, 2005.

[16] H. D. Nejatian, E. Khodapanah, and E. Sahraei, "Experimental investigation of steam-CO2-foam flooding: combination of CO2-foam flooding and steam injection as an effective enhanced oil recovery (EOR) method in heavy oil reservoirs," *Asia-Pacific Journal of Chemical Engineering*, vol. 10, no. 3, article 377386, 2015.

[17] Z. Qi, T. Liu, C. Xi et al., "Status quo of a CO_2-assisted steam-flooding pilot test in China," *Geofluids*, vol. 2021, Article ID 9968497, 13 pages, 2021.

[18] C. Yanbin, L. Dongqing, Z. Zhang, W. A. Shantang, W. Quan, and X. Daohong, "Steam channeling control in the steam flooding of super heavy oil reservoirs, Shengli Oilfield," *Petroleum Exploration and Development*, vol. 39, no. 6, pp. 785–790, 2012.

[19] J. Zhao, F. Torabi, and J. Yang, "The role of emulsification and IFT reduction in recovering heavy oil during alkaline-surfactant-assisted CO_2 foam flooding: an experimental study," *Fuel*, vol. 313, article 122942, 2022.

[20] M. D. Reichert and L. M. Walker, "Interfacial tension dynamics, interfacial mechanics, and response to rapid dilution of bulk surfactant of a model oil–water-dispersant system," *Langmuir*, vol. 29, no. 6, pp. 1857–1867, 2013.

[21] D. B. Bennion, F. Thomas, and D. Sheppard, "Formation damage due to mineral alteration and wettability changes during hot water and steam injection in clay-bearing sandstone reservoirs," Paper presented at the SPE Formation Damage Control Symposium, Lafayette, Louisiana, 1992.

[22] J. Han, F. Feng, M. Yan, Z. Cong, S. Liu, and Y. Zhang, "CO_2-water-rock reaction transport via simulation study of nanoparticles-CO_2 flooding and storage," *Sustainable Energy Technologies and Assessments*, vol. 50, article 101736, 2022.

[23] Y. Sun, L. Zhao, T. Lin et al., "Enhance offshore heavy oil recovery by cyclic steam-gas-chemical costimulation," *Paper Presented at the SPE Heavy Oil Conference and Exhibition*, 2011, Kuwait City, Kuwait, 2011, 2011.

[24] D. Watkins, L. Kalfayan, D. Watanabe, and J. A. Holm, "Reducing gravel pack and formation dissolution during steam injection," *SPE Production Engineering*, vol. 1, no. 6, pp. 471–477, 1986.

[25] B. Fermaniuk, M. Claerhout, and D. Zhu, "In-situ SAGD thermal-chemical effects and metal-bond coated slotted liner design for enhanced sand control, flow and long-term performance," Paper presented at the SPE Thermal Well Integrity and Design Symposium, Banff, Alberta, Canada, 2015.

[26] M. A. Tabar, H. Bagherzadeh, A. Shahrabadi, and S. Dahim, "A comprehensive research in chemical consolidator/stabilizer agents on sand production control," *Journal of Petroleum Exploration and Production Technology*, vol. 11, no. 12, pp. 4305–4324, 2021.

[27] V. Lightbown, "New SAGD technologies show promise in reducing environmental impact of oil sand production," *Journal of Environmental Solutions for Oil, Gas, and Mining*, vol. 1, no. 1, pp. 47–58, 2015.

[28] D. Xiao-Hu and L. Hui-Qing, "Investigation of the features about steam breakthrough in heavy oil reservoirs during steam injection," *The Open Petroleum Engineering Journal*, vol. 5, no. 1, pp. 1–6, 2012.

[29] F. Bruns and T. Babadagli, "Heavy-oil recovery improvement by additives to steam injection: identifying underlying mechanisms and chemical selection through visual experiments," *Journal of Petroleum Science and Engineering*, vol. 188, article 106897, 2020.

Hindawi
Geofluids
Volume 2023, Article ID 9740015, 12 pages
https://doi.org/10.1155/2023/9740015

Research Article

Experimental Study on the Distribution of Retained Fracturing Fluids and Its Effect on the Permeability and Wettability in Tight Oil Reservoirs

Tuan Gu,[1] **Zhilin Tuo**,[2] **Tao Fan**,[1] **Dongpo Shi**,[1] **Chun Mu**,[1] **Shucan Xu**,[3] **and Desheng Zhou**[3]

[1]*Research Institute of Petroleum Exploration and Development, Liaohe Oilfield Company of Petro, China*
[2]*Gas Recovery Plant No.2, PetroChina Changqing Oilfield Company, China*
[3]*College of Petroleum Engineering, Xi'an Shiyou University, China*

Correspondence should be addressed to Desheng Zhou; x13689261423@163.com

Received 14 November 2022; Revised 25 November 2022; Accepted 21 March 2023; Published 24 April 2023

Academic Editor: Daoyi Zhu

It is not clear how the distribution of retained fracturing fluids and its effect on the permeability and wettability in tight oil reservoirs interact. Especially, there are more qualitative studies and less quantitative studies on this issue. Under laboratory experimental conditions, this paper clarifies the distribution of retained fracturing fluids in the core and reveals the influence rule of retained fracturing fluids on tight reservoir permeability and wettability. It is found that the main retention space of retained fracturing fluids in a tight reservoir is a microporous interval, and the residual oil after oil displacement by retained fracturing fluids mainly exists in the core in the form of dots or porphyries. The smaller permeability and porosity of the core will lead to more retained fracturing fluids. The permeability of different cores after fracturing fluid retention has decreased to varying degrees compared with that before fracturing fluid retention. The wettability of core slices before and after fracturing fluid retention was tested, and the effect of retained fracturing fluids on reservoir wettability was not significant. This study has important significance for improving the recovery of tight oil reservoirs and enhancing the understanding of postfracturing fluid retention.

1. Introduction

The tight oil is widely distributed and has huge reserves in China and will gradually become the main force in the supply of oil and gas resources [1]. However, the compaction of a tight oil reservoir is strong in the diagenesis [2]. Because the rock is dense and the particles are small, the porosity and permeability of the reservoir are low and the physical properties are relatively poor, which brings a series of problems to the development of a tight oil reservoir [3]. The combination technology of hydraulic fracturing and long horizontal well is the most effective method to develop a tight oil reservoir at present [4].

During the fracturing, a large amount of fracturing fluids are injected into the formation, and the flow-back rate is usually low [5]. A large amount of fracturing fluids is retained in the formation, and previous researches on fracturing fluid retention in the formation have been conducted. Williams [6] divided the retention process of fracturing fluids into three stages: nonformation of filter cake, formation of filter cake, and dynamic filtration. Yew et al. [7] considered the influence of natural fractures existing in low permeability reservoirs on fracturing fluid retention based on the research of Economides. Rodgerson [8] studied and analyzed the fracturing fluid retention state of the reservoir when there are natural fractures. However, due to its complex conditions, this study did not obtain an effective retention model for natural fracture reservoirs. Outmans [9] proposed a model including the relationship between porosity, compressibility and pressure, and permeability to predict

dynamic filtration. It is found that the dynamic filtration rate is independent of the shear rate when the mud dynamic filtration reaches equilibrium. Vinod et al. [10] calculated that the microparticles in the fluids will block the rock pores, block the fluid flow, and cause damage to the formation to some extent. It is concluded that the effective permeability of the formation is related to the polymer, and the polymer will cause additional pressure difference to the fracturing fluid filtration. Mathias and Van Reeuwijk [11] proposed one-dimensional and two-dimensional fracturing fluid filtration calculation models. The calculation results are far from the actual filtration situation, and the simulation effect is poor. For tight reservoirs, the fracturing fluid retention has a serious impact on the physical properties of the reservoir. At present, the research on the fracturing fluid retention is mainly focused on establishing the mathematical model of the retention and correcting the model, but the method of the impact of the retention on the physical properties of rocks by means of indoor core experiments has not been adopted [12, 13].

Two important parameters related to the physical properties of tight reservoir rocks include permeability and wettability [14]. In 1964, Pirson et al. [15] proposed a model for calculating relative permeability from resistivity, tested their model through experimental data, and adjusted the model under different conditions with different correction coefficients. For example, the gas-water model is different from the oil-water model. Through the optimization of permeability modeling, accurate permeability parameters are obtained. The prediction methods for permeability are mainly divided into two categories: one is statistical modeling based on core analysis data, and the other is the learning modeling method using data mining. Akande et al. [16] established a permeability prediction model based on the random selection of particle swarm optimization algorithm, combined with support vector function to simplify the regression problem, and improved the generalization ability and prediction accuracy of the model. Purcell [17] established the Purcell model applicable to sandstone reservoir; Thomeer [18, 19] established the Thomeer model applicable to sandstone reservoir; Kolodzie [20] divided the petrophysical category of sandstone reservoir and carbonate reservoir with the corresponding pore throat radius when the mercury inflow saturation is 35% and established the Winland-r35 model. Since then, other scholars such as Rezaee et al. [21] have studied tight sandstone gas reservoirs in Western Australia and found that the correlation between the corresponding pore throat radius and permeability is the highest when the mercury inflow saturation is 10%; Min et al. [22] believed that when the stress is small, the permeability of broken rock decreases with the increase of stress amplitude, while when the stress ratio is large enough, the permeability increases with the increase of stress. Larsen et al. [23] pointed out that the geological tectonic field has a great impact on the permeability of carbonate rocks, and the tensile stress caused by fracture is helpful to increase the permeability of carbonate rocks. In fact, a large amount of retained filtration fracturing fluids can change the state of tight reservoir rocks, such as the generation of new microfractures, which will lead to significant changes in permeability. There are more qualitative studies than quantitative studies on this issue.

Rock wettability is one of the important characteristics of rock physics [24]. The nuclear magnetic resonance T2 spectrum is commonly used to reflect the pore size distribution of hydrophilic rocks, but when the rock wettability changes, the nuclear magnetic resonance response based on the position of fluid relative to the rock pore surface will change [25, 26]. Howard [27] was the first to attempt to evaluate the wettability of reservoir rocks by quantitative means and to establish a relationship between the relaxation movement of saturated water and water saturation and wettability. Straley et al. [28] introduced the wetting parameters and oil saturation into the surface relaxation formula and established the relationship between the relaxation time and the surface relaxation rate, specific surface area, oil saturation, and wetting parameters. In 2003, Fleury and Deflandre [29] proposed an NMR wettability index that is more consistent with the physical properties of rocks; however, this method requires complete separation of T2 relaxation of oil and water. Guan et al. [30] proposed to quantitatively indicate the wettability characteristics of reservoir rocks by using the change of the arithmetic mean value of nuclear magnetic relaxation time before and after oil flooding and water flooding. The calculation result of this method is different from the value range of the Amott index, so it is impossible to directly make a numerical comparison. Al-Mahrooqi et al. [31] published an article on the evaluation of rock wettability in 2006 by combining nuclear magnetic resonance experiments and numerical simulation. By establishing a capillary bundle seepage model of triangular interface considering liquid-solid interaction, the expression of nuclear magnetic resonance T2 spectrum under different displacement pressures (i.e. different microdistribution of oil and water) was derived, and the influence of different wettability on nuclear magnetic resonance response was quantitatively explained from the rock pore size. Johannesen et al. [32] proposed to calculate the difference between the relaxation time corresponding to the peak value of the right peak of T2 relaxation spectrum of saturated oil state in other wettability states of cores and the standard based on the relaxation time corresponding to the peak value of the right peak of T2 relaxation spectrum of saturated oil state in strong hydrophilic cores as the evaluation parameter of rock wettability. Chen et al. [33] found that the change of the effective surface relaxation rate of oil or water in saturated uncompacted silica sand or calcite porous media was in good agreement with the wetting size measured by the contact angle and proposed to establish the nuclear magnetic resonance wetting index by obtaining the effective surface relaxation rate from the T2 surface relaxation term. Minh et al. [34] proposed a study on rock wettability based on restricted diffusion, which can be applied to downhole measurement. Rabiei et al. [35] studied the thickness of the water film on the sandstone wall when water and oil exist at the same time and believed that after the water film was stripped, the crude oil directly contacted the sandstone surface, so the sandstone surface showed part of the oil wet, while other parts were still wet. Pratten and

Craig [36] believed that neutral wettability existed in most reservoirs, which are neither lipophilic nor hydrophilic, and there is no strong selectivity for both. Gachot et al. [37] pointed out that the rock surface with strong hydrophilicity will change to weak hydrophilicity after contacting with crude oil, and the small pores in the core are mostly water wet, while the water wetness of large pores is relatively weak. Therefore, it is necessary to test the influence of fracturing fluid retention on reservoir wettability through a more reasonable experimental design and method.

Under laboratory experimental conditions, this paper studies the influence of retained fracturing fluids on reservoir physical properties by using core thin section and nuclear magnetic resonance technology, clarifies the distribution rule of retained fracturing fluids in core, and reveals the influence rule of retained fracturing fluids on tight reservoir permeability and wettability. This study has important reference significance for improving the recovery of tight oil reservoirs and enhancing the understanding of postfracturing fluid retention.

2. Materials and Methods

2.1. Experimental Materials. The materials used in this study include rock slices and rock column samples, which are, respectively, used to carry out thin section observation experiments and permeability evolution experiments. The basic parameters of the slices used are shown in Table 1. The diameter is about 2.5 cm, the thickness is 1 mm to 3 mm, and the permeability is generally low. As shown in Table 2, the column samples are more than 4 cm in length, less than 10% in porosity, and higher in permeability. In addition, the experimental materials also include simulated retained fracturing fluids, kerosene, $MnCl_2$ solution, and other liquid materials.

2.2. Experimental Method. In order to study the oil-water distribution in tight oil reservoirs after fracturing, nuclear magnetic equipment is used for monitoring [38]. The instrument used in the experiment is MesoMR23-60H-I low-field NMR analyzer, and the manufacturer is Suzhou Niumag Analytical Instrument Corporation. The magnet type is a permanent magnet. The magnetic field intensity is 0.5 ± 0.05 T. The probe coil is 25 mm. The magnet temperature is 32°C. The dominant frequency of the instrument is 23 MHz. The sample size should be 25 mm in diameter and about 50 mm in length. The ambient temperature is 15-25°C, and the relative humidity is 50-70%, as shown in Figure 1. Laboratory experiments were carried out on the tight sandstone core of Chang 7 Member of Yanchang Formation in Ordos Basin, using nuclear magnetic resonance technology, scanning electron microscopy, casting thin section and mirror observation photography, and other technical means.

In order to prevent the influence of hydrogen signal in distilled water on the oil signal in the core, the experimental liquid is a manganese chloride solution with a mass fraction of 40%. This is because after the divalent manganese ions fully diffuse into the core pores, the water signal will be shielded, and manganese chloride is not soluble in oil, so the oil signal will not be affected [39]. In this way, the water and oil signals will be separated to facilitate T2 spectrum observation. The experimental process and equipment are shown in Figure 2. The main test steps are as follows: (1) use the wire cutter to cut the core into thin slices (1-2 mm thickness) of the required size and put the core into a 70°C thermostat until the dry weight of the slices does not change. Measure the diameter, thickness, quality, permeability, and other basic parameters of the thin film and photograph the dry thin film samples in full view and local view with a stereoscopic microscope. (2) Pressurize and saturate the dried core slice to simulate formation water condition for 24 h to obtain the core slice saturated with water. Scan and image the saturated core slice by nuclear magnetic resonance to obtain the T2 spectrum and imaging image of saturated water. Dry the scanned core in a constant temperature oven at 70°C, and then saturate the core slice in the configured 40% manganese chloride solution. (3) Put the core slice

Table 1: List of core slice parameters.

No.	Diameter/mm	Thickness/mm	Weight/g	Permeability/mD
A-1	25.37	2.57	2.295	0.024
A-2	25.33	1.97	1.887	0.091
A-3	25.33	2.53	2.664	0.034
A-4	25.34	2.18	2.247	0.088
A-5	25.33	2.11	2.148	0.034
B-4	25.36	1.81	1.776	0.029

Table 2: Basic parameters of the experimental core.

No.	Length (cm)	Diameter (cm)	Weight (g)	Porosity (%)	Permeability (mD)
E-1	4.486	2.517	59.144	7.21	0.564
E-2	4.064	2.525	51.726	6.35	0.535
E-3	4.128	2.536	53.733	3.97	0.278
E-4	4.825	2.528	62.860	6.85	0.494
E-5	4.503	2.509	55.655	4.67	0.389

Figure 1: Low-field NMR analyzer.

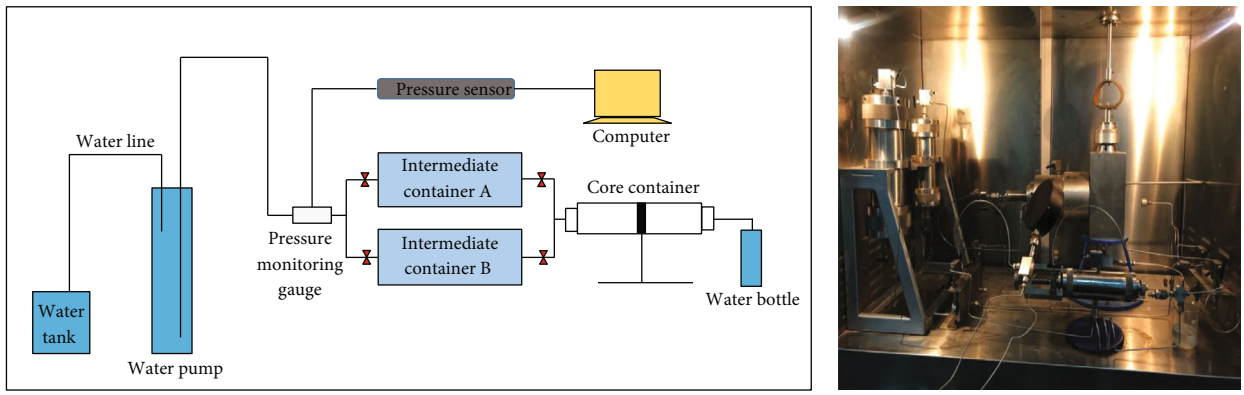

(a) Physical diagram (b) Schematic diagram

Figure 2: Core flow chart.

saturated with 40% manganese chloride solution into the nuclear magnetic resonance analyzer for scanning and imaging and get the T2 spectrum and imaging map of saturated manganese. Then, use the stereoscopic microscope to take pictures in full and local view. Put the core slice after the experiment into the displacement device to start oil flooding to the outlet end without water and create the bound water state of the core. (4) Put the core slice with bound water into the nuclear magnetic resonance analyzer for scanning and imaging, obtain the T2 spectrogram and imaging image, and use the stereoscopic microscope to take pictures in a full field of view and local field of view. (5) Put the original oil-bearing core slices in the irreducible water state into the displacement device and displace them with 40% manganese chloride solution to the outlet end without oil production, scan and image them with the nuclear magnetic resonance analyzer, and take photos with the stereoscopic microscope. (6) Use oil to reverse drive the core slice after water flooding to the outlet without water. Use the MRI analyzer for scanning and imaging, and then use the stereoscopic microscope for taking pictures [40].

In order to study the effect of retained fracturing fluids on the permeability of a tight reservoir, a permeability monitoring experiment after fracturing fluid retention was carried out. The experimental steps are as follows: (1) cut the core into the size required by the experiment, wash the oil, dry the core, and measure its dry weight and size; (2) gas logging core porosity and permeability; (3) pressurize the core to 20 MPa saturated water; (4) displace the saturated kerosene by the core, and weigh its wet weight to calculate the porosity and permeability; (5) put the core into the displacement device to start water drive oil until the outlet end is no longer producing oil. Record the volume of oil expelled V1. At this time, the volume of oil expelled is equal to the volume of water retained in the core. For water drive cores, this process simulates the fracturing fluid retention into the formation during development; (6) oil reversely displaces water until there is no water at the outlet end. Record the volume of water expelled, V2. This process simulates the process of oil entering the wellbore after fracturing. At this time, the water loss in the core should be V1-V2.

In order to analyze the influence of fracturing fluids on reservoir wettability, the cores before and after fracturing fluid retention were treated with saturated water and saturated oil, and nuclear magnetic resonance scanning was performed on them. The NMR data of fracturing fluids before and after fracturing fluid retention are used to analyze the change of core mixing wettability. The specific steps are as follows: (1) wash and dry the compact rock sample slices; (2) test the T2 relaxation time spectrum of NMR after the core is saturated with simulated formation water condition; (3) displace the saturated water core by 40% $MnCl_2$ solution to shield the water phase signal in the core and scan the core again by NMR, reducing the signal to less than 1% of the original signal; (4) put the rock sample in the displacement device, and then conduct oil displacement water experiment until there is no water output at the outlet end, and establish irreducible water saturation; (5) measure the T2 atlas of saturated oil cores in the original formation state and compare the T2 relaxation time atlas in the saturated simulated formation water state with it; (6) repeat the above steps for the core slice after fracturing fluid retention to obtain T2 relaxation time atlas of saturated water and saturated oil after fracturing fluid retention.

3. Experimental Results and Discussion

3.1. Oil-Water Distribution in Tight Oil Reservoirs after Fracturing. Figure 3 shows the pseudocolor NMR images of different stages of core slice A-1. Except for the images of saturated samples, the other images only reflect the strength of oil signals. The signal of the A-1 oil displacement manganese water sample of the core slice is not as strong as that of the saturated water sample, which indicates that manganese water is not completely driven out during oil displacement, and there is still a lot of bound water in the micropores of the core slice. However, the water drive oil sample signal of core slice A-1 decreases again, indicating that a large amount of oil is displaced to the outside by the differential pressure of displacement, and only a small part of the oil remains in the core slice. When it comes to oil reverse displacement, although the signal strength is enhanced, it cannot reach the

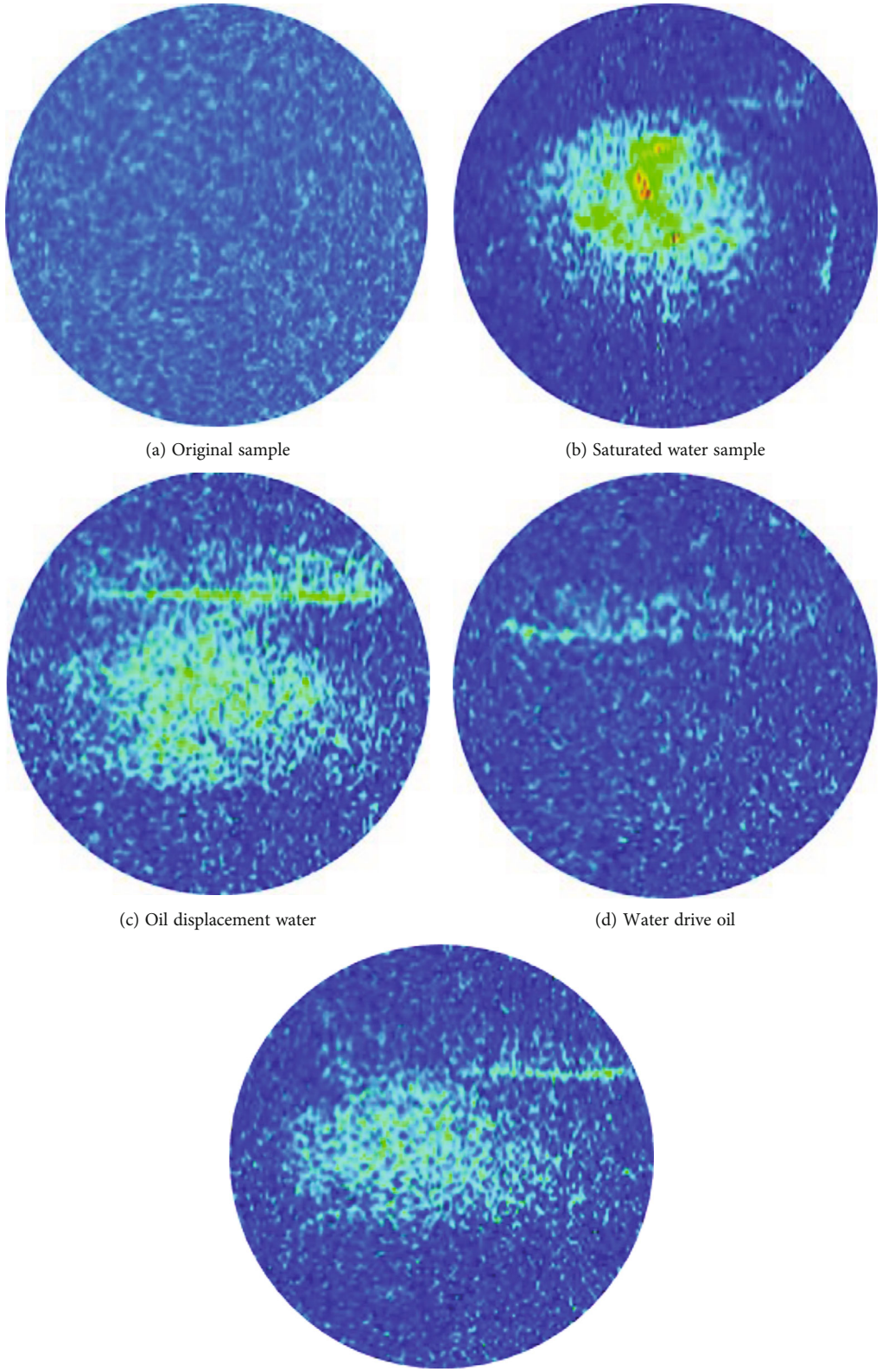

(a) Original sample

(b) Saturated water sample

(c) Oil displacement water

(d) Water drive oil

(e) Oil reverse displacement water

Figure 3: Pseudocolor NMR images of different stages of core slice A-1.

signal strength under the original oil saturation state, indicating that it is difficult for oil to enter the pores filled with fluid again, and most of the oil and water in the macropores can only move along the direction of the pore path with small capillary resistance, which results in a large amount of water remaining in the reservoir due to retention [41].

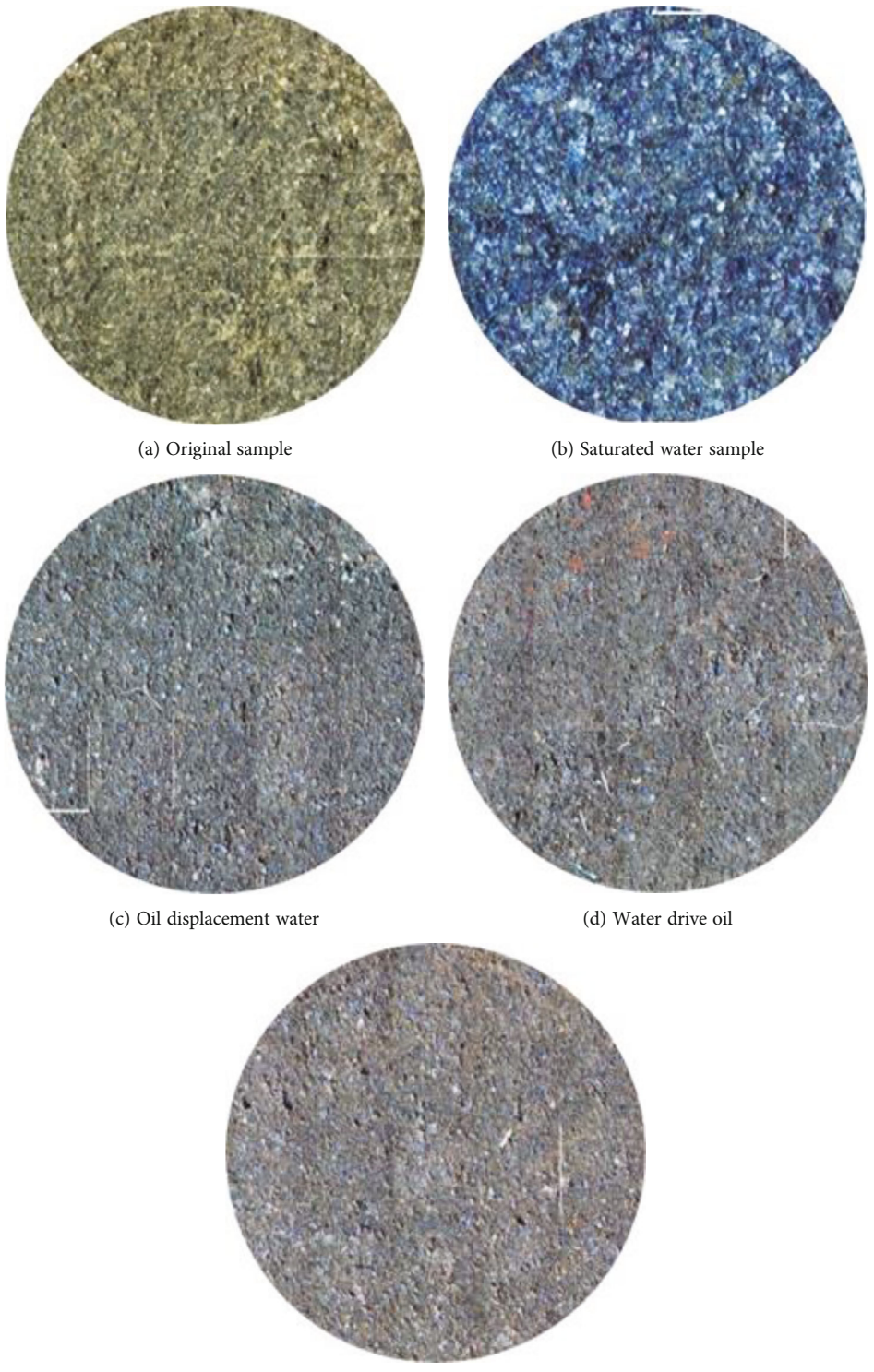

(a) Original sample

(b) Saturated water sample

(c) Oil displacement water

(d) Water drive oil

(e) Oil reverse displacement water

Figure 4: Photographic images for the stereoscopic microscope of different stages of core slice A-1.

The following images which are taken with a stereoscopic microscope can be more intuitive to see the distribution of retained fracturing fluid in the core slice. Figure 4 shows the photographic images for the stereoscopic microscope of different stages of core slice A-1. After oil displaces manganese water, the blue color on the thin slice obviously fades, indicating that a large amount of oil has saturated into the inner part of the slice.

Figure 5 shows the local enlarged view of core slice A-1 after oil displacing manganese water. The position of the black circle in the figure is red kerosene saturated into the inner part of the sheet, but there are still many blue parts

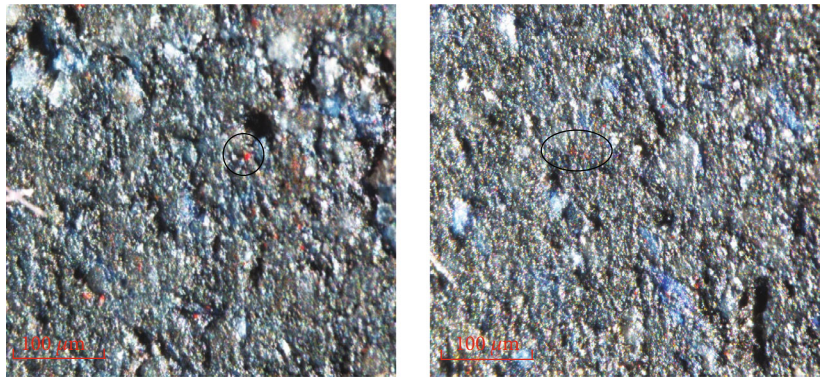

Figure 5: Local enlarged view of core slice A-1 after oil displacing manganese water.

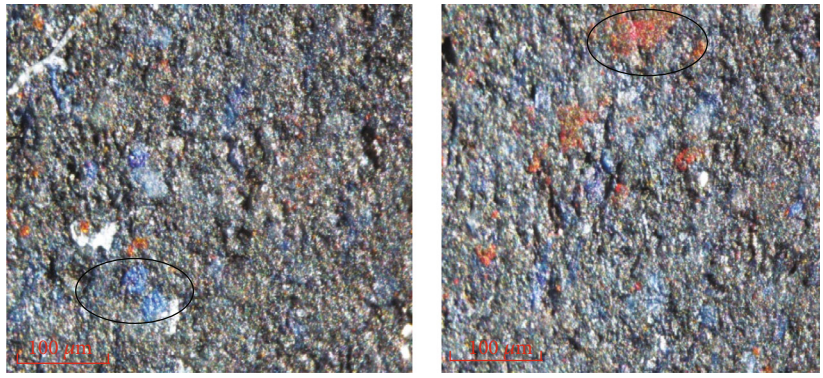

Figure 6: Local enlarged view of core slice A-1 after water flooding.

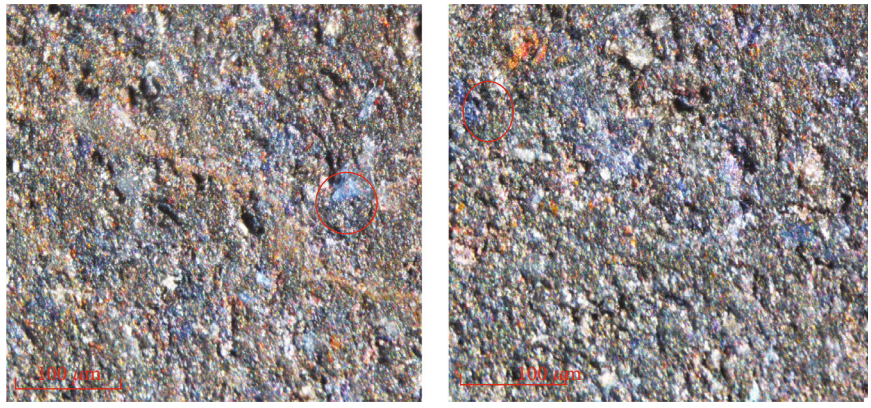

Figure 7: Local enlarged view of core slice A-1 after oil reverse displacement.

in the figure, indicating that there is still a large amount of manganese water in the sheet at this time. The blue parts in the figure are dark and light, indicating the different bound water volumes, which is due to the overlapping of porosity phases in the picture. The three-dimensional distribution of pores in the sheet is very obvious, and there are many small pores developed.

Figure 6 shows the local enlarged view of core slice A-1 after water flooding. The position of the black circle in the figure is the residual oil after water flooding. The residual oil is mainly concentrated in the small and medium-sized pores. In the extremely small pores, because the oil is basically not saturated into the oil when saturated, there is very little residual oil in the too-small pores, and the oil in the large pores is basically expelled by water, so there is less residual oil in the large pores. During displacement, microfingering will occur, that is, the retained fracturing fluids will easily move along the direction of low capillary resistance and high permeability. When multiple projecting water phase channels are closed, there will be a large amount of residual oil in the area between the water channel and the water channel that is not swept by the injected water. A large amount of residual oil mainly exists in the matrix that is not swept by water in the form of spots, and some residual oil

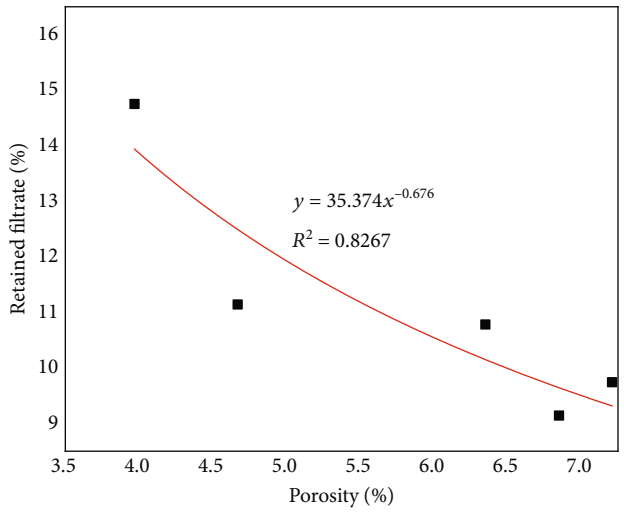

Figure 8: Relationship between fracturing fluid retention and porosity.

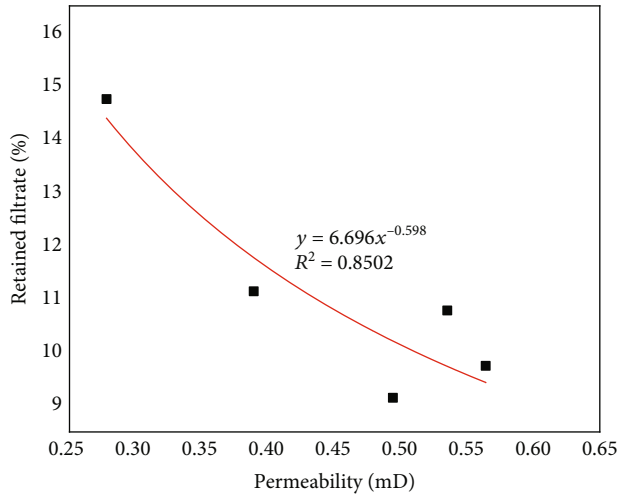

Figure 9: Relationship between fracturing fluid retention and permeability.

exists in the matrix that is easy to flow in the form of mutual infection of oil and water.

Figure 7 shows the local enlarged view of core slice A-1 after oil reverse displacement, and the red circle represents the retained fracturing fluids trapped in the core. It can be seen from the figure that after the oil reverse drive, there is a large amount of kerosene in the core, but the oil reverse drive does not drive out all the retained fracturing fluids in the slice, and some of it remains in the core. For tight reservoirs, as more and more water is retained in the reservoir rocks due to fracturing fluid retention, plus reasonable shut-in time, more oil will be produced due to imbibition displacement, and the production will increase significantly.

3.2. Influence of Fracturing Fluid Loss on Permeability. Through the curve analysis in Figures 8 and 9, it can be concluded that with the increase of porosity, the amount of retained fracturing fluids in the core will decrease, while

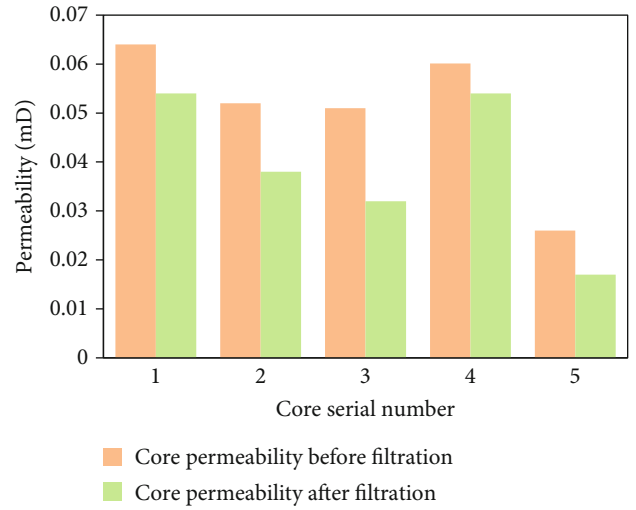

Figure 10: The permeability change before and after core fracturing fluid retention.

when the permeability decreases, the amount of retained fracturing fluids in the core will increase. Among them, compared with porosity, the correlation between core permeability and retained water is good. The results show that, in the actual production process, there will be more fracturing fluid retention in the tight core and more fracturing fluid retention in the reservoir; then, the retained fracturing fluids in the reservoir will replace the oil in the micro pores under the appropriate well shut-in time, thus producing more oil. This is different from the traditional production wells that require rapid flow-back. For conventional oil well exploitation, the reservoir permeability is relatively high, and the retained fracturing fluids that can be retained in the formation itself is less, so the displacement effect is not significant. Therefore, the rapid flow-back method is required to effectively avoid reservoir damage. However, in the tight reservoir, it has low permeability, and the fracturing fluids is mostly slippery water system, so the reservoir itself is less damaged by the fracturing fluids. At the same time, the fracturing fluids flow-back rate is very low. In addition, the retained fracturing fluids will displace the oil that is difficult to flow in the tight reservoir, thus increasing the production of oil wells. Therefore, the most important thing in tight reservoirs is to determine the reasonable shut in time and give full play to its advantages of imbibition displacement, rather than blindly pursuing a high flow-back rate.

Figure 10 shows the permeability change before and after core fracturing fluid retention. It can be seen from the figure that the permeability after fracturing fluid retention has decreased to a certain extent compared with the permeability before core fracturing fluid retention. This is due to the high content of clay minerals in low-permeability reservoirs. In the process of saturated oil, some oil will be adsorbed by clay minerals. With their gradual accumulation and occupation, the originally small pore space will be further reduced, which greatly reduces the porosity and permeability, increases the thickness of the boundary layer, and aggravates the influence of the boundary layer on seepage. The pore space of clay

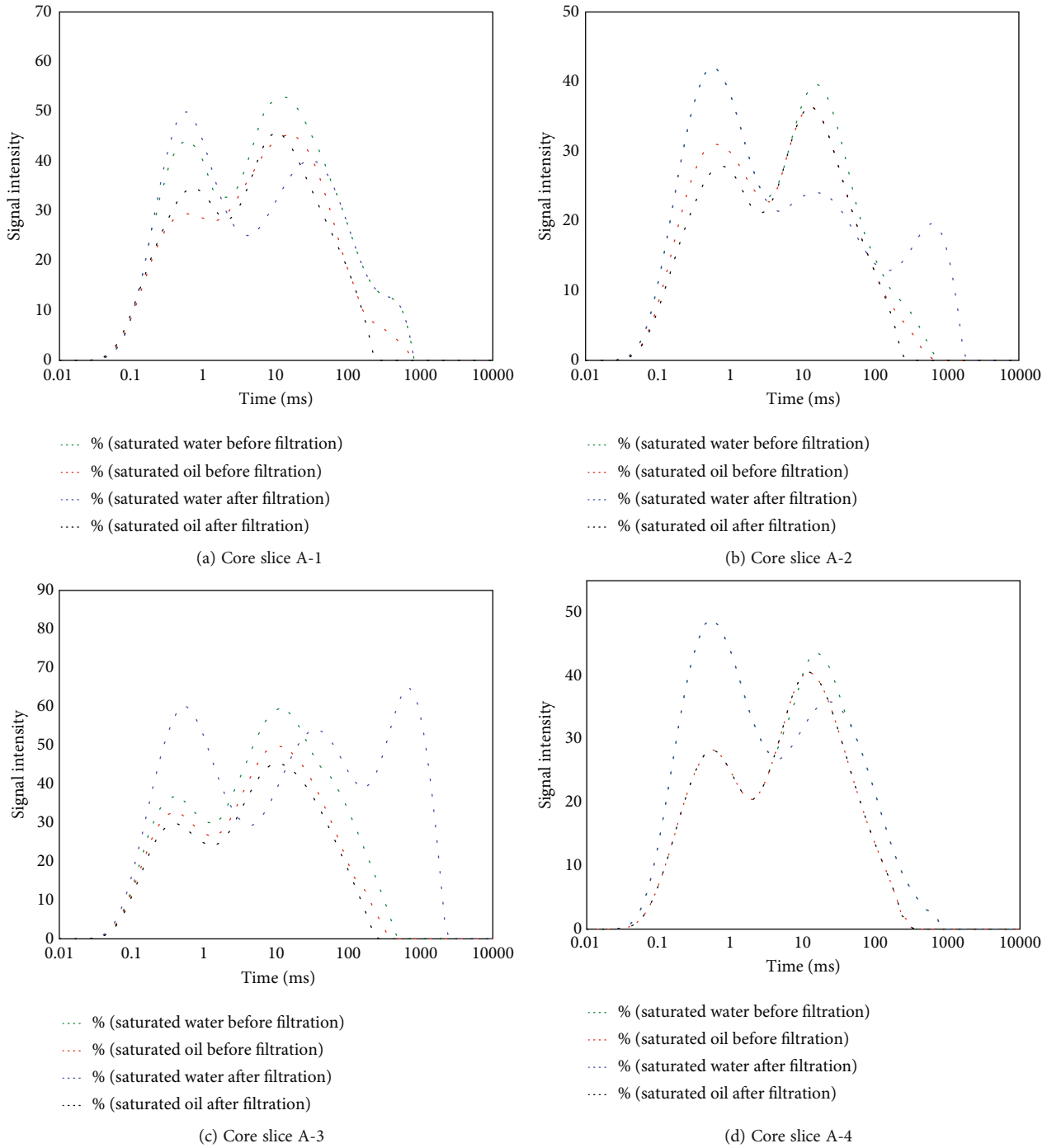

(a) Core slice A-1

(b) Core slice A-2

(c) Core slice A-3

(d) Core slice A-4

Figure 11: Continued.

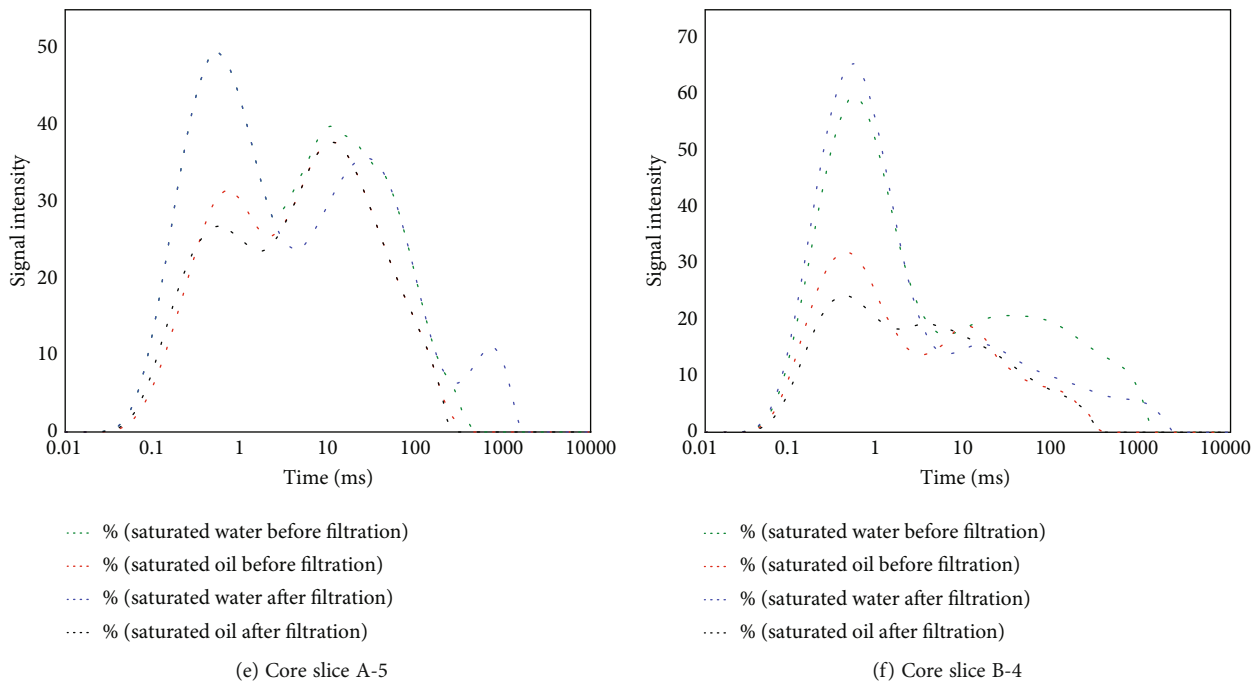

Figure 11: NMR spectra of different core slices.

Table 3: Mixed wettability test results of different core slices.

No.	Before fracturing fluid retention				After fracturing fluid retention			
	Hydrophilicity coefficient	Lipophilic coefficient	Mixed wettability	Wettability	Hydrophilicity coefficient	Lipophilic coefficient	Mixed wettability	Wettability
A-1	0.577	0.422	0.154	Weak hydrophilicity	0.572	0.427	0.145	Weak hydrophilicity
A-2	0.574	0.425	0.149	Weak hydrophilicity	0.608	0.391	0.217	Weak hydrophilicity
A-3	0.527	0.472	0.055	Neutral	0.649	0.350	0.299	Weak hydrophilicity
A-4	0.641	0.358	0.283	Weak hydrophilicity	0.655	0.344	0.311	Hydrophilicity
A-5	0.636	0.363	0.273	Weak hydrophilicity	0.639	0.360	0.278	Weak hydrophilicity
B-4	0.634	0.365	0.268	Weak hydrophilicity	0.715	0.284	0.430	Hydrophilicity

minerals, such as illite, with a large content in the reservoir in this area, is often filled by them, resulting in the narrowing or even disappearance of the pore throat, increasing the heterogeneity of the pore throat, and increasing the uncertainty and complexity of the fracturing fluid retention process. Therefore, there are a large number of clay minerals in the tight reservoir that affect the structure of the pore throat and lead to a significant increase in its microheterogeneity, making the pore throat thinner and poor connectivity, reducing the seepage channel and greatly reducing its permeability.

3.3. Influence of Retained Fracturing Fluids on Wettability. The wettability is evaluated according to the evaluation standard of wettability. When the mixed wettability index is greater than 0, it indicates that the hydrophilic part in the core is more than the lipophilic part, which generally shows the hydrophilic characteristics. The higher value will cause stronger hydrophilicity of the core. When the mixed wettability index is less than 0, it indicates that the lipophilic part of the core is more than the hydrophilic part, showing the characteristics of lipophilicity in general. The lower value indicates the stronger lipophilicity of the core. The measured T2 spectrum is shown in Figure 11.

The results of the mixed wettability of core slices are shown in Table 3. From the table, it shows that the average hydrophilic coefficient of core slices used in this experiment is 0.598. The average lipophilic coefficient is 0.402, and the average mixed wettability index is 0.196. The wettability is generally weak and hydrophilic. The average hydrophilicity coefficient, oil affinity coefficient, and mixed wettability

index of the core slice measured again after the retention of the fracturing fluids are 0.640, 0.360, and 0.280, respectively. It can be seen that the mixed wettability index of the core slice before and after the retention of the fracturing fluids increases slightly, but it is still in the range of weak hydrophilicity. Therefore, the retained fracturing fluids during the fracturing process have little impact on the reservoir wettability, and there is no wettability inversion.

4. Conclusions

Under laboratory experimental conditions, this paper studies the influence of retained fracturing fluids on reservoir physical properties by using core thin section and nuclear magnetic resonance technology, clarifies the distribution of retained fracturing fluids in the core, and reveals the influence rule of retained fracturing fluids on tight reservoir permeability and wettability.

(1) The retention of fracturing fluids and oil in micropores is studied using nuclear magnetic resonance technology and a stereoscopic microscope. The main retention space of retained fracturing fluids in tight reservoirs is a microporous interval. The residual oil after displacement by retained fracturing fluids mainly exists in the core in the form of dots or patches

(2) There will be more retained fracturing fluids in the tight core. The smaller permeability and porosity of the core will cause the more retained fracturing fluids. The permeability of different cores after fracturing fluid retention has decreased to varying degrees compared with that before fracturing fluid retention. In tight reservoirs, clay minerals will expand or migrate when encountering retained fracturing fluids, which will occupy the pore space, reducing the porosity and poor permeability

(3) Using the method of evaluating the overall mixed wettability of tight cores, combining the indoor core physical simulation with nuclear magnetic resonance technology, the wettability of core slices before and after the test is tested, and the retained fracturing fluids has no significant impact on the reservoir wettability

Data Availability

Data is available by contacting the corresponding author.

Conflicts of Interest

The authors declare that they have no conflicts of interest.

Acknowledgments

This study was supported by the National Natural Science Foundation of China (grant nos. 51874242 and 51934005).

References

[1] S. Longde, Z. Caineng, J. Ailin et al., "Development characteristics and orientation of tight oil and gas in China," *Petroleum Exploration and Development*, vol. 46, no. 6, pp. 1015–1026, 2019.

[2] B. Liu, Y. Yang, J. Li, Y. Chi, J. Li, and X. Fu, "Stress sensitivity of tight reservoirs and its effect on oil saturation: a case study of lower cretaceous tight clastic reservoirs in the Hailar Basin, Northeast China," *Journal of Petroleum Science and Engineering*, vol. 184, article 106484, 2020.

[3] Y. Xie, X. Liu, J. Wang, N. Wu, C. Hu, and Y. Wang, "Characteristics and main controlling factors of tight oil reservoirs in Chang 7 member of Yanchang formation in Ordos Basin, North Shaanxi," *Marine Geology & Quaternary Geology*, vol. 42, no. 3, pp. 149–159, 2022.

[4] D. Zhang, L. Zhang, T. A. Huiying, and Z. H. Yulong, "Fully coupled fluid-solid productivity numerical simulation of multistage fractured horizontal well in tight oil reservoirs," *Petroleum Exploration and Development*, vol. 49, no. 2, pp. 338–347, 2022.

[5] J. Wang, H. Q. Liu, G. B. Qian, and Y. C. Peng, "Mechanisms and capacity of high-pressure soaking after hydraulic fracturing in tight/shale oil reservoirs," *Petroleum Science*, vol. 18, no. 2, pp. 546–564, 2021.

[6] B. B. Williams, "Fluid loss from hydraulically induced fractures," *Journal of Petroleum Technology*, vol. 22, no. 7, pp. 882–888, 1970.

[7] C. H. Yew, M. J. Ma, and A. D. Hill, "A study of fluid leakoff in hydraulic fracture propagation," in *International Oil and Gas Conference and Exhibition in China*, Beijing, China, 2000.

[8] J. L. Rodgerson, "Impact of natural fractures in hydraulic fracturing of tight Gas Sands," in *SPE Permian Basin Oil and Gas Recovery Conference*, Midland, Texas, 2000.

[9] H. D. Outmans, "Mechanics of static and dynamic filtration in the borehole," *Society of Petroleum Engineers Journal*, vol. 3, no. 3, pp. 236–244, 1963.

[10] P. S. Vinod, M. L. Flindt, R. J. Card, and J. P. Mitchell, "Dynamic fluid-loss studies in low-permeability formations with natural fractures," in *SPE production operations Symposium*, Oklahoma City, Oklahoma, 1997.

[11] S. A. Mathias and M. Van Reeuwijk, "Hydraulic fracture propagation with 3-D leakoff," *Transport in Porous Media*, vol. 80, no. 3, pp. 499–518, 2009.

[12] B. Hou, Z. Cui, J.-H. Ding, F.-S. Zhang, L. Zhuang, and D. Elsworth, "Perforation optimization of layer-penetration fracturing for commingling gas production in coal measure strata," *Petroleum Science*, vol. 19, no. 4, pp. 1718–1734, 2022.

[13] Q. A. Da, C. J. Yao, X. Zhang, X. P. Wang, X. H. Qu, and G. L. Lei, "Investigation on microscopic invasion characteristics and retention mechanism of fracturing fluid in fractured porous media," *Petroleum Science*, vol. 19, no. 4, pp. 1745–1756, 2022.

[14] J. Lu, B. Hao, C. Li, W. Wang, Q. Wang, and W. Yang, "Permeability prediction of tight sandstone reservoirs based on flow unit classification," *Petroleum Science Bulletin*, vol. 3, pp. 369–379, 2021.

[15] S. J. Pirson, E. M. Boatman, and R. L. Nettle, "Prediction of relative permeability characteristics of intergranular reservoir rocks from electrical resistivity measurements," *Journal of Petroleum Technology*, vol. 16, no. 5, pp. 564–570, 1964.

[16] K. O. Akande, T. O. Owolabi, S. O. Olatunji, and A. AbdulRaheem, "A hybrid particle swarm optimization and support vector regression model for modelling permeability prediction of hydrocarbon reservoir," *Journal of Petroleum Science and Engineering*, vol. 150, no. 2, pp. 43–53, 2017.

[17] W. R. Purcell, "Capillary pressures - their measurement using mercury and the calculation of permeability therefrom," *Journal of Petroleum Technology*, vol. 1, no. 2, pp. 39–48, 1949.

[18] J. H. M. Thomeer, "Introduction of a pore geometrical factor defined by the capillary pressure curve," *Journal of Petroleum Technology*, vol. 12, no. 3, pp. 73–77, 1960.

[19] J. H. M. Thomeer, "Air permeability as a function of three pore-network parameters," *Journal of Petroleum Technology*, vol. 35, no. 4, pp. 809–814, 1983.

[20] S. J. Kolodzie, "Analysis of pore throat size and use of the Waxman-Smits equation to determine OOIP in Spindle field, Calorado," in *SPE Annual Technical Conference and Exhibition*, Dallas, Texas, 1980.

[21] M. R. Rezaee, A. Saeedi, and B. Clennell, "Tight gas sands permeability estimation from mercury injection capillary pressure and nuclear magnetic resonance data," *Journal of Petroleum Science and Engineering*, vol. 12, pp. 92–99, 2012.

[22] K. B. Min, J. Rutqvist, C. F. Tsang, and L. Jing, "Stress-dependent permeability of fractured rock masses: a numerical study," *International Journal of Rock Mechanics and Mining Sciences*, vol. 41, no. 7, pp. 1191–1210, 2004.

[23] B. Larsen, I. Grunnaleite, and A. Gudmundsson, "How fracture systems affect permeability development in shallow-water carbonate rocks: an example from the Gargano Peninsula, Italy," *Journal of Structural Geology*, vol. 32, no. 9, pp. 1212–1230, 2010.

[24] Z. Meng, S. L. Yang, Y. Cui et al., "Enhancement of the imbibition recovery by surfactants in tight oil reservoirs," *Petroleum Science*, vol. 15, no. 4, pp. 783–793, 2018.

[25] J. Wang, L. Z. Xiao, G. Z. Liao et al., "NMR characterizing mixed wettability under intermediate-wet condition," *Magnetic Resonance Imaging*, vol. 56, pp. 156–160, 2019.

[26] Y. Zhang, H. Ge, Y. Shen, L. Jia, and J. Wang, "Evaluating the potential for oil recovery by imbibition and time-delay effect in tight reservoirs during shut-in," *Journal of Petroleum Science and Engineering*, vol. 184, article 106557, 2020.

[27] J. J. Howard, "Quantitative estimates of porous media wettability from proton NMR measurements," *Magnetic Resonance Imaging*, vol. 16, no. 5-6, pp. 529–533, 1998.

[28] C. Straley, C. E. Morriss, W. E. Kenyon, and J. J. Howard, "NMR in partially saturated sandstones: laboratory insights into free fluid index, and comparison with borehole logs," *The Log Analyst*, vol. 36, pp. 40–56, 1995.

[29] M. Fleury and F. Deflandre, "Quantitative evaluation of porous media wettability using NMR relaxometry," *Magnetic Resonance Imaging*, vol. 21, no. 3-4, pp. 385–387, 2003.

[30] H. Guan, D. Brougham, K. S. Sorbie, and K. J. Packer, "Wettability effects in a sandstone reservoir and outcrop cores from NMR relaxation time distributions," *Journal of Petroleum Science and Engineering*, vol. 34, no. 1-4, pp. 35–54, 2002.

[31] S. H. Al-Mahrooqi, C. A. Grattoni, A. H. Muggeridge, R. W. Zimmerman, and X. D. Jing, "Pore-scale modelling of NMR relaxation for the characterization of wettability," *Journal of Petroleum Science and Engineering*, vol. 52, no. 1-4, pp. 172–186, 2006.

[32] E. B. Johannesen, H. Riskedal, L. Tipura, J. J. Howard, and A. Graue, "Wettability characterization by NMR T2 measurements in Edwards limestone rock," in *International Symposium of the Society of Core Analysts*, pp. 10–13, Calgary, Canada, 2007.

[33] J. Chen, G. J. Hirasaki, and M. Flaum, "NMR wettability indices: effect of OBM on wettability and NMR responses," *Journal of Petroleum Science and Engineering*, vol. 52, no. 1-4, pp. 161–171, 2006.

[34] C. C. Minh, S. Crary, P. M. Singer et al., "Determination of wettability from magnetic resonance relaxation and diffusion measurements on fresh-state cores," in *SPWLA 56th Annual Logging Symposium*, Long Beach, California, USA, 2015.

[35] A. Rabiei, M. Sharifinik, A. Niazi, A. Hashemi, and S. Ayatollahi, "Core flooding tests to investigate the effects of IFT reduction and wettability alteration on oil recovery during MEOR process in an Iranian oil reservoir," *Applied Microbiology and Biotechnology*, vol. 97, no. 13, pp. 5979–5991, 2013.

[36] D. H. Pratten and R. G. Craig, "Wettability of a hydrophilic addition silicone impression material," *Journal of Prosthetic Dentistry*, vol. 61, no. 2, pp. 197–202, 1989.

[37] C. Gachot, M. Hans, R. Catrin, U. Schmid, and F. Mücklich, "Tuned wettability of material surfaces for tribological applications in miniaturized systems by laser interference metallurgy," in *Smart Sensors, Actuators, and MEMS IV (Vol. 7362, pp. 242-250)*, Dresden, Germany, 2009.

[38] Y. Zhang, Y. Zou, Y. Zhang et al., "Experimental study on characteristics and mechanisms of matrix pressure transmission near the fracture surface during post-fracturing shut-in in tight oil reservoirs," *Journal of Petroleum Science and Engineering*, vol. 219, article 111133, 2022.

[39] G. Chunyuan, Q. I. Rongsheng, D. I. Qinfeng, F. Jiang, and C. H. Huijuan, "Simulation and visualization experiment of manganese ion diffusion and damage to gel in a porous media-gel system," *Petroleum Exploration and Development*, vol. 46, no. 2, pp. 354–360, 2019.

[40] M. Meng, L. Li, B. Yuan et al., "Influence of overburden pressure on imbibition behavior in tight sandstones using nuclear magnetic resonance technique," *Journal of Energy Resources Technology*, vol. 145, no. 7, article 073302, 2023.

[41] Y. L. Su, J. L. Xu, W. D. Wang, H. Wang, and S. Y. Zhan, "Relative permeability estimation of oil–water two-phase flow in shale reservoir," *Petroleum Science*, vol. 19, no. 3, pp. 1153–1164, 2022.

Hindawi
Geofluids
Volume 2023, Article ID 7897165, 11 pages
https://doi.org/10.1155/2023/7897165

Research Article

Experimental Study for the Effects of Different Factors on the Sand-Carrying Capacity of Slickwater

Huan Peng,[1,2] **Wenzhe Li**,[1,2] **Juncheng Liu**,[3] **Junliang Peng**,[1,2] **Huifen Han**,[1,2] **Jiayi Liu**,[4] **Dan Liu**,[1] **and Zhifan Yang**[1,2]

[1]*Engineering Technology Research Institute of Southwest Oil & Gas Field Company, PetroChina, Chengdu 610017, China*
[2]*Key Laboratory of Shale Gas Evaluation and Exploitation of Sichuan Province, Chengdu 610017, China*
[3]*Development Division of Southwest Oil & Gas Field Company, PetroChina, Chengdu 610051, China*
[4]*Shunan Gas Field of Southwest Oil & Gas Field Company, PetroChina, Luzhou 646000, China*

Correspondence should be addressed to Huan Peng; 282600120@qq.com

Received 6 December 2022; Revised 2 January 2023; Accepted 22 March 2023; Published 4 April 2023

Academic Editor: Daoyi Zhu

With the continuous exploration and development of unconventional oil and gas reservoirs, volume fracturing technology becomes one of the necessary measures for developing shale gas and tight sandstone gas reservoirs effectively. Volume fracturing technology usually uses slickwater and drag-reducing agent as the core of the fracturing system. The composition of the fracturing system is the main factor determining its performance. Polyacrylamide has many amide groups in its main chain, high activity, and controllable performance, often in solid powder and liquid emulsion states. Furthermore, polyacrylamide which is the water-soluble drag-reducing agent is most widely used in applying current shale gas slickwater fracturing operations. Due to the low viscosity and poor sand-carrying capacity of slickwater, proppant easily settles at the bottom of hydraulic fractures. This phenomenon influences the stimulation effect of volume fracturing. Therefore, the law of sand carrying and placement of proppant in hydraulic fractures in volume fracturing plays an essential role in determining the success of the stimulation effect of volume fracturing. Through the visualization device of proppant transport in the fracture, the settlement of proppant in the fracture was studied experimentally. And through experimental equipment, the effects of different operation pumping rates, liquid viscosity, proppant type, and proppant pumping schedule on the stimulation effect were studied. The experimental results can provide strong support for volume fracturing into well material optimization and operation parameter optimization for unconventional oil and gas reservoirs.

1. Introduction

With the continuous exploration and development of unconventional oil and gas reservoirs, hydraulic fracturing has become one of the necessary measures for increasing the production of low-permeability and extra-low-permeability reservoirs [1–3]. Reservoir stimulation of shale and tight sandstone by the combination of volume fracturing, segmented multicluster perforation, and high pumping rate and the large amount of fracturing fluid usage, slickwater, and temporary plugging agent techniques can provide communication between natural fractures and rock stratigraphy. Furthermore, by communicating between natural fractures and rock laminae, the hydraulic fractures are interwoven with multilevel secondary fractures to form a fracture network system [4–7]. The fracture network system can "break up" the effective reservoir where seepage can take place, maximize the contact area between the fractures and the reservoir, and increase the volume of the reservoir stimulation as much as possible. It enables the shortest percolation distance of oil and gas from the matrix in any direction to the fracture; dramatically improves the overall permeability of the reservoir; realizes a comprehensive transformation of the reservoir in the three-dimensional direction of length, width, and height; increases the percolation area and inflow capacity; and improves the initial production and final recovery [8–13].

Due to the low viscosity of slickwater, the capacity for sand carrying is poor, so it is necessary to improve the sand-carrying capacity of fracturing fluid by increasing the injection rate of slickwater [14, 15]. However, the friction resistance in the pipeline is increased by this measure. As such, the drag-reducing agent becomes the core of slickwater fracturing technology and plays a decisive role. Furthermore, the drag-reducing agent has become a research hotspot all around the world. Polyacrylamide is a synthetic polymer obtained by the copolymerization of acrylamide and other monomers, including cationic, anionic, nonionic, and amphoteric polyacrylamide. Polyacrylamide that can be dissolved in water in any proportion is a long-chain macromolecule, and it has good thermal stability and drag reduction performance. Polyacrylamide has a large number of amide groups in the main chain, with high activity and controllable performance, usually in the state of solid powder and liquid. And polyacrylamide is the most widely used water-soluble dampening agent in shale gas slickwater fracturing operation [16, 17].

In shale gas and tight sandstone fracturing, due to the low viscosity of slickwater, poor sand-carrying capacity, and fast settling rate of proppant, the exorbitant concentration of proppant during operation is likely to cause sand plugging [18, 19]. However, the low concentration of proppant will reduce the concentration of sand laid in the fractures and the effects of fracturing stimulation. Due to the development of microfractures in the reservoir, fracturing will induce a large amount of slickwater filtration loss. And the slickwater filtration loss exacerbates the difficulty of proppant transport. As the height of the sand dike increases, the slickwater overflow area in the fracture decreases, and the liquid flow rate gradually increases. When the fluid flow rate increases to the extent that the proppant can reach dynamic suspension, the height of the sand dike is the equilibrium height. There is no proppant filling at the top of the fracture above the equilibrium height at this time. The proppant often settles at the bottom of the fracture, while there is no proppant placement in the upper part of the fracture and away from the wellbore end. This situation reduces the fracture inflow capacity and effects of fracturing stimulation. Therefore, studying the law of proppant carrying, transport, settling, and placement pattern in the fracture is crucial. The placement of proppant in the hydraulic fracturing process is essential to the outcome of the fracturing operation. The prediction of proppant placement is also the key to the design and evaluation of hydraulic fracturing [20–23].

In recent years, the studies of the sand-carrying capacity of slickwater were mainly based on laboratory experiments and numerical simulations. In the experimental studies, Liu et al. [24], Wu and Sharma [25], Hu et al. [26], and other researchers carry out experimental studies under different conditions of fracture width, pumping rate, and particle size. Through the experimental studies, they obtain the accumulation process of sand settlement and the various patterns of equilibrium height. Furthermore, they derived the empirical equations of equilibrium height, equilibrium velocity, and other characteristic parameters. In the field of numerical simulation, Olaleye et al. [27], Akhshik and Rajabi [28], Suri et al. [29], and Guo et al. [30] used the CFD method to simulate the transport process of proppant settlement in different fractures. Zhang et al. [31] use a coupled CFD-DEM method to establish a solid-liquid mixing model between parallel plates to analyze the microscopic sand-carrying mechanism of fracturing fluid in hydraulic fracturing. In general, the researches on the law of the carry and transport of proppant during the fracturing process were mainly theoretical. Field operation is often based on experience or software simulations, and there are few systematic experimental studies [32, 33]. The rheology of the liquid, flow rate, concentration, and density of proppant affect the sand-carrying capacity of slickwater, which is not conducive to grasping the laws of proppant placement, roll-up, and sand settlement distribution during sand addition [34–37]. Thus, it is necessary to carry out systematic research and analysis to compare and select fracturing fluid and proppant parameters and optimize fracturing operation parameters to ensure the formation of effective proppant placement and improve fracture conductivity [38–40].

In this paper, the proppant transport visualization device is used to observe the flow status of the sand-carrying fluid in the fracture, the scouring and carrying performance of the fluid on the proppant, and the proppant transport and settlement status through the transparent glass. By changing parameters such as pumping rate, fluid viscosity, proppant type, and pumping schedule, experimental research on the law of sand carrying and settlement in proppant-supported fracture was carried out. And the effects of different factors in volume fracturing on the sand-carrying capacity of slickwater and the settlement pattern of proppant were studied by quantitative analysis of experimental results. The research results can provide strong technical support for the preferential selection of volume fracturing entry materials and optimization of operation parameters for unconventional oil and gas reservoirs.

2. Experimental Methods

2.1. Experimental Materials. The slickwater system is commonly used in volume fracturing, and the slickwater system is formed by compounding additives such as drag-reducing agent, clay stabilizers, and drainage aids. The basic formula of our configured slickwater system is water + 0.1 ~ 0.5% emulsion drag − reducing agent + 0.25% clay stabilizer + 0.1% drainage aid. Slickwater with different viscosity values can be obtained by varying the amount of drag-reducing agent. We adopted the evaluation method for the performance of slickwater fracturing fluid which refers to the requirements and technical indexes in industry-related standards of China such as SY/T 5107-2016 (Performance Evaluation Method of Water-based Fracturing Fluid), SY/T 5613-2000 (Test Method of Physical and Chemical Properties of Mud Shale), NB/T 14003.1-2015 (Slickwater Fracturing Fluid Part 1: Performance Index and Evaluation Method), and other industry-related standards and technical indexes for the evaluation method of slickwater fracturing fluid performance. According to the standard, we conducted indoor testing to evaluate the performance of the slickwater fracturing fluid

Table 1: Performance parameters of slickwater.

Term	Apparent viscosity (mPa·s)	pH	Surface tension (mN/m)	Interfacial tension (mN/m)
Parameters	1~100	6.5~7.0	24~26	0.8~1.8
Term	CST ratio	Linear expansion rate (%)	Residue content (mg/L)	Resistance reduction rate (%)
Parameters	0.7~1.2	1.1~2.5	20~50	50~74

Table 2: 40/70 mesh ceramsite proppant performance parameters.

Term	Average diameter (μm)	Sphericity	Acid solubility (%)	Turbidity (FTU)
Parameters	320~370	0.9	3.1~6.4	38~79
Term	Bulk density (g/cm^3)	Apparent density (g/cm^3)	9% crushing grade of domestic proppant (K)	
Parameters	1.5~1.8	2.5~2.9	12.5~15.0	

system. The evaluation indexes mainly include apparent performance, resistance reduction rate, surface tension, and linear expansion rate, and the performance parameters of slickwater are shown in Table 1.

We selected the ceramsite proppant that is commonly used in current volume fracturing. According to the SY/T 5108-2014 (Test Method of Proppant Performance for Hydraulic Fracturing and Gravel Filling Operations), the basic properties of proppant such as density, roundness, turbidity, acid solubility, and anticrushing rate are evaluated. The performance parameters of the support agent are shown in Table 2. Figure 1 shows the 40/70 mesh ceramsite proppant appearance.

2.2. Experimental Device. Figures 2 and 3 show the technological process of the experimental device for visualization of the flow state in proppant-supported fracture. The experimental device comprises six parts: fluid supply and pumping system, sand mixing system, powder delivery system, visible fracture system, fluid recovery system, data acquisition, and control system. Among these six parts, the width and height of the visible fracture system are 6 mm and 0.6 m. The length of the visible fracture system is available in three modes, 2 m, 4 m, and 6 m. The maximum pumping rate of the power delivery system is 200 L/min, which can complete the engineering simulation experiment of the settlement pattern in the volume fracturing proppant-supported fracture.

The device can simulate a segment of artificial fracture in volume fracturing, which can be injected into the visual fracture system at different velocities by a powered delivery system. The flow of fracturing fluid or sand-carrying fluid in the fracture and the proppant transport and placement can be clearly observed through the transparent Plexiglas of the visual fracture system.

2.3. Experimental Steps. The experimental schedule for the visualization of the flow state in the proppant-supported fracture is as follows:

Step 1: connect the experimental apparatus, ensure the sealing of the experimental device, start the data acquisition and control system of the experimental device, and clear the data to zero.

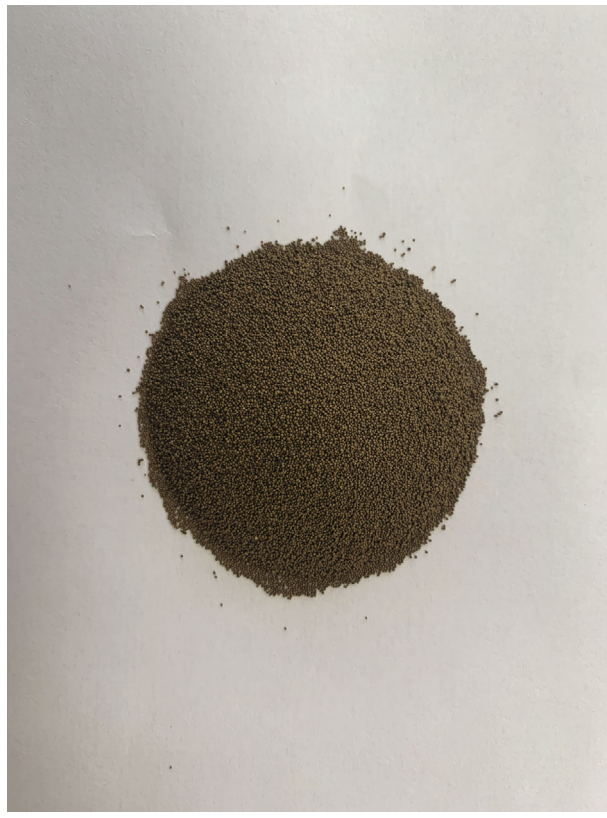

Figure 1: 40/70 mesh ceramsite proppant appearance.

Step 2: close the outlet of the sand mixing tank of the sand mixing system, inject the amount of fracturing fluid required for the experiment, calculate and measure the number of additives required for the slickwater, open the agitator of the sand mixing tank, and add the required additives.

Step 3: open the outlet of the sand mixing tank, start the screw pump of the fluid supply and pumping system, inject fracturing fluid into the simulated fracture, and wait for the fracturing fluid to fill the whole fracture.

Step 4: calculate and measure the number of proppant particles required for the experiment, add it to the powder delivery system, adjust the transfer velocity of the sand

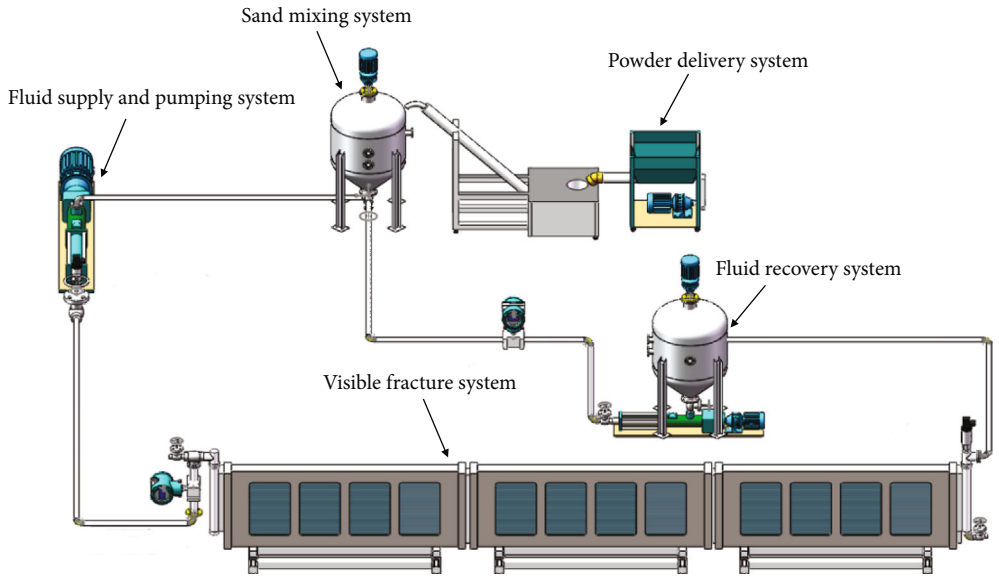

Figure 2: The technological process of an experimental device for visualization of flow state in proppant-supported fracture.

Figure 3: Experimental device for visualization of proppant flow state in proppant-supported fracture.

transfer device to ensure that it is mixed with the fracturing fluid in the sand mixing tank to reach dynamic equilibrium, adjust it to the sand concentration required for the experiment, turn on the screw pump and data acquisition system, and start the experiment.

Step 5: from the time the proppant starts to enter the fracture timing, the experimental process is filmed using the high-resolution video camera in the data acquisition and control system to record the proppant in proppant-supported fracture settlement patterns throughout the experimental process under different experimental conditions.

Step 6: after the sand mixing liquid is pumped, sand mixing system, fluid supply and pumping system, and powder delivery system are shut down, the data acquisition system is closed, and the experiment is finished.

Step 7: the visible fracture system is flushed with clean water. In the fluid recovery system, the proppant and fracturing fluid are separated and the proppant particles are collected and dried for reuse, while the fracturing fluid is uniformly recycled for disposal.

2.4. Experimental Scheme. The experiments follow the Reynolds similarity principle by converting the volume fracturing field operation pumping rate to the flow rate of the intrafracture fluid in the visible fracture system in the experimental setup, calculated as follows:

$$v_e = \frac{v_f}{h_f \times w_f \times 2} \times (h_e \times w_e). \quad (1)$$

The parameters in Equation (1) are shown in Table 3.

At present, the characteristics of the volume fracturing process are the high pumping rate, large amount of fracturing fluid and proppant usage, small particle size, and low sand ratio. The main technical parameters are as follows: the horizontal section is 1000~1500 m long, divided into 15~20 segments, each segment is divided into 4~6 clusters of perforation, the spacing of the cluster of perforation is 20~30 m, the pumping rate is 10 m^3/min or more, the average sand ratio concentration is 100~240 kg/m^3, the fracturing fluid volume is 1500~2000 m^3 per segment, and the proppant volume is 100~150 t per segment. The fracturing fluid system combines slickwater and linear rubber, and the proppant volume is mainly 40/70 mesh.

In order to study the effects of pumping rate, fluid viscosity, proppant density, and proppant pumping schedule on the law of proppant settlement, we combined the current field volume fracturing operation parameters to design experiment cases, such as in Table 4.

3. The Characteristics of Sand Carrying by Slickwater

Figure 4 indicates the transport process of proppant in fracture, where Ho is defined as the fracture height and He is defined as the equilibrium height of the sand dike. After the proppant particles enter the fracture, the sand dike will

Table 3: Meaning of the symbols in Equation (1).

Symbol	V_e	V_f	h_f
Meaning	Pumping rate of indoor experiment (m^3/min)	Field pumping rate (m^3/min)	The height of the hydraulic fracture (m)
Symbol	W_f	H_e	W_e
Meaning	The width of the hydraulic fracture (mm)	The height of fracture in visible fracture system (m)	The width of the fracture in the visible fracture system (mm)

Table 4: Experimental scheme of proppant settlement and transport in proppant-supported fracture of volumetric fracturing proppant.

No.	Pumping rate (L/min)	Liquid viscosity (mPa·s)	Proppant bulk density (g/cm^3)	Proppant concentration (kg/m^3)	Proppant pumping schedule
1	40	3	1.50	150	Sand uniformly throughout the whole process
2	60	3	1.50	150	Sand uniformly throughout the whole process
3	80	3	1.50	150	Sand uniformly throughout the whole process
4	80	30	1.50	150	Sand uniformly throughout the whole process
5	80	100	1.50	150	Sand uniformly throughout the whole process
6	60	3	1.65	150	Sand uniformly throughout the whole process
7	60	3	1.80	150	Sand uniformly throughout the whole process
8	60	3	1.50	80~220	Slope sand throughout the whole process
9	60	3	1.50	80~220	Slug slope sand throughout the whole process

gradually accumulate with time. Until the height of the sand dike no longer increases, it is the equilibrium height. The t_1~t_8 are the sand dike forms under the nth minute.

It was found that in the first to fourth minutes of the initial stage of sand carrying by slickwater, the sand-carrying liquid flows out from the borehole at high velocity. The proppant settles to the bottom of the fracture by gravity to form a sand dike. With the sand-carrying liquid's continuous pumping, the length and height of the sand dike gradually increase. Finally, the sand dike gradually reaches the equilibrium height near the fracture inlet. After reaching equilibrium height, proppant particles rolled up and sunk in the fracture reach equilibrium, and the height of the sand dike remains unchanged. This stage is sand dike formation.

In the intermediate stage of sand carrying by slickwater at 5-6 minutes, the gap between the top of the sand dike and the top of the fracture will reduce to a minimum when the sand dike near the wellbore reaches the equilibrium height. Because the number of proppant particles settling at this location equals the number of proppant being carried away, settlement occurs after the proppant is transported to the sand dike to reach the equilibrium height. Due to the injected sand-carrying liquid, the dike of sand that has reached equilibrium height flows over it and settles before flowing to a location where it has not yet reached equilibrium height. Thus, the final equilibrium height will keep moving towards the flow direction towards the front of the flow. This stage is sand dike balance.

At 7-8 minutes of the final stage of sand carrying by slickwater, the front section of the sand dike reaches the equilibrium height. In this stage, the sand dike grows only in the length direction with the injection of sand-carrying liquid, and the height always maintains the equilibrium height, and the sand dike always grows forward with the equilibrium height. This stage is sand dike advancement.

In summary, the whole process of sand carrying by slickwater and proppant settlement in fractures can be divided into three stages: sand dike formation, sand dike balance, and sand dike advancement.

4. Experimental Results and Analysis

4.1. The Effect of Pumping Rate on the Law of Sand Carrying by Slickwater. Volume fracturing with large fluid volumes and a high pumping rate is usually used to stimulate the shale gas and tight gas reservoirs. Under the condition of the same total proppant dose and concentration of proppant, we studied the effect of pumping rate on the law of sand carrying by slickwater. The pumping rates in the experimental cases are 40 L/min, 60 L/min, and 80 L/min. These three cases correspond to field operation pumping rates of 6 m^3/min, 8 m^3/min, and 12 m^3/min, respectively. The height of the sand dike with different pumping rates at different times is shown in Figure 5, and the final shape of the sand dike is shown in Figure 6.

From Figures 5 and 6, we can see that different pumping rates have a significant effect on the shape of the sand dike under the condition. As the pumping rate increases, the horizontal transport velocity of particles increases, and the equilibrium height of the sand dike decreases. The equilibrium height of the sand dike is 0.44 m when the pumping rate is 40 L/min, 0.42 m when it is 60 L/min, and 0.39 m when it is 80 L/min. The pumping rate increases cause the sand dike

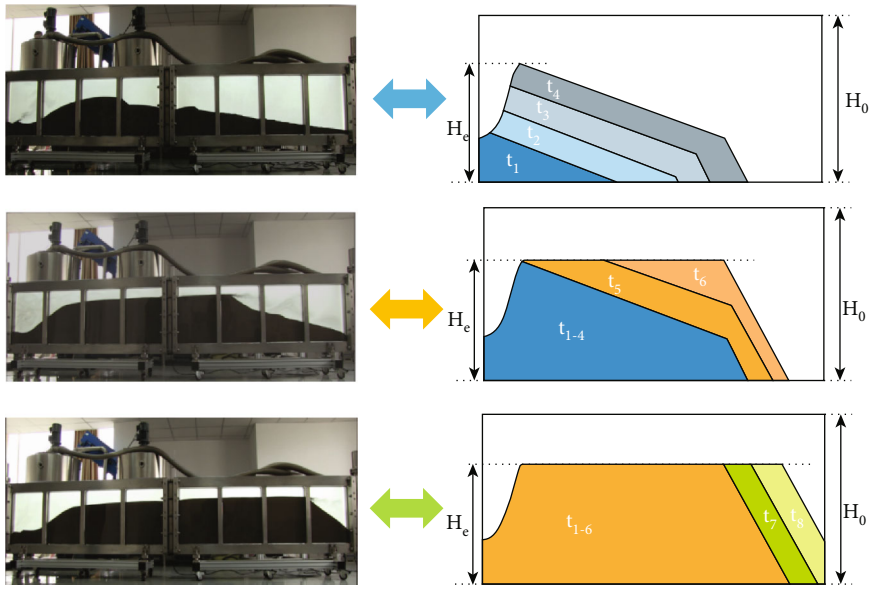

Figure 4: The process of sand carrying by slickwater and proppant transport.

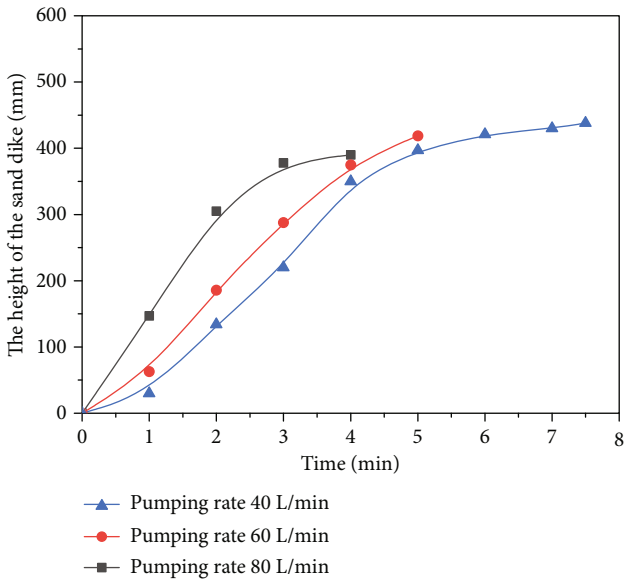

Figure 5: The height of the sand dike in sand carrying by slickwater with different pumping rates.

to become gentle and tend to transport deep into the fracture. Thus, the proppant cannot be delivered deep into the fracture when the pumping rate is low. During the process of field operation, to form a long and effective proppant-supported fracture, the operation pumping rate should be increased as much as the conditions allow. However, we cannot increase the pumping rate without limitation because the pumping rate increase causes equilibrium height reduction and low concentration of proppant near the fracture inlet. This is not conducive to forming proppant-supported fracture with high conductivity at the fracture inlet, as shown in Figure 6.

4.2. The Effect of Liquid Viscosity on the Law of Sand Carrying by Slickwater. The advantages of low viscous slickwater are low reservoir damage, large stimulation reservoir volume, and low cost, but the disadvantage is limited sand-carrying capacity. The high-viscosity fracturing fluid has a positive sand-carrying capacity, but it is harmful to the reservoir and too expensive. To improve the sand-carrying capacity of slickwater and reduce reservoir damage and the cost of volume fracturing, we need to establish a variable-viscosity slickwater liquid system. Thus, we investigated the effect of liquid viscosity on the law of proppant settlement in slickwater. The results of this part of the study can guide the optimal formation of a variable-viscosity slickwater liquid system to meet the requirements of increasing the volume of reservoir stimulation and sand-carrying capacity of slickwater. The cases used in the experiments were all performed under the same total proppant and pumping rate conditions. The pumping rate in the experiment is 80 L/min. Figure 7 reveals the height of the sand dike at different times with different liquid viscosities, and Figure 8 shows the final shape of the sand dike. It can be seen in Figure 7 that the viscosity is 3 mPa·s, 30 mPa·s, and 100 mPa·s, respectively, when the liquid is low-viscosity slickwater, medium-viscosity slickwater, and high-viscosity slickwater. The time to reach equilibrium height for sand dikes with low viscous slickwater and medium viscous slickwater was 4.0 min and 3.0 min, respectively. The equilibrium heights of sand dikes are 0.41 m and 0.32 m for low viscous slickwater (viscosity of 3 mPa·s) and medium viscous slickwater (30 mPa·s) conditions, respectively, as shown in Figure 8. Due to the high viscous slickwater with high sand-carrying capacity, the proppant advances uniformly forward in the fracture, and the settlement rate is slow. The sand dike advances uniformly in the fracture.

In summary, the effect of slickwater viscosity on the law of sand-carrying capacity by slickwater is consistent with the

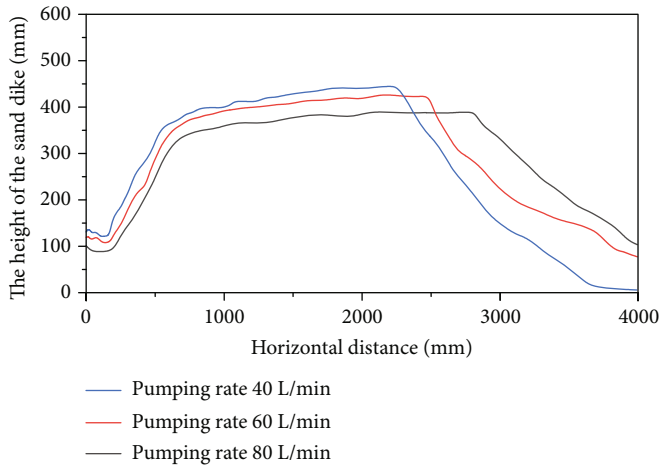

Figure 6: The shape of the sand dike formed by proppant sedimentation in sand carrying by slickwater with different pumping rates.

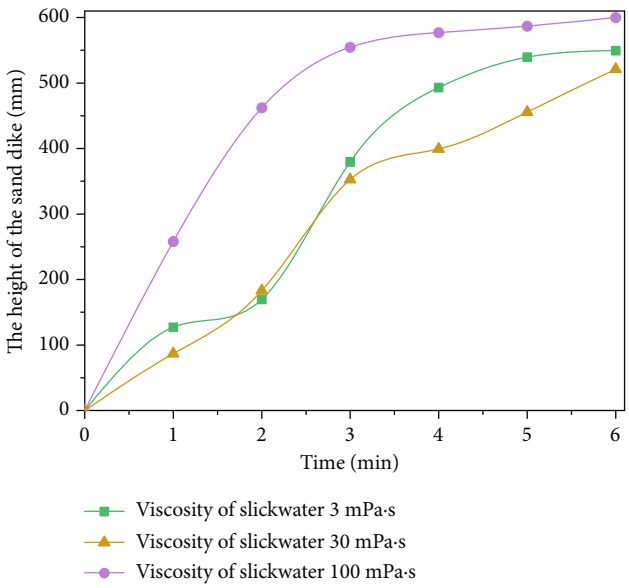

Figure 7: The height of the sand dike in sand carrying by slickwater with different liquid viscosities.

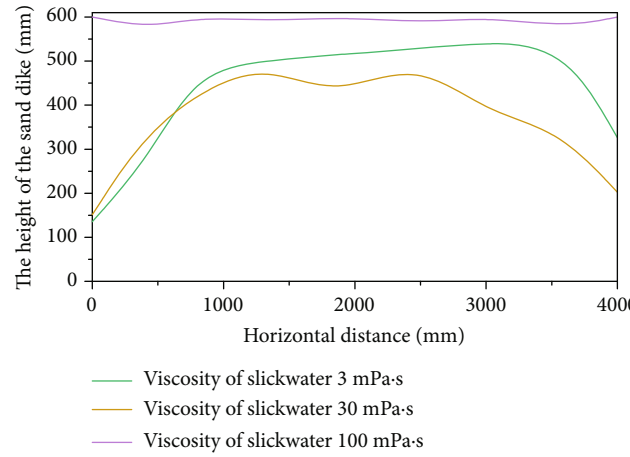

Figure 8: The shape of the sand dike formed by proppant sedimentation in sand carrying by slickwater with different liquid viscosities.

trend of pumping rate on the law of sand carrying by slickwater. Furthermore, the effect of liquid viscosity on the sand-carrying capacity of slickwater is more significant than the pumping rate. Therefore, during field operation in order to form the proppant-supported fracture with a longer length and higher conductivity, slickwater with high viscosity should be selected as far as possible under the condition of satisfying the reservoir damage so that the proppant can be transported to the fracture tips.

4.3. The Effect of Proppant Bulk Density on the Law of Sand Carrying by Slickwater. Proppant is used in volume fracturing to establish proppant-supported fracture with high conductivity, thus ensuring the reservoir stimulation effect. Under the condition of the same total proppant dose and pumping rate, the study on the effect of different proppant types on the settlement pattern of proppant was carried out, which adopts the pumping rate was 60 L/min. Figure 9 indicates the height of the sand dike at different times with different proppant densities, and the final shape of the sand dike is shown in Figure 10. It was found that different proppant density impacts the shape of the sand dike at the same total proppant dose and pumping rate. As the proppant density decreases, the horizontal transport velocity of particles decreases, and the equilibrium height of the sand dike decreases. When the proppant density is 1.80 g/cm^3, the sand dike equilibrium height is 450 mm. When the proppant density is 1.65 g/cm^3, the sand dike equilibrium height is 0.43 m. When the proppant density is 1.50 g/cm^3, the sand dike equilibrium height is 0.42 m. Sand dike thus becomes smoother, and similar to the increased pumping rate, there is a tendency for proppant to be transported deeper into the fractures. Overall, the influence of proppant density on proppant settling law is opposite to the influence of

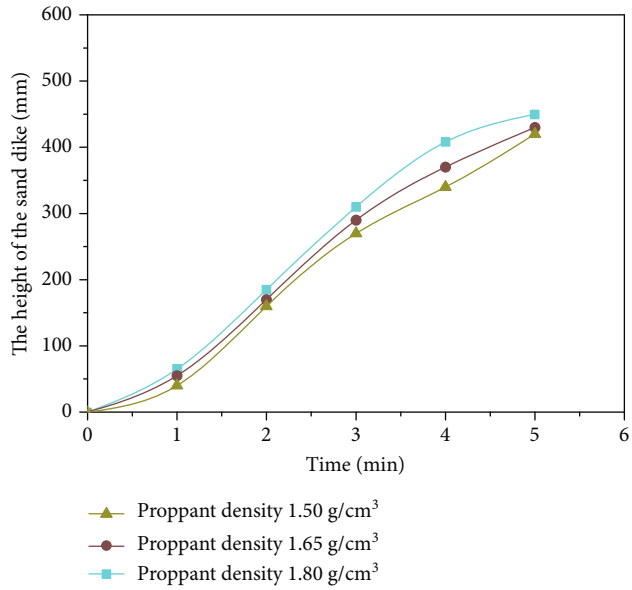

Figure 9: The height of the sand dike in sand carrying by slickwater with different proppant densities.

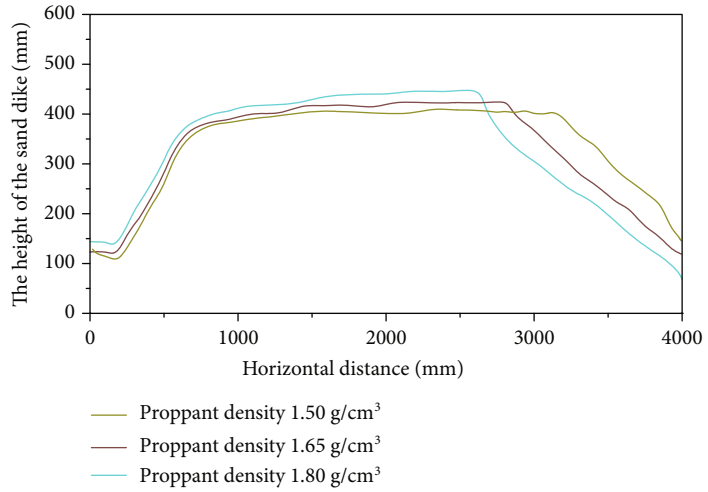

Figure 10: The shape of the sand dike formed by proppant sedimentation in sand carrying by slickwater with different proppant densities.

pumping rate on proppant settling law, and the influence of proppant density on proppant settling law is smaller than the influence of pumping rate on proppant settling law. During the field construction, to form the proppant-supported fracture with a longer length and higher conductivity, low-density proppant should be used as much as possible under the condition that the compressive strength of the proppant is satisfied, which can make the proppant delivered to the depth of the fractures.

4.4. The Effect of Proppant Pumping Schedule on the Law of Proppant Settlement. In order to meet the needs of the reservoir stimulation, slope sand and slug slope sand pumps are selected to inject the proppant schedule [13, 14]. Thus, we researched the effect of the proppant pumping schedule on the law of proppant settlement with the condition of the same total proppant dose and pumping rate, and the pumping rate in the experiment was 60 L/min. Figure 11 shows the height of the sand dike at different times with different proppant pumping schedules, and the final shape of the sand dike is shown in Figure 12. Different proppant pumping schedules significantly affect sand dike morphology for the same total proppant dose and pumping rate. The height of the sand dike grows more rapidly in uniform sand addition throughout the whole process. When slope sand addition is used, the initial increase in the height of the sand dike is slow due to the low proppant concentration at the beginning of pumping. With slope sand addition, the proppant concentration becomes more significant at the later stage of pumping, resulting in an increase in proppant concentration at the

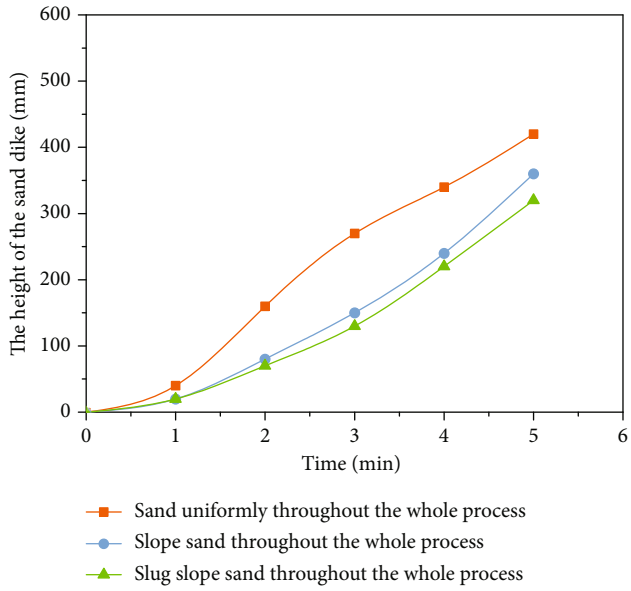

Figure 11: The height of the sand dike in sand carrying by slickwater with different proppant pumping schedules.

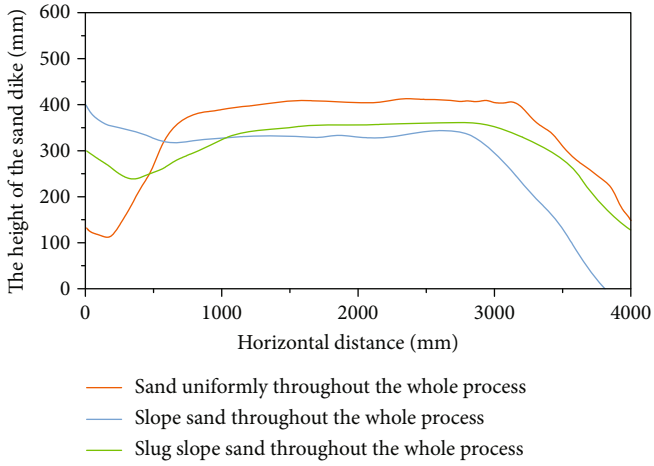

Figure 12: The shape of the sand dike formed by proppant sedimentation in sand carrying by slickwater with different proppant pumping schedules.

fracture inlet, which can form a proppant-supported fracture with high conductivity. Compared to slope sand addition, when slug slope sand addition is used, the proppant-free liquid has a more substantial scouring effect on the sand dike. It can transport the proppant to the depth of the fracture, thus forming a better proppant-supported fracture both near the fracture inlet and deeper in the fracture.

5. Conclusion

(1) With the pumping rate increases, the horizontal transport velocity of particles increases and the equilibrium height of the sand dike decreases, among which the equilibrium height of the sand dike is 0.44 m, 0.42 m, and 0.39 m for the pumping rate of 40 L/min, 60 L/min, and 80 L/min, respectively. The pumping rate increases cause the sand dike to become gentle and tend to transport deep into the fracture. Thus, the pumping rate should be increased as much as possible during the field operation process of volume fracturing

(2) When the viscosity is low viscous slickwater (3 mPa·s) and medium viscous slickwater (30 mPa·s), the equilibrium height of the sand dike produced is 0.41 m and 0.32 mm, respectively. Due to the high viscous slickwater (viscosity 100 mPa·s) with great sand-carrying capacity, the proppant advances evenly forward in the fracture, the settlement rate is slow, and the sand dike advances evenly in the fracture. During the field operation process, to form the proppant-supported fracture with a longer length and higher conductivity, slickwater with high viscosity should be selected as much as possible under the acceptable condition of reservoir damage, which can make the proppant deliver to the depth of fractures

(3) As the density of the proppant decreases, the equilibrium height of the sand dike decreases, where the equilibrium height of the sand dike is 0.45 m, 0.43 m, and 0.42 m when the density of the proppant is 1.80 g/cm^3, 1.65 g/cm^3, and 1.50 g/cm^3, and the sand dike thus becomes more gentle. During the field operation process, to form the proppant-supported fracture with a longer length and higher conductivity, low-density proppant should be used as much as possible under the condition that the compressive strength of the proppant is satisfied, which can enable the proppant to be delivered deeper into the fractures

(4) In different proppant pumping schedules, the sand dike height grows more rapidly when the whole process of uniform sand addition is used. Because the low concentration of proppant is selected at the beginning of the pumping schedule, the initial increase of the height of the sand dike is slower when slope sand addition is used. Furthermore, the concentration of proppant at the fracture inlet and the proppant-supported fracture with high conductivity during later in the pumping schedule. Compared with the slope sand addition, when slug slope sand addition is used, the proppant-free liquid has a stronger flushing effect on the sand dike. Thus, the proppant is transported to the depth of the fracture. And the proppant-supported fracture with higher conductivity both near the fracture inlet and deep in the fracture is formed. It can help achieve better oil and gas production

Data Availability

The experiment data used to support the findings of this study are included within the article.

Conflicts of Interest

The authors declare that they have no conflicts of interest.

Acknowledgments

This study was financially supported by the Scientific Research and Technology Development Project of Southwest Oil and Gas Field Company, PetroChina (No. 20210302-05 and No. 20210305-22).

References

[1] A. S. Ramlan, R. M. Zin, N. F. A. Bakar, and N. H. Othman, "Recent progress on proppant laboratory testing method: characterisation, conductivity, transportation, and erosivity," *Journal of Petroleum Science and Engineering*, vol. 205, article 108871, 2021.

[2] J. M. Estrada and R. Bhamidimarri, "A review of the issues and treatment options for wastewater from shale gas extraction by hydraulic fracturing," *Fuel*, vol. 182, pp. 292–303, 2016.

[3] C. Jia, M. Zheng, and Y. Zhang, "Unconventional hydrocarbon resources in China and the prospect of exploration and development," *Petroleum Exploration and Development*, vol. 39, no. 2, pp. 139–146, 2012.

[4] M. Paterniti, D. Kundert, M. Ramurthy, and D. Craig, "Production review of current stimulation techniques in the Jonah field," in *Paper Presented at the SPE Hydraulic Fracturing Technology Conference*, pp. 1–11, The Woodlands, TX, USA, February 2013.

[5] Y. Peng, J. Zhao, K. Sepehrnoori, Y. Li, and Z. Li, "The influences of stress level, temperature, and water content on the fitted fractional orders of geomaterials," *Mechanics of Time-Dependent Materials*, vol. 24, no. 2, pp. 221–232, 2020.

[6] Y. Peng, Y. Li, and J. Zhao, "A novel approach to simulate the stress and displacement fields induced by hydraulic fractures under arbitrarily distributed inner pressure," *Journal of Natural Gas Science & Engineering*, vol. 35, pp. 1079–1087, 2016.

[7] Y. Jinzhou Zhao, Y. L. Peng, and W. Xiao, "Analytical model for simulating and analyzing the influence of interfacial slip on fracture height propagation in shale gas layers," *Environmental Earth Sciences*, vol. 73, no. 10, pp. 5867–5875, 2015.

[8] Y. Peng, K. Jinzhou Zhao, Z. L. Sepehrnoori, and X. Feng, "Study of delayed creep fracture initiation and propagation based on semi- analytical fractional model," *Applied Mathematical Modelling*, vol. 72, pp. 700–715, 2019.

[9] Y. Jinzhou Zhao, Y. L. Peng, and Z. Tian, "Applicable conditions and analytical corrections of plane strain assumption in the simulation of hydraulic fracturing," *Petroleum Exploration and Development*, vol. 44, no. 3, pp. 454–461, 2017.

[10] Y. Peng, J. Zhao, K. Sepehrnoori, and Z. Li, "Fractional model for simulating the viscoelastic behavior of artificial fracture in shale gas," *Engineering Fracture Mechanics*, vol. 228, article 106892, 2020.

[11] H. Peng, F. Yu, J. Peng et al., "Research and application of a proppant transport experimental device for complex fractures in the unconventional reservoir," *Geofluids*, vol. 2022, Article ID 8356470, 10 pages, 2022.

[12] Y. Huan Peng, J. P. Fan, X. Gao, X. Gou, and Y. Yin, "Experimental evaluation and application of new size proppant for unconventional reservoir fracturing," *Fresenius Environmental Bulletin*, vol. 31, no. 3, pp. 2898–2907, 2022.

[13] H. Peng, J. Yang, J. Peng, H. Han, X. Gou, and Y. Jia, "Source analysis and countermeasure research of sand production after hydraulic fracturing in tight sandstone gas reservoir," *Lithosphere*, vol. 2022, no. Special 12, article 8342062, 2022.

[14] H. Bai, F. Zhou, M. Zhang et al., "Optimization and friction reduction study of a new type of viscoelastic slickwater system," *Journal of Molecular Liquids*, vol. 344, article 117876, 2021.

[15] N. K. Korlepara, K. Gore, and S. D. Kulkarni, "Understanding effect of fluid salinity on polymeric drag reduction in turbulent flows of slickwater fluids," *Journal of Petroleum Science and Engineering*, vol. 216, article 110747, 2022.

[16] S. Shi, J. Sun, K. Lv et al., "Comparative studies on thickeners as hydraulic fracturing fluids: suspension versus powder," *Gels*, vol. 8, no. 11, p. 722, 2022.

[17] A. V. Shibaev, A. A. Osiptsov, and O. E. Philippova, "Novel trends in the development of surfactant-based hydraulic fracturing fluids: a review," *Gels*, vol. 7, no. 4, p. 258, 2021.

[18] H. Peng, L. Zhou, J. Yang et al., "Influence of supercritical CO_2 on the formation sensitivity of tight sandstone," *Frontiers in Energy Research*, vol. 10, article 922941, 2022.

[19] H. Peng, J. Yang, J. Peng et al., "Experimental investigation of the mechanism of supercritical CO_2 interaction with tight sandstone," *Frontiers in Energy Research*, vol. 10, article 984144, 2022.

[20] S. Tong and K. K. Mohanty, "Proppant transport study in fractures with intersections," *Fuel*, vol. 181, no. 1, pp. 463–477, 2016.

[21] M. E. Fernández, M. Sánchez, and L. A. Pugnaloni, "Proppant transport in a scaled vertical planar fracture: vorticity and dune placement," *Journal of Petroleum Science and Engineering*, vol. 173, pp. 1382–1389, 2019.

[22] K. Shrivastava and M. M. Sharma, "Proppant transport in complex fracture networks," in *SPE Hydraulic Fracturing Technology Conference and Exhibition*, pp. 1–10, The Woodlands, TX, USA, 2018.

[23] R. Sahai, J. L. Miskimins, and K. E. Olson, "Laboratory results of proppant transport in complex fracture systems," in *SPE Hydraulic Fracturing Technology Conference*, pp. 1–26, The Woodlands, TX, USA, 2014.

[24] X. Liu, X. Zhang, Q. Wen, S. Zhang, Q. Liu, and J. Zhao, "Experimental research on the proppant transport behavior in nonviscous and viscous fluids," *Energy & Fuels*, vol. 34, no. 12, pp. 15969–15982, 2020.

[25] C.-H. Wu and M. M. Sharma, "Effect of perforation geometry and orientation on proppant placement in perforation clusters in a horizontal well," in *SPE Hydraulic Fracturing Technology Conference*, pp. 1–23, The Woodlands, TX, USA, 2016.

[26] H. Xiaodong, W. Kan, G. Li, J. Tang, and Z. Shen, "Effect of proppant addition schedule on the proppant distribution in a straight fracture for Slickwater treatment," *Journal of Petroleum Science and Engineering*, vol. 167, pp. 110–119, 2018.

[27] A. K. Olaleye, O. Shardt, G. Walker, H. E. A. Van den Akker, and H. E. A. Van den Akker, "Pneumatic conveying of cohesive dairy powder: experiments and CFD-DEM simulations," *Powder Technology*, vol. 357, pp. 193–213, 2019.

[28] S. Akhshik and M. Rajabi, "Simulation of proppant transport at intersection of hydraulic fracture and natural fracture of wellbores using CFD-DEM," *Particuology*, vol. 63, pp. 112–124, 2022.

[29] Y. Suri, S. Z. Islam, and M. Hossain, "Proppant transport in dynamically propagating hydraulic fractures using CFD-XFEM approach," *International Journal of Rock Mechanics and Mining Sciences*, vol. 131, article 104356, 2020.

[30] T. K. Guo, Z. Luo, J. Zhou et al., "Numerical simulation on proppant migration and placement within the rough and complex fractures," *Petroleum Science*, vol. 19, no. 5, pp. 2268–2283, 2022.

[31] G. Zhang, M. Li, and M. Gutierrez, "Simulation of the transport and placement of multi-sized proppant in hydraulic fractures using a coupled CFD-DEM approach," *Advanced Powder Technology*, vol. 28, no. 7, pp. 1704–1718, 2017.

[32] M. Baldini, C. M. Carlevaro, L. A. Pugnaloni, and M. Sánchez, "Numerical simulation of proppant transport in a planar fracture. A study of perforation placement and injection strategy," *International Journal of Multiphase Flow*, vol. 109, pp. 207–218, 2018.

[33] S. E. Gorucu, V. Shrivastava, and L. X. Nghiem, "Numerical simulation of proppant transport in hydraulically fractured reservoirs," in *SPE Reservoir Simulation Conference*, pp. 1–15, 2021.

[34] R. Sahai and R. G. Moghanloo, "Proppant transport in complex fracture networks - a review," *Journal of Petroleum Science and Engineering*, vol. 182, article 106199, 2019.

[35] X. Zhang, L. Yang, D. Weng, Z. Wang, and R. G. Jeffrey, "Numerical study on proppant transport in hydraulic fractures using a pseudo-3D model for multilayered Reservoirs," *SPE Journal*, vol. 27, no. 1, pp. 77–92, 2022.

[36] A. Isah, M. Hiba, K. Al-Azani, M. S. Aljawad, and M. Mahmoud, "A comprehensive review of proppant transport in fractured reservoirs: experimental, numerical, and field aspects," *Journal of Natural Gas Science and Engineering*, vol. 88, article 103832, 2021.

[37] A. Bello, J. Ozoani, and D. Kuriashov, "Proppant transport in hydraulic fractures by creating a capillary suspension," *Journal of Petroleum Science and Engineering*, vol. 208, article 109508, 2022.

[38] S. Yatin, S. Z. Islam, and M. Hossain, "Effect of fracture roughness on the hydrodynamics of proppant transport in hydraulic fractures," *Journal of Natural Gas Science and Engineering*, vol. 80, article 103401, 2020.

[39] E. Rivas and R. Gracie, "A monolithic coupled hydraulic fracture model with proppant transport," *Computer Methods in Applied Mechanics and Engineering*, vol. 372, article 113361, 2020.

[40] A. M. Skopintsev, E. V. Dontsov, P. V. Kovtunenko, A. N. Baykin, and S. V. Golovin, "The coupling of an enhanced pseudo-3D model for hydraulic fracturing with a proppant transport model," *Engineering Fracture Mechanics*, vol. 236, article 107177, 2020.

Hindawi
Geofluids
Volume 2023, Article ID 4981874, 13 pages
https://doi.org/10.1155/2023/4981874

Research Article

Study on Damage Mechanism of Waterflooding Development in Weizhou 11-4N Low-Permeability Oilfield

Yi Zhang,[1] **Pengyu Zhu**,[1] **Feng Wei**,[2] **Guoqing Xue**,[3] **Mingguang Tang**,[2] **Congdi Zhang**,[4] **and Rui Wang**[1]

[1]*Engineering Research Center of the Ministry of Education for the Development and Treatment of Low and Ultra-Low Permeability in the West of Xi'an Shiyou University, Shanxi, Xi'an 710065, China*
[2]*Zhanjiang Branch of CNOOC (China) Co., Ltd, Guangdong, Zhanjiang 524057, China*
[3]*Hainan Branch of CNOOC (China) Co., Ltd, Hainan, Haikou 570312, China*
[4]*Yakela Gas Exploitation Plant, Sinopet Northwest China Oilfield Company, Xinjiang Kuche 842017, China*

Correspondence should be addressed to Yi Zhang; zhyfly@163.com

Received 6 September 2022; Revised 11 October 2022; Accepted 15 October 2022; Published 16 February 2023

Academic Editor: Daoyi Zhu

Weizhou 11-4N oilfield is a medium-low-porosity and low-permeability reservoir. The oilfield was initially developed by edge and bottom water energy and then transferred to water injection development. Affected by poor physical properties and heterogeneity of the reservoir, the oilfield appeared in the process of water injection development. When the water injection pressure increases, the water injection volume continues to decrease, and it is difficult to meet the injection requirements. On the basis of the analysis of reservoir heterogeneity, void structure, and clay minerals of reservoir, the water injection compatibility experiment, damage evaluation experiment, and nuclear magnetic resonance-velocity sensitivity experiments were carried out to clarify the damage in the process of oilfield water flooding development. Experiments show that the main causes of damage in Weizhou 11-4N oilfield water flooding development process are water quality incompatibility and strong velocity-sensitive damage. The determination of water type shows that the injected water and formation water are $MgCl_2$ water type and $NaHCO_3$ water type, respectively, under the classification of Surin water type, resulting in the formation of scale with calcium carbonate as the main component in the reservoir. Incompatibility of water quality is an important cause of reservoir damage and scaling. In the reservoir-sensitive flow experiment, the experimental core showed strong velocity sensitivity, the average velocity sensitivity damage rate was 466.31%, and the average critical velocity was 2.98 m/d. Nuclear magnetic resonance experiments show that the core has a significant decrease in average pore size after water flooding. The main damage range is the tiny throat of 0-2 μm. In this paper, the main damage interval of velocity-sensitive damage in the Weizhou 11-4N area and the change trend of void structure after velocity-sensitive experiment are clarified by nuclear magnetic resonance and velocity sensitivity experiments. The main cause of block reservoir damage provides the basis for the oilfield to take targeted measures and provides a guarantee for the efficient development of the subsequent oilfield.

1. Introduction

Weizhou 11-4N oilfield is located in the Beibu Gulf of the South China Sea about 100 km away from Beihai city and about 50 km away from Weizhou island. It was first discovered in 1986 according to two-dimensional seismic interpretation. The Paleogene of Weizhou 11-4N Oilfield mainly develops the Weizhou formation, Liushagang formation, and Changliu formation. The main oil groups are L_1V, L_1III, and L_1I oil groups [1–5]. In the early stage of development, depletion development was adopted, then gradually adopt water injection development. In order to restore the formation energy and maintain a high oil production rate, in the process of water injection development, high injection volume water injection was used at the initial stage. After water injection development for a period of time, the water injection pressure continued to increase, and the water injection volume decreased to varying degrees.

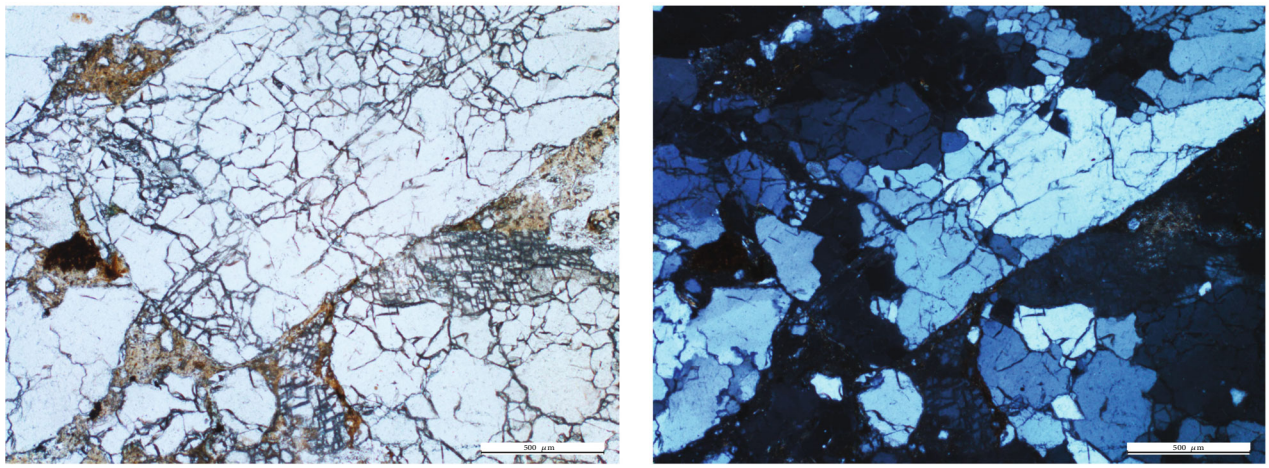

Figure 1: Thin section of core casting of L_1 section in Weizhou 11-4N oilfield.

The water injection volume of some water injection wells has been reduced by 70%, and the oil production volume of the corresponding oil production wells has also been greatly reduced compared with the initial stage of water injection, which seriously restricts the efficient development of the oil field. It is particularly important to clarify the damage to the reservoir caused by the speed sensitivity in water flooding development and to improve the development benefit for the subsequent depressurization and injection.

In 2008, Bedrikovetsky et al. [6] established a depth filter loss model through theoretical analysis and experimental research, obtained the particle concentration values at multiple points through the indoor long core segment test, and then used the least square method to obtain the core impedance model. The damage evaluation parameters of the system can be obtained. In 2009, Xijin and Feng [7] analyzed the hydration mechanism of biotite and analyzed the influence on water injection according to the hydration process. In the same year, Lijun and Yili [8] analyzed the influence of capillary self-absorption on reservoir sensitivity evaluation by using capillary self-absorption experiments on the basis of reviewing the capillary self-absorption mechanism. In 2014, on the basis of study on compatibility of water quality, Yutian et al. [9] used electron microscopy to analyze the damage characteristics of scaling after water injection, sewage reinjection, etc. and believed that water quality incompatibility and high oil content in the sewage were the main damage factor in the process of water injection.

In 2018, Ramez et al. [10] showed that low-salinity water flooding can effectively improve water flooding effect and reduce reservoir damage, and the optimal salinity is related to the physical properties of the reservoir. In the same year, Jianjun et al. [11] conducted an indoor evaluation of waterflooding and scaling, combined with the analysis of core minerals in the early and late stages of development, and clarified the reservoir scaling mechanism, and made it clear that scaling, velocity sensitivity, and water sensitivity are the main damage types. In 2019, Lei et al. [12] applied the global mobility theory to evaluate the results of water flooding experiments with different salinities and established an oil-water two-phase flow oil well productivity equation considering low-velocity non-Darcy flow and reservoir stress sensitivity. The effects of reservoir properties and oil-water two-phase seepage capacity on reservoir productivity were quantitatively evaluated. In the same year, Moghadasi et al. [13] showed that nanosilica has obvious effect of inhibiting calcium sulfate scaling in formation water with high salinity at appropriate temperature, but the effect is not obvious at low salinity.

In 2020, based on the study of reservoir geological characteristics, Dongyu et al. [14] used laboratory experiments to determine the reservoir damage mechanism during water injection and believed that strong water sensitivity and high water injection intensity were the main damages in the development process. In the same year, Wang and Zhou [15] used electron microscope scanning technology to study the difference in water plugging damage between uncracked cores and cracked cores and evaluated the improvement effect of the new nanoemulsion on microclogging and liquid flow capacity. In 2021, Zhu et al. [16] reviewed the application research progress of NMR technology in the role of polymer gels, showing that it has broad application prospects in evaluating the performance of gel and monitoring the improvement effect of gel. In 2022, Negahdari et al. [17] proposed a technology to optimize the injection water composition of low-salinity water flooding using numerical simulation. The study showed that the optimal injection water composition in the same formation is not unique. Yi et al. [18] used a neural network to predict and analyze reservoir damage based on laboratory experimental results. The above papers have done a lot of work in improving water injection effect, reducing reservoir damage and reservoir scaling mechanism, and inhibiting reservoir scaling. However, none of the above papers paid attention to the microscopic damage mechanism of the reservoir. In this paper, based on the analysis of Weizhou 11-4N reservoir characteristics, the microscopic damage mechanism of the core and the main size range of pore throat damage will be studied. The potential damage mechanism of the reservoir was analyzed by scanning electron microscope, X-ray diffraction, and other experimental results, and the damage mechanism of the reservoir was clarified by the indoor flooding

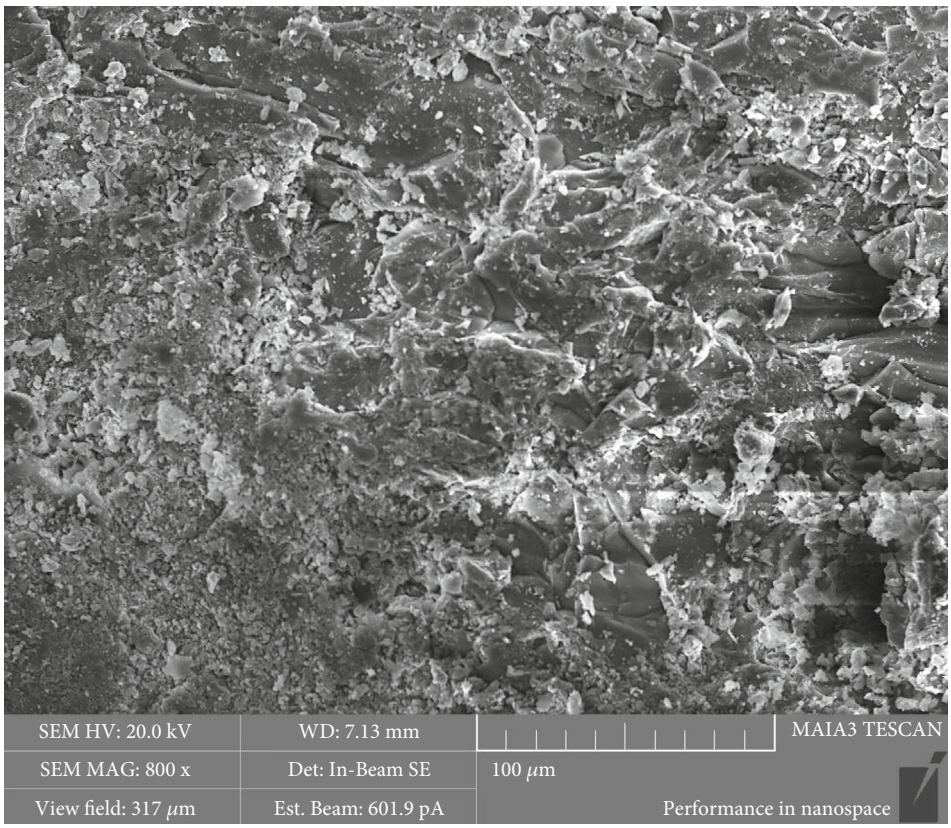

(a) A5 core Panorama

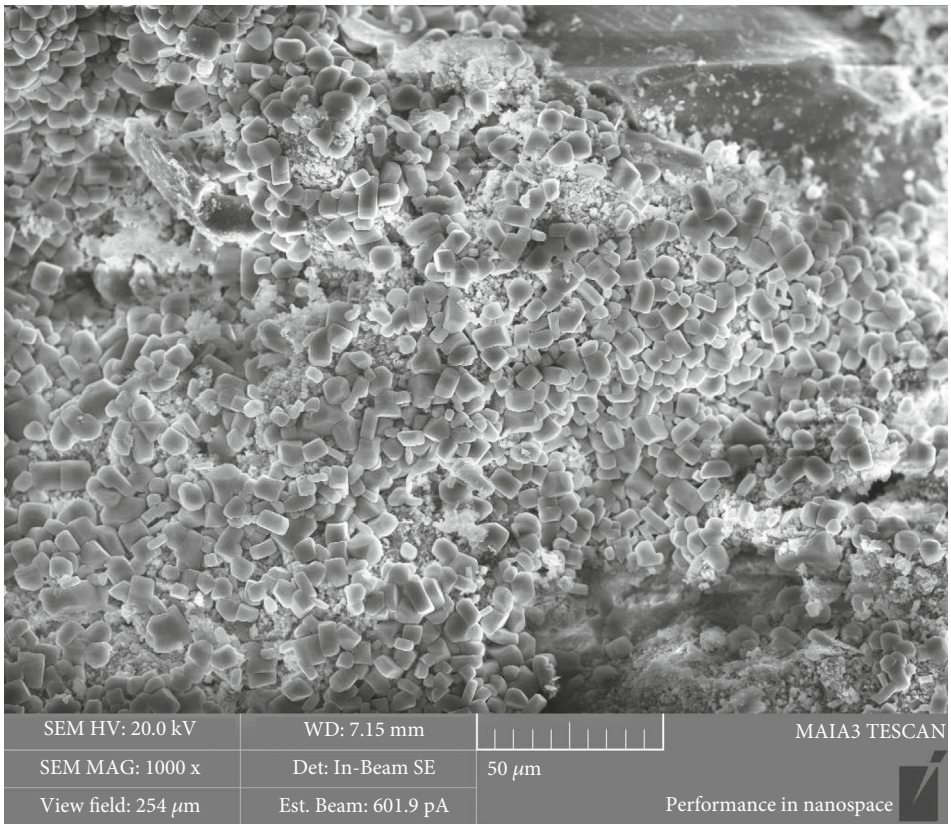

(b) A5 Core magnification (1000 times)

Figure 2: Continued.

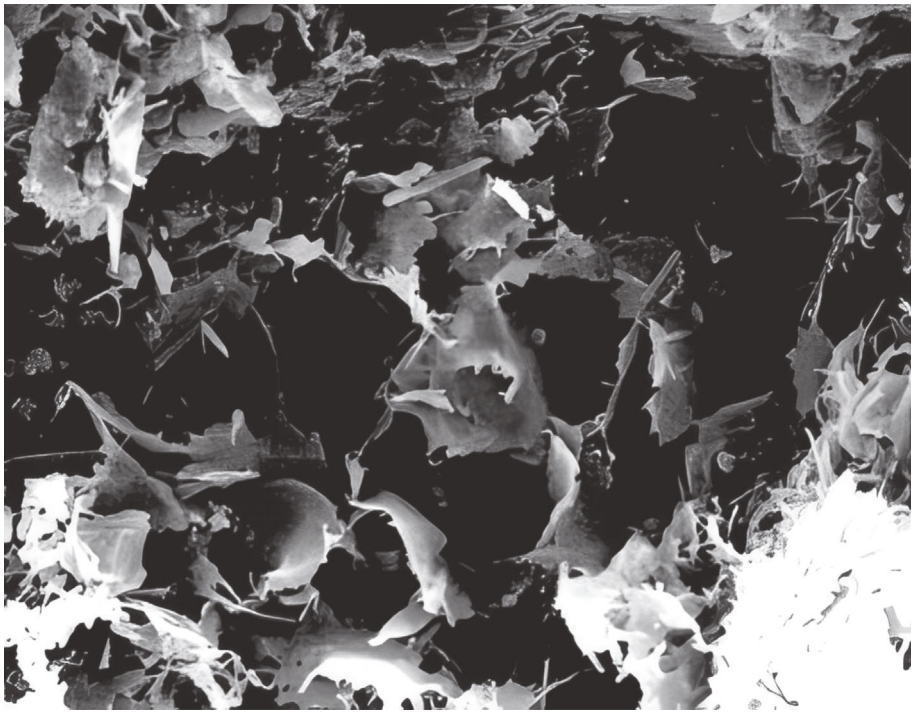

(c) Intergranular honeycomb layer

(d) Intergranular flaky illite

Figure 2: Core electron microscopic diagram of Liu 1 formation in Weizhou 11-4N oilfield (Wang Yanxing, [19]).

experiment. It provides strong guidance for the determination of efficient development and production and injection measures. At the same time, combined with the water quality compatibility experiment, a comprehensive analysis of the damage mechanism of water injection development in oilfields was carried out to provide reference for subsequent production practice.

2. Reservoir Overview

2.1. Analysis of Reservoir Heterogeneity. The fan delta front subfacies is developed in the L_1 section of Weizhou 11-4N, which is dominated by underwater distributary channel deposits. The lithological composition of the reservoir is relatively complex, including glutenite, coarse sandstone, and

Table 1: clay mineral composition table of L_1 section in Weizhou 11-4 N oilfield.

Number	Core number	Well depth (m)	Quartz (%)	Total amount of clay minerals (%)	Other minerals (%)	Illite (%)	Kaolinite (%)	Mixed layer of illite and montmorillonite (%)	Chlorite (%)
1	2-1	2603.09	70.50	14.40	15.10	70.00	11.00	15.00	4.00
2	2-4	2934.59	71.50	17.80	10.70	61.00	25.00	11.00	3.00
3	2-8	2217.00	85.20	8.20	6.60	44.00	32.00	18.00	6.00
4	2-10	2514.80	85.80	7.10	7.10	43.00	44.00	7.00	6.00
5	2-21	2778.00	87.50	9.10	3.40	48.00	39.00	9.00	4.00
6	2-13	3132.60	81.00	14.00	5.00	77.00	7.00	12.00	4.00
7	2-29	3139.50	83.00	15.30	1.70	68.00	11.00	14.00	7.00
8	2-35	2777.70	86.90	4.60	8.50	70.00	10.00	16.00	4.00
	Maximum value		87.50	17.80	15.10	77.00	44.00	18.00	7.00
Statistics	Maximum value		70.50	4.60	1.70	43.00	7.00	7.00	3.00
	Mean value		81.43	11.31	7.26	60.13	22.38	12.75	4.75

Table 2: Water sample ion concentration of the Weizhou 11-4N oilfield.

Water type	Cation (mg/L)			Anions (mg/L)				Total mineralization (mg/L)	pH value
	K^++Na^+	Mg^{2+}	Ca^{2+}	Cl^-	HCO_3^-	SO_4^{2-}	CO_3^{2-}		
Injection water	36.22	353.79	144.8	240.71	70.94	0.52	0	846.97	7
Formation water	2481	58	0	1427	4238	25	72	8301	7.71

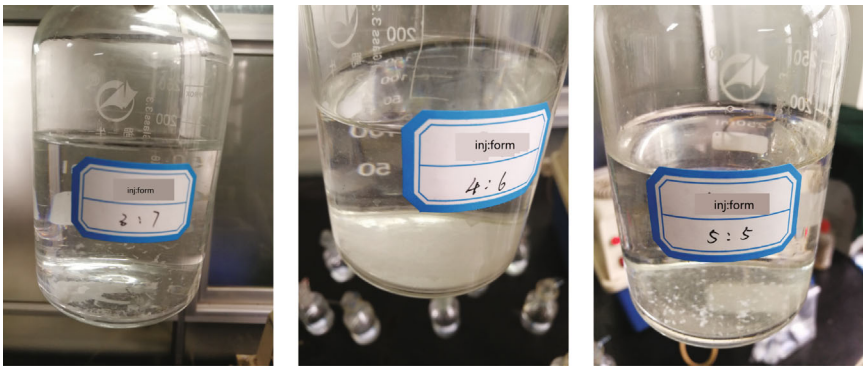

Figure 3: Some samples with serious scale after 140 days of standing.

silt-fine sandstone. The lithology is mixed and the sorting ability is poor; the overall reservoir distribution is not stable, and the vertical interlayers are developed, which are thin and interbedded, the plane phase change is fast, the lateral change is violent, and the heterogeneity is strong [5, 19]. The relative physical properties of several cores obtained from the field were measured, and the porosity of the cores was mainly distributed in the range of 9.65% to 22.27%, with an average of 15.37%; the average permeability of the cores was $12.62 \times 10^{-3}\ \mu m^2$.

2.2. Analysis of Pore Structure. Through the analysis of core pore throat by casting thin section (Figure 1), there are very few carbonate dissolved pores and intercrystalline pores in the core, and the feldspar dissolved pores are formed by local dissolution of feldspar. The quartz is cut through by microfractures and filled with micrite calcite. The intercrystalline pores and dissolved pores are randomly distributed, and the connectivity is general, but the heterogeneity is strong.

It can be seen from the core electron microscope images (Figures 2(a) and 2(b)) that the core pores are poorly developed, mainly intercrystalline pores, accompanied by a certain amount of feldspar dissolved pores, and there are few intercrystalline dissolved pores [5, 20]. The diagenetic authigenic clay mixed layer and chlorite were produced in a liner type and filled with pores, and no increase in quartz was evident. Combined with the research of Yanxing et al. (Figures 2(c) and 2(d)), the dissolution pores on the grain surface in this area were observed. There are mixed layers of authigenic quartz, flaky illite, and lamellar illite. During waterflooding development, illite can migrate under the action of water and fluid to block the pore throat, which

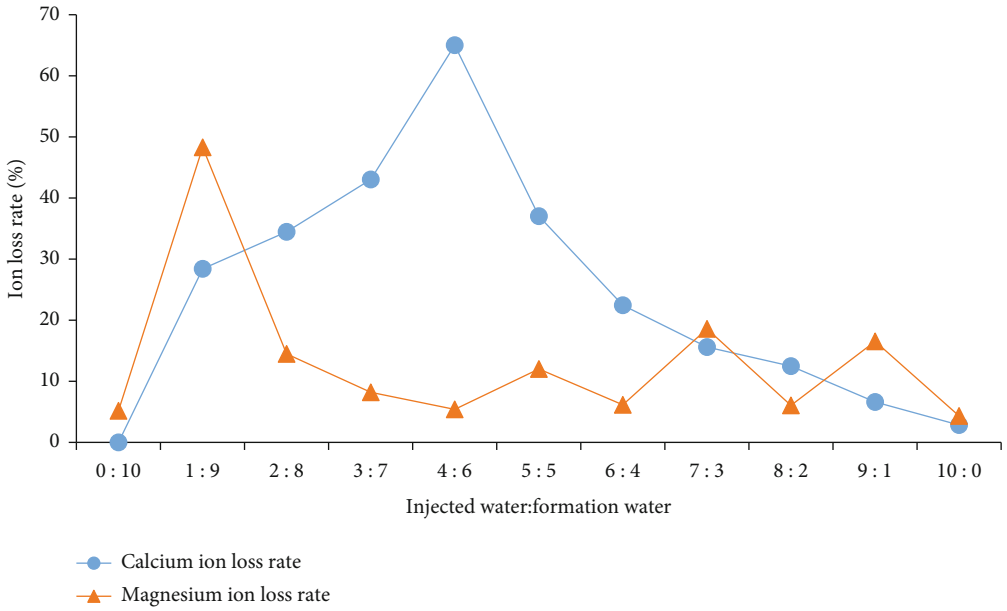

Figure 4: Water quality compatibility data chart.

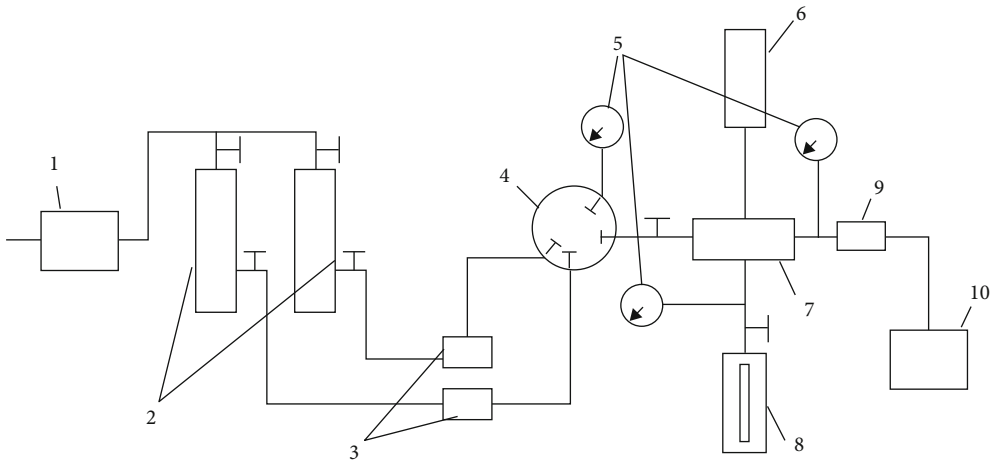

1-High pressure micro flow displacement advection pump
2-Sealed middle container
3-Filter
4-Six-way valve
5-Pressure gauge
6-Thermostat
7-Core holder
8-Manual confining pressure pump
9-Back pressure valve
10-Water separator

Figure 5: Flow chart of sensitivity experiment. 1: high pressure microflow displacement advection pump; 2: sealed middle container; 3: filter; 4: six-way valve; 5: pressure gauge; 6: thermostat; 7: core holder; 8: manual confining pressure pump; 9: back pressure valve; 10: water separator.

has potential risk of speed-sensitive and water-sensitive damage, which carries particles through fluid flushing and leads to reservoir plugging.

2.3. Reservoir Clay Mineral Analysis. The analysis of clay minerals in the cores by X-ray diffraction (Table 1) shows the content of clay minerals in the L_1 section is 4.6%-17.8%, with an average of 11.31%. Among the clay minerals, the content of illite, which is easy to cause water-sensitive and speed-sensitive damage, is relatively high, followed by kaolinite. The honeycomb-like and flake-like microscopic morphology of illite and kaolinite determines that when the injected fluid flow rate and salinity change, the particles may disperse and migrate, which in turn blocks other pore throats, resulting in a decrease in permeability and a decrease in the ability to absorb and inject water. In the L_1

Table 3: Experimental results of velocity sensitivity, water sensitivity and salt sensitivity in the Weizhou 11-4N oilfield.

Type of experiment	Sample number	Well depth (m)	Lithology	Damage rate (%)	Damage assessment
Speed sensitivity	A1	2208.53	Sandstones	96.68	Strong
Speed sensitivity	A2	2209.17	Sandstones	1455.77	Strong
Speed sensitivity	A3	2086.76	Sandstones	133.36	Strong
Speed sensitivity	A4	2171.89	Sandstones	39.05	Moderately weak
Water sensitivity	B1	2087.67	Sandstones	36.6	Moderately weak
Water sensitivity	B2	2086.79	Sandstones	78.89	Strong
Water sensitivity	B3	2209.41	Sandstones	33.04	Moderately weak
Water sensitivity	B4	2092.31	Sandstones	32.79	Moderately weak
Water sensitivity	B5	2088.73	Sandstones	41.27	Moderately weak
Water sensitivity	B6	2087.49	Sandstones	29.75	Weak
Water sensitivity	B7	2209.58	Sandstones	13.51	Weak
Salt sensitivity	C1	2209.04	Sandstones	89.11	Strong
Salt sensitivity	C2	2230.7	Sandstones	48.92	Moderately weak
Salt sensitivity	C3	2221.84	Sandstones	/	None
Salt sensitivity	C4	2225.38	Sandstones	35.35	Moderately weak

section, illite accounts for 60.13% of clay minerals on average, kaolinite accounts for 22.38% on average, and velocity-sensitive clay minerals account for as high as 82.51%. There is a potential risk of relatively strong velocity-sensitive damage in the reservoirs of L_1 section.

3. Compatibility Test of Injected Water

On the basis of the ion composition of formation water obtained from the analysis of oilfield data, the sampling was measured according to "SL394.1-2007 Determination of 34 Elements such as Lead, Cadmium, Vanadium, Phosphorus - Inductively Coupled Plasma Atomic Emission Spectroscopy (ICP-AES)." The cations of the injected water were then measured by the EDTD volumetric method, the acid-base titration method, and the silver nitrate method to measure the sulfate ion content, the carbonate, bicarbonate ion concentration, and the chloride ion concentration. The measurement results are shown in Table 2. According to the difference in water type and salinity between the injected water and the formation water from external operations, the injected water and formation water were analyzed by the Surin water type classification. The experimental results show that the formation water type is $NaHCO_3$, while the injection water type is $MgCl_2$. According to the difference in ion and salinity of formation water and injection water, there is a potential incompatibility problem [21–27].

To clarify the compatibility of injected water and formation water, an appropriate amount of simulated formation water and injection water were prepared according to the analysis results of oilfield water samples. On the basis of filtering membrane to remove suspended particles, the injected water and formation water were fully mixed according to the following proportions 1 : 0, 9 : 1, 8 : 2, 7 : 3, 6 : 4, 5 : 5, 4 : 6, 3 : 7, 2 : 8, 1 : 9, and 0 : 1 and then 11 groups of it were made. After mixing, take 200 mL of each water sample and place it in a closed sampling bottle and stand at 26°C for 140 days to observe the compatibility of injected water and formation water under different mixed concentrations. We filter on the filter and analyze its ion concentration. The results of naked eye observation and the change of ion concentration of water samples are shown in Figures 3 and 4, respectively. It can be seen from Figure 3 that the injection water and formation water have obvious scaling at 2 : 8-5 : 5, that is, the mixed water of 20% to 50% of the injection water. Furthermore, according to the change diagram of mixed water ion concentration (Figure 4), it can be seen that the mixed water samples with a calcium ion loss rate of more than 30% have scaling phenomenon, and magnesium ions have little change. The results show that the injection water and formation water in this area scale were changed. The sample is mainly calcium carbonate. The laboratory evaluation experiment on the compatibility of injected water and formation water shows that Weizhou 11-4N oilfield has a certain water quality incompatibility problem. During long-term water injection development, due to the influence of calcium carbonate scaling at some mixed concentrations, the pore throats in the formation may be blocked. As a result, the formation permeability decreases, and the water injection volume decreases and the water injection pressure increases.

Table 4: Evaluation index of damage rate.

Damage rate (%)	Degree of damage
Dv ≤ 5	None
$5 < D_v \leq 30$	Weak
$30 < D_v \leq 50$	Moderately weak
$50 < D_v \leq 70$	Moderately strong
$D_v > 70$	Strong

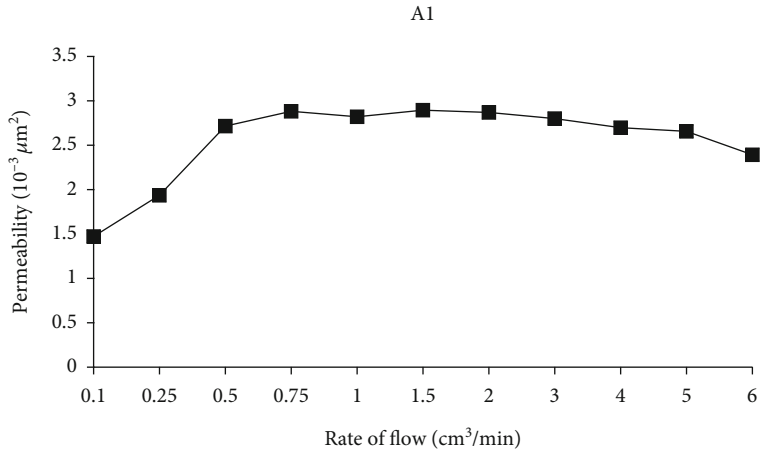

(a) A1

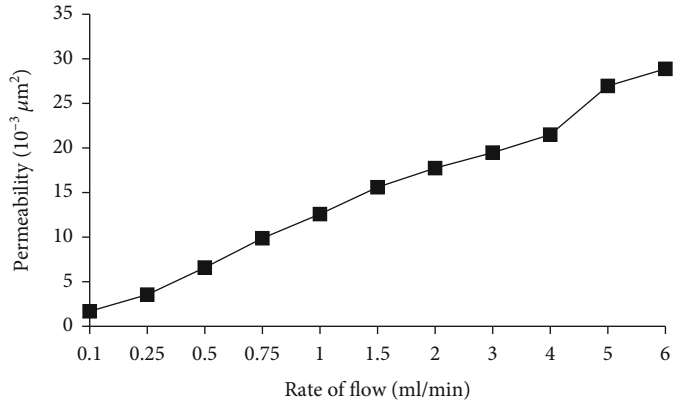

(b) A2

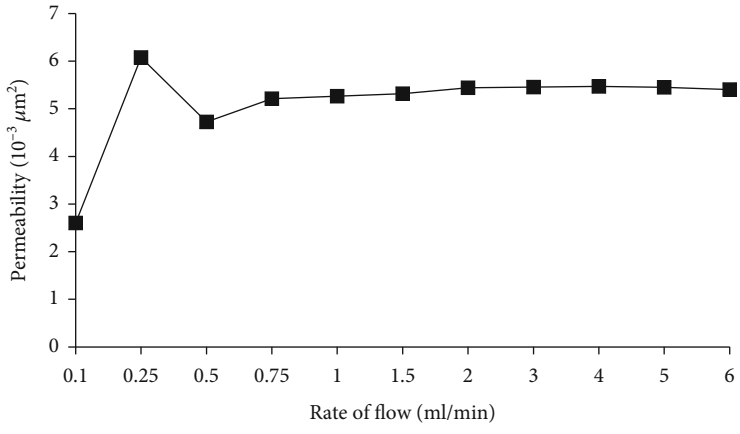

(c) A3

Figure 6: Continued.

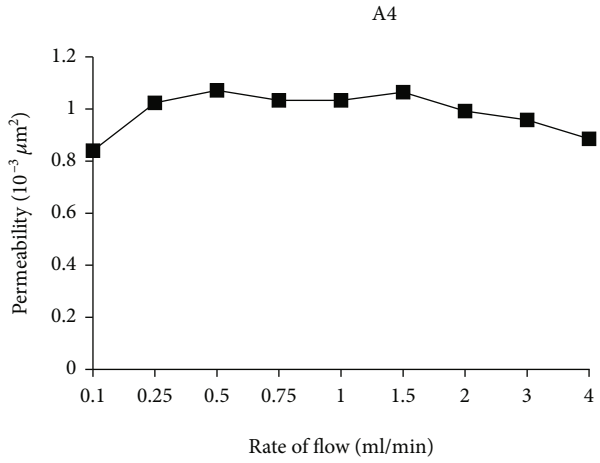

(d) A4

Figure 6: The relationship between reservoir flow rate and permeability.

4. Damage Evaluation Experiment

4.1. Preparation and Process of the Experiment. Firstly, according to "GB/T 29172-2012 Core Analysis Method," the experimental core was prepared, the porosity and permeability were measured by gas, and the simulated formation water was saturated by vacuum pumping. Then, the reservoir sensitivity experiment of Weizhou 11-4N oilfield was carried out according to the procedures and evaluation indicators specified in the petroleum industry standard "SY/T 5358-2010 Evaluation Method of Reservoir Sensitivity Flow Experiment." The experimental process is shown in Figure 5, which mainly includes high-pressure microflow displacement advection pump, manual confining pressure pump, sealed intermediate container, core holder, pressure gauge, and flow meter.

4.2. Result Analysis. According to the experimental method and standard of "SY/T 5358-2010 Experimental Evaluation Method for Reservoir Sensitive Flow," laboratory evaluation experiments on velocity-sensitive, water-sensitive, and salt-sensitive damage of 15 cores in the Weizhou 11-4N oilfield were carried out, respectively. The data and experimental evaluation results are shown in Table 3. According to the damage rate evaluation index (Table 4), it can be seen that the Weizhou 11-4N oilfield has velocity sensitivity ranging from moderately weak to strong, of which the strong velocity sensitivity accounts for 75%. There are water sensitivities ranging from weak to strong, with moderately weak water sensitivities prevailing. There are salt sensitivities ranging from non-existent to strong, with moderately weak salt sensitivities prevailing. At the same time, combined with the previous experimental results, there are alkali-sensitive and acid-sensitive damages from no to weak.

From the experimental results of velocity-sensitive damage evaluation of several cores (Figure 6), it can be seen that except for the A2 core, whose permeability increases with the increase of injection rate, the other three cores all show that the permeability first increases and then decreases with the increase of injection rate. According to the formula $D_v = ((|K_n - K_i|)/K_i) \times 100\%$, the core permeability transformation rate caused by velocity sensitivity is calculated, where K_n is the permeability of the rock sample under different flow rates, and K_i is the permeability under the minimum flow rate; the calculation formula of the damage rate is $D_V = \max(D_{v2}, D_{v3}, \cdots, D_{vn})$, the velocity-sensitive damage rate of the 4 cores is 27.56%~1607.62%, with an average of 466.31%, and the critical flow rate is 2.68~3.48 m/d, with an average of 2.98 m/d.

Further analysis of the results of the velocity sensitivity experiments on the four cores shows that, except for the A2 core, the other three cores all show that the permeability becomes an inflection point before and after the injection flow rate of 0.75 cm^3/min. When the injection flow rate is less than 0.75 cm^3/min, it increases with the injection rate. The permeability of the core increases, and the permeability decreases with the increase of the flow rate after the injection flow rate is greater than 0.75 cm^3/min. By analyzing the relationship between different flow rates and permeability damage rate (Figure 7), at low flow rate (flow rate less than 0.75 cm^3/min), the permeability increases with the increase of flow rate, and the permeability damage rate increases with the increase of flow rate and increase. At high flow rate (flow rate greater than 0.75 cm^3/min), the permeability decreases with the increase of flow rate, and the permeability damage rate also decreases with the increase of flow rate. Combined with the analysis of mineral composition and clay minerals, it is believed that when the seepage velocity is low, the migration of loose small particles in the core increases the storage space and improves the core permeability. Poor rock particles begin to migrate, migrate deep into the formation, and plug at deep pore throats, resulting in a decrease in overall permeability. It is reflected in the mine field that the water absorption capacity is reduced

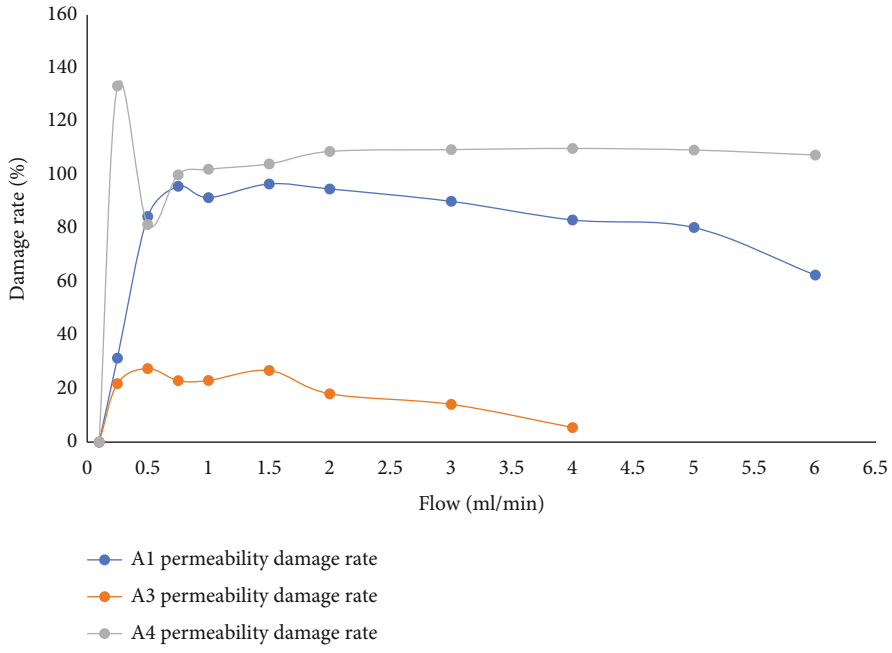

Figure 7: Relationship between damage degree of core permeability and flow rate.

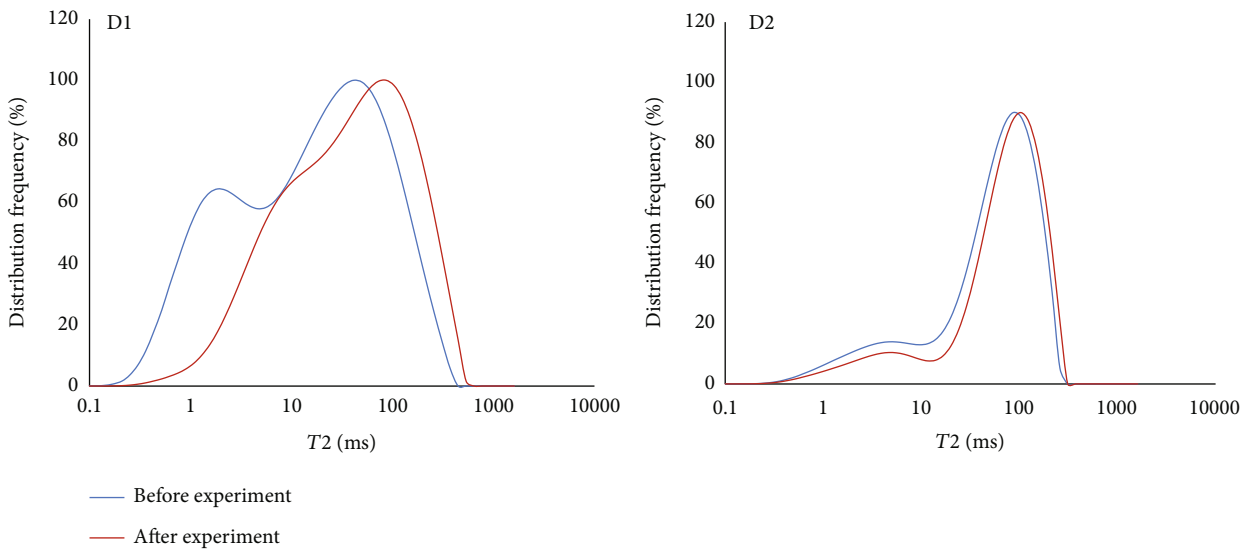

Figure 8: Contrast figure of nuclear magnetic resonance curves before and after core velocity-sensitive experiment.

and the water injection pressure is increased. Due to the short length of the core used in the experiment, the phenomenon of particle migration blocking the pore throat is not obvious enough, and the decrease of permeability is small. After analyzing the experimental process, it is believed that the A2 core has serious internal fractures due to external force factors before the experiment, which leads to the continuous increase of permeability.

In order to verify the blockage caused by the velocity-sensitive experiment, two cores D1 and D2 were selected for velocity-sensitive experiments according to the above standards, and then, the two cores before and after displacement were tested by nuclear magnetic resonance. Comparing the NMR data before and after displacement, it can be observed that after the velocity sensitivity test, the distribution frequency curves of the two cores have decreased to varying degrees in the interval of 0.1-100 ms. It shows that the proportion of small voids and small pore throats in the cores of the two samples decreased to varying degrees after the test. Larger pores and pore throats rise slightly or remain basically unchanged.

According to the data obtained by the constant-rate mercury intrusion experiment on the D1 and D2 cores before and after the experiment, the distribution map of

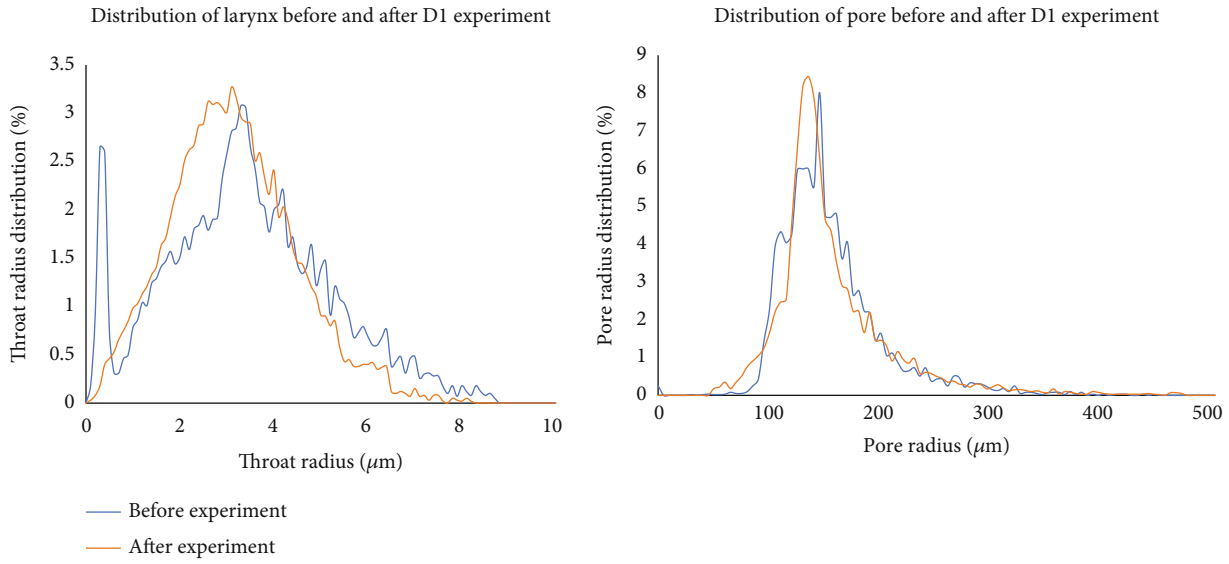

Figure 9: D1 distribution of pore and throat before and after core experiment.

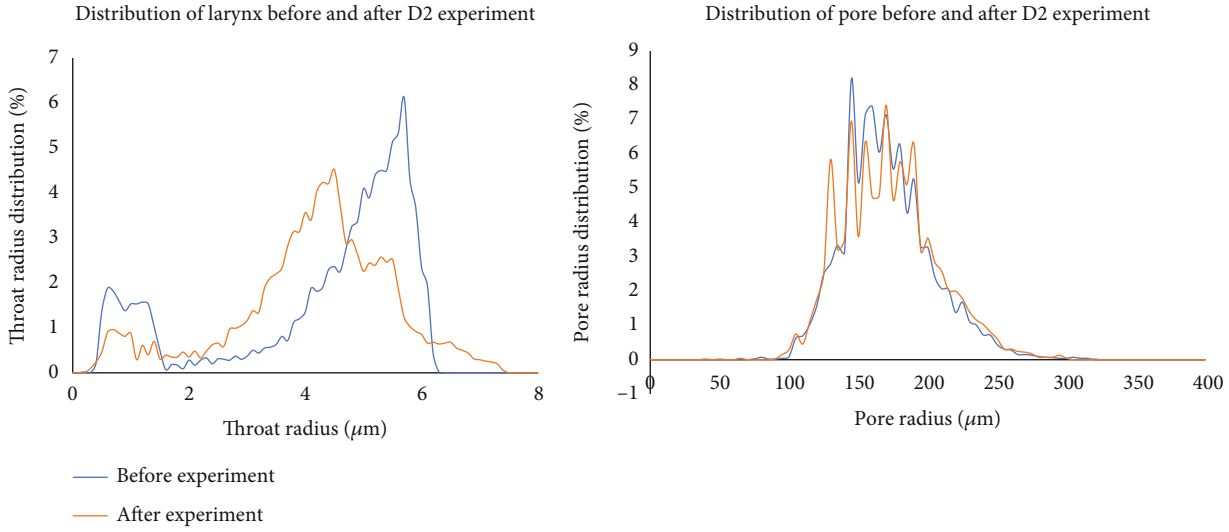

Figure 10: D2 distribution of pore and throat before and after core experiment.

the pores and throats before and after the D1 and D2 cores are drawn. From the analysis of Figures 8–10, it can be seen that after the velocity sensitivity test of the two cores D1 and D2, the proportion of pores with a size of 0-2 μm has decreased significantly. The proportion of larger pores (2-5 μm) increased slightly or remained basically unchanged. D2 showed a significant decrease in the pore throat ratio in the range of 5-6 μm. The pores with larger size were not significantly affected, and the overall proportion of the pores basically did not change before and after the experiment. Based on the analysis of the previous experiments, it is believed that in the velocity-sensitive experiment, when the flow velocity exceeds a certain limit, the loose small particles on the walls of the larger pore throats in the core begin to peel off, and these small particles migrate with the fluid. When the channel is blocked, the roars with a size of 0-2 μm decrease significantly after the test, while the proportion of the throats with larger size increases slightly due to particle migration. The decrease in the proportion of pore throats in the 5-6 μm range of the D2 core is presumed to be caused by operational errors or external factors during the experiment.

At the same time, according to the data measured in the experiment, the main flow throat radius of the D1 core is 3.42 μm before the experiment and 2.97 μm after the experiment. The average throat radius was 3.84 μm before the experiment and 3.41 μm after the experiment (Table 5). The radius of the mainstream throat was 4.68 μm before the D2 core experiment and 3.98 μm after the experiment. The average throat radius was 4.63 μm before the experiment and 4.36 μm after the experiment (Table 6).

Table 5: Throat data before and after the D1 core experiment.

	Mainstream throat radius (μm)	Maximum throat radius (μm)	Average throat radius (μm)	Relative sorting coefficient	Homogeneity coefficient
Before speed sensitivity experiment	3.42	8.70	3.84	0.47	0.39
After speed sensitivity experiment	2.97	8.20	3.41	0.40	0.38

Table 6: Throat data before and after the D2 core experiment.

	Mainstream throat radius (μm)	Maximum throat radius (μm)	Average throat radius (μm)	Relative sorting coefficient	Homogeneity coefficient
Before speed sensitivity experiment	4.68	6.30	4.63	0.37	0.69
After speed sensitivity experiment	3.98	7.40	4.36	0.32	0.56

5. Conclusion

(1) The content of clay minerals that are easy to cause velocity-sensitive damage in the first-stage reservoir of the Weizhou 11-4N oilfield exceeds 80%, and other nonclay mineral formation particles such as calcite and anorthite will also migrate with the fluid. Effects of potential sensitivity damage

(2) According to the reservoir compatibility experiment, the formation water and injection water of the Weizhou 11-4N oilfield are $NaHCO_3$ water type and $MgCl_2$ water type, respectively, and there is water quality incompatibility. It is easy to form calcium carbonate precipitation, which blocks the pore throat and causes the permeability to decrease

(3) The velocity sensitivity test results show that the reservoir in the first stage of the flow is strongly velocity-sensitive damage, with an average damage rate of 466.31% and an average critical flow rate of 2.98 m/d. Add clay stabilizers and other methods to reduce reservoir damage

(4) NMR experiments show that the velocity-sensitive damage in Weizhou 11-4 N oilfield mainly occurs in the tiny throat of 0-2 μm, and the main damage is caused by the blockage of the throat caused by particle migration. Velocity-sensitive lesions in larger throats and pores were less pronounced. After the test, the average throat radius of the two cores decreased. It can be concluded that the main reason for velocity sensitivity in the Weizhou 11-4N oilfield is the blockage of tiny throats caused by particle migration

(5) Long-term water flooding development under the action of various factors such as scaling and velocity sensitivity, the pore size of the reservoir tends to decrease, which will lead to a decrease in its permeability, and a decrease in water absorption capacity, which makes water flooding difficult

Data Availability

The (data type) data used to support the findings of this study are available from the corresponding author upon request.

Conflicts of Interest

The authors declare that they have no competing of interest.

Acknowledgments

This work is financially supported by the Development Department of Zhanjiang Branch of China National Offshore Oil Corporation (CNOOC) (China) and Key Research and Development Program of Shaanxi (Program No. 2023-YBGY-316).

References

[1] Y. Weixuan, "Nanhai West oil company will develop wei11-4 oilfield for the first time," *Petroleum Exploration and Development*, no. 6, p. 88, 1988.

[2] F. Dianjing, "Logging evaluation method and application of reservoir sensitivity in Weizhou 11-1n oilfield," *Inner Mongolia Petrochemical Industry*, vol. 37, no. 1, pp. 115–118, 2011.

[3] J. Ping, Z. Hui, W. Wenjuan, L. Biao, and T. Mingguang, "Efficient development strategy of low permeability complex fault block reservoir in Liushagang Formation of Weizhou 11-4n oilfield," *China Offshore Oil and Gas*, vol. 30, no. 6, pp. 86–91, 2018.

[4] W. Feng, L. Yuelin, and M. Guangchun, "Reservoir configuration modeling of fan delta in the first member of Liushagang Formation of Weizhou 11-1n oilfield in the western South China Sea," *China Offshore Oil and Gas*, vol. 31, no. 2, pp. 93–102, 2019.

[5] L. Shiju, G. Gang, X. Xinde et al., "Source control characteristics of oil and gas migration and accumulation in Weizhou 11-4-weizhou 11-4n oilfield, Weixinan Sag, Beibu Gulf Basin," *Natural Gas Geoscience*, vol. 30, no. 9, pp. 1312–1318, 2019.

[6] P. G. Bedrikovetsky, A. S. Vaz, C. J. Furtado, and A. L. de Souza, "Formation damage evaluation from non-linear skin growth during coreflooding," in *Paper presented at the SPE International Symposium and Exhibition on Formation Damage Control*, Lafayette, Louisiana, USA, 2008.

[7] X. Xijin and Z. Feng, "Biotite hydration mechanism and its impact on water injection development," *Journal of Southwest Petroleum University (Science & Technology Edition)*, vol. 31, no. 2, pp. 81–184, 2009.

[8] Y. Lijun and K. Yili, "Research progress on capillary self absorption of oil and gas reservoir rocks," *Journal of Southwest Petroleum University (Science & Technology Edition)*, vol. 31, no. 4, pp. 112–116, 2009.

[9] F. Yutian, T. Hongming, L. Shu, W. Yanling, and C. Chao, "Analysis of reservoir damage mechanism during water injection in Bozhong 28-2nan oilfield," *Oilfield Chemistry*, vol. 31, no. 3, pp. 371–399, 2014.

[10] R. A. Nasralla, H. Mahani, H. A. van der Linde et al., "Low salinity waterflooding for a carbonate reservoir: experimental evaluation and numerical interpretation," *Journal of Petroleum Science and Engineering*, vol. 164, pp. 640–654, 2018.

[11] S. Jianjun, T. Hongming, W. Yijun, G. Xiaoping, and Y. Hao, "Study on reservoir scaling mechanism of Shahejie Formation in Qikou 18-1 oilfield and its impact on water injection development," *Oil and Gas Reservoir Evaluation and Development*, vol. 8, no. 3, pp. 40–45, 2018.

[12] L. Wang, H. Zhang, X. Peng et al., "Water-sensitive damage mechanism and the injection water source optimization of low permeability sandy conglomerate reservoirs," *Petroleum Exploration and Development*, vol. 46, no. 6, pp. 1218–1230, 2019.

[13] R. Moghadasi, A. Rostami, A. Tatar, and A. Hemmati-Sarapardeh, "An experimental study of nanosilica application in reducing calcium sulfate scale at high temperatures during high and low salinity water injection," *Journal of Petroleum Science and Engineering*, vol. 179, pp. 7–18, 2019.

[14] P. Dongyu, T. Hongming, S. Jincheng, Z. Ju, and Z. Feng, "Study on damage mechanism during water injection in pl19-9 oilfield," *Discussion on Geological Prospecting*, vol. 35, no. 2, pp. 187–196, 2020.

[15] J. Wang and F. Zhou, "Cause analysis and solutions of water blocking damage in cracked/non-cracked tight sandstone gas reservoirs," *Petroleum Science*, vol. 18, pp. 219–233, 2021.

[16] D. Y. Zhu, Z. H. Deng, and S. W. Chen, "A review of nuclear magnetic resonance (NMR) technology applied in the characterization of polymer gels for petroleum reservoir conformance control," *Petroleum Science*, vol. 18, no. 6, pp. 1760–1775, 2021.

[17] Z. Negahdari, S. Khandoozi, M. Mojtaba Ghaedi, and R. Malayeri, "Optimization of injection water composition during low salinity water flooding in carbonate rocks: a numerical simulation study," *Journal of Petroleum Science and Engineering*, vol. 209, article 109847, 2022.

[18] Z. Yi, Z. Ningsheng, L. Xiangfang, L. Hua, and Y. Juan, "Rapid prediction of reservoir sensitivity using neural network information fusion technology," *Drilling and Production Technology*, vol. 29, no. 3, pp. 50–125, 2006.

[19] W. Yanxing, *Study on sensitivity evaluation and protection measures under reservoir conditions in Weizhou 11-4n oilfield*, Changjiang University, 2015.

[20] H. Yaotu, P. Mingyue, W. Xiaopeng, and L. Jiayu, "Protection technology of unconsolidated sandstone complex pressure reservoir," *Daqing Petroleum Geology and Development*, vol. 36, no. 5, pp. 124–130, 2017.

[21] Z. Congdi, *Analysis on influencing factors of water injection in Weizhou low permeability reservoir and research on injection increasing measures*, Xi'an Shi You University, 2021.

[22] P. Mohammadalinejad, N. Hosseinpour, N. Rahmati, and M. R. Rasaei, "Formation damage during oil displacement by aqueous S_iO_2 nanofluids in water-wet/oil-wet glass micromodel porous media," *Journal of Petroleum Science and Engineering*, vol. 182, article 106297, 2019.

[23] Z. Wang, Y. Zhang, and H. Liao, "Experimental investigation on precipitation damage during water alternating flue gas injection," *Oil & Gas Science and Technology-Revue D IFP Energies Nouvelles*, vol. 75, p. 45, 2020.

[24] J. Z. Wang, X. K. Song, L. T. Sun, Y. C. Fu, and J. J. Xu, "Water quality sensitivity and characterization of permeability of waterflooding sandstone reservoirs," *Petroleum Science and Technology*, vol. 39, no. 3, pp. 88–100, 2021.

[25] Z. Zhichao, L. Daiqiang, X. Hongrong, H. Fengze, X. Rui, and L. Yuhang, "Measures of formation damage and protection in the water-injection process —the A block in Xinjiang oil filed," *IOP Conference Series: Earth and Environmental Science*, vol. 651, no. 3, article 032042, 2021.

[26] Q. Sajjad, G. Abdolah, A. Amin, M. Santos Rafael, S. M. Saeid, and N. Milad, "Experimental and modelling approach to investigate the mechanisms of formation damage due to calcium carbonate precipitation in carbonate reservoirs," *Journal of Petroleum Science and Engineering*, vol. 205, article 108801, 2021.

[27] Y. Zhang, B. Zhang, Y. Yang, B. Liu, and L. Shen, "Storage ratio of CO_2 miscible flooding in Chang 8 reservoir of H block in Ordos Basin under different injection methods," *Frontiers in Energy Research*, vol. 10, article 848324, 2022.

Hindawi
Geofluids
Volume 2023, Article ID 7731591, 14 pages
https://doi.org/10.1155/2023/7731591

Research Article

Research on Slug Flow Elimination Method Based on Kinetic Energy Conversion

Ruiquan Liao,[1,2,3,4] **Donghui Zhou**,[2,3,4] **Zhihui Wang**,[2,3,4] **Weixia Yang**,[5] **and Xingkai Zhang**[1,2,3,4]

[1]*Key Laboratory of Exploration Technologies for Oil and Gas Resources (Yangtze University), Ministry of Education, Wuhan, China 430100*
[2]*Petroleum Engineering Institute of Yangtze University, Wuhan, China 430100*
[3]*Laboratory of Multiphase Pipe Flow, Gas Lift Innovation Center, China National Petroleum Corp., Wuhan, China 430100*
[4]*Key Laboratory of Drilling and Production Engineering for Oil and Gas, Wuhan, China 430100*
[5]*Jinchang PetroChina Kunlun Gas Co., Ltd., Jinchang, China 737100*

Correspondence should be addressed to Xingkai Zhang; zhangxingkai001@163.com

Received 19 October 2022; Revised 7 November 2022; Accepted 24 November 2022; Published 30 January 2023

Academic Editor: Ze Wang

Slug flow is one of the most common flow patterns in the petrochemical industry. It will affect the normal operation of oil well surface pipelines and connected equipment, especially gas well multiphase flowmeters. The extant slug flow traps are complex in structure and limited in application sites. To reduce the influence of slug flow on gas-liquid two-phase measurement, a slug flow elimination device is designed based on the kinetic energy conversion method. The gas-liquid two-phase flow law inside the device and its energy loss are investigated using a combination of indoor experiments and numerical simulations. This study evaluates the device's working performance, including the flow pattern, pressure fluctuation, velocity distribution, and energy loss. The results show that the flow rate and pressure fluctuation of the gas-liquid two-phase flow are weakened after the device. And the flow pattern changes from intermittent slug flow to gas-liquid continuous flow. The pressure drop calculation method for the device is developed based on the share of different structures in the total pressure drop, with a prediction error of 20%. The slug elimination device is designed to provide a flow pattern basis for metering equipment, improve metering accuracy, and further promote the development of multiphase metering technology.

1. Introduction

The fluids produced from oil wells may be a gas-liquid two-phase flow in many cases. Slug flow is a common gas-liquid two-phase flow pattern. Slug flow will affect the stable operation of the oil well surface pipeline and the equipment connected to the pipeline. In particular, slug flow will cause large measurement errors in the real-time measurement of oil well production [1]. A large number of studies have been conducted to investigate the kinematic characteristics of slug flow [2–5]. Based on the existing theories, the optimal method to reduce or eliminate the slug flow is sought [6]. Meng et al. [7] and Zheng et al. [8] installed a cyclone upstream of the gas-liquid measurement device to eliminate the slug so that the flow through the measurement device is annular. They concluded that the cyclone can force the downstream flow pattern into an annular flow and obtained a stable differential pressure, thus obtaining high measurement accuracy. Passive section slug control can also be achieved by using many devices or techniques, commonly installing flow pattern adjusters [9, 10], multiple riser combinations [11], gas lift method [12], bubble crushers [13], mixing devices [14], and slug flow traps [15], etc. In general, according to the site production needs, different types of slug flow elimination devices can be chosen [16]. If the slug flow can be effectively eliminated, it will not only provide a good

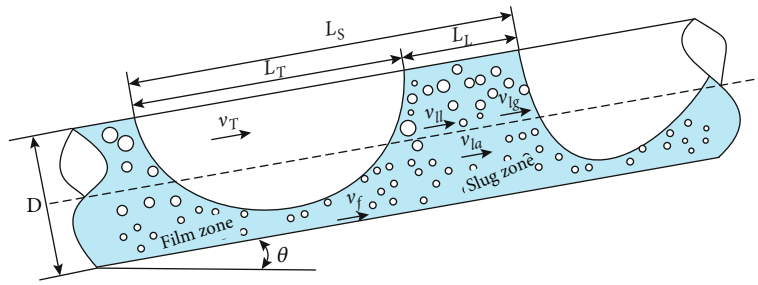

Figure 1: Geometric model of the slug flow in the inner section of the slightly inclined pipe.

flow basis for gas-liquid measurement but also improve the stability of equipment operation [17, 18].

To eliminate the measurement error caused by a sudden change in the flow pattern, the experimental study of the slug flow elimination method under different working conditions is the most convincing. Experimental studies are limited to some extent due to the disadvantages such as the high cost of experimental equipment and low reusability. Researchers began to seek more accurate and predictive tools for the study of gas-liquid two-phase flow laws [19]. Among them, Computational Fluid Dynamics (CFD) methods are coming into the researchers' view, and they will be a valuable addition to the toolbox [20].

The purpose of this study is to eliminate or weaken the slug flow and provide a stable flow pattern for gas-liquid two-phase measurements while increasing the stability of the instrument operation. Based on the principle of kinetic energy conversion and turbulent diffusion [21], a new slug flow elimination method is put forward to change the distribution pattern of gas and liquid phases [22]. This method can effectively reduce the slug flow frequency and achieve the purpose of weakening or eliminating the slug flow. The performance of the slug flow elimination device is tested by experimental and numerical simulation, and the pressure drop calculation model of the device is also established.

2. Model Building and Methodology

2.1. Slug Flow Model. When the gas-liquid two-phase flow flows through the horizontal- or upward-inclined pipeline, the liquid moves forward under the action of a pressure gradient to overcome gravity and friction. When the pressure gradient or gas-carrying role is large enough, the liquid has a large kinetic energy and can flow together with the gas. On the contrary, the impact of gravity and friction will move the liquid behind the gas, causing the liquid to accumulate in the pipe, and then generating hydraulic slug flow. Therefore, if the energy of the liquid is increased by certain means, the slug flow can be eliminated.

As shown in Figure 1, the total length of a hydraulic slug flow unit is L_S, which mainly consists of a liquid film zone and a liquid slug zone. Assume that the length of the liquid slug zone is L_L and the length of the liquid film zone is L_T, where the liquid film zone consists of Taylor bubbles and liquid film. The hydraulic section slug flow is accompanied by the accumulation of the liquid phase at the head of the slug and the loss of the liquid phase at its tail during the movement.

Taking the slug flow unit as the object of study, the continuity equation is established based on the conservation of mass of the slug flow per unit of time.

$$\text{Liquid}: \frac{v_{sl}\rho_l}{e} = v_{ll}t_s H_{ls}\rho_l + v_f t_f H_{lf}\rho_l, \tag{1}$$

$$\text{Gas}: \frac{v_{sg}\rho_g}{e} = v_{\text{lg}}t_s(1-H_{ls})\rho_g + v_T t_f\left(1-H_{lf}\right)\rho_g, \tag{2}$$

where v_{sl} and v_{sg} represent the superficial velocity of liquid and gas, respectively, m/s. v_{ll} and v_f represent the liquid phase velocity in the liquid slug and liquid film zones, respectively, m/s. H_{ls} and H_{lf} represent the liquid holdup in the liquid slug and liquid film zones, respectively, dimensionless. e is the frequency of the slug flow, Hz. v_{lg} and v_T are the bubble velocity and Taylor bubble velocity in the liquid slug zone, respectively, m/s. ρ_l and ρ_g represent the density of the liquid and gas, respectively, kg/m^3. t_s and t_f represent the time for the liquid slug and Taylor bubble to pass a point, respectively, s.

$$t_s = \frac{L_L}{v_{ll}}, \tag{3}$$

$$t_f = \frac{L_f}{v_f}. \tag{4}$$

Substituting Equations (3) and (4) into Equations (1) and (2), respectively, we get

$$\frac{v_{sl}}{e} = \frac{L_L H_{ls} v_{ll}}{v_{la}} + L_f H_{lf}, \tag{5}$$

$$\frac{v_{sg}}{e} = \frac{L_L v_{\text{lg}}}{v_{la}}(1-H_{ls}) + \frac{L_f}{v_f}\left(1-H_{lf}\right)v_T. \tag{6}$$

The Taylor bubble motion process causes the interconversion of the liquid slug and liquid film zones, and in the steady state, the mass exchange is

$$H_{ls}(v_T - v_{ll}) = H_{lf}\left(v_T - v_{lf}\right). \tag{7}$$

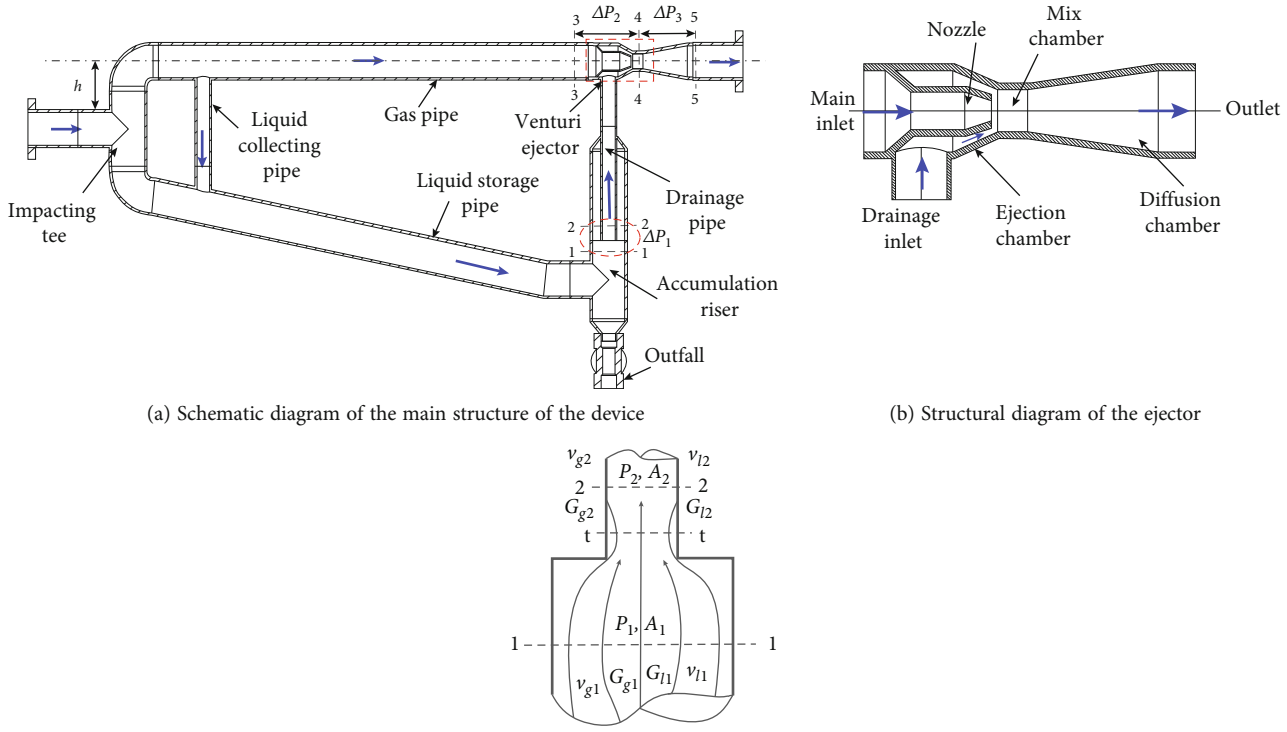

(a) Schematic diagram of the main structure of the device

(b) Structural diagram of the ejector

(c) Structure diagram of the drainage pipe inlet

Figure 2: Schematic design of the main structure of the slug flow elimination device (the blue arrow is the flow direction).

A certain amount of liquid holdup is the basic condition for the formation of slug flow. The liquid holdup in the liquid slug zone is much larger than that in the liquid film zone in the slug flow unit. The liquid holdup of the slug is calculated according to the relationship proposed by Gregory [23], namely,

$$H_{ls} = \frac{1}{1 + [v_m/8.66]^{1.39}}. \tag{8}$$

The velocity of the mixture (v_m) in the slug flow unit can be expressed as

$$v_m = v_{sl} + v_{sg}. \tag{9}$$

2.2. Structure and Working Principle. The elimination device designed and processed in this study mainly consists of an impacting tee, an ejector, a liquid accumulation riser, a liquid storage pipe, and a gas pipe, and the structure is shown in Figure 2(a). Among them, the main function of the impacting tee is to separate the liquid slug area and liquid film area of the slug flow unit, so that the gas-liquid two phases are reorganized at the Venturi throat. When the slug flow passes through the inlet impacting tee, the kinetic energy of the liquid along the axial direction disappears and flows into the liquid storage pipe by its gravity. The impacting tee has little effect on the gas superficial velocity, and the gas in the Taylor bubble enters the horizontal gas pipe. The role of the ejector is to convert part of the gas energy into the liquid. The gas velocity increases and pressure decrease as it flows through the nozzle. Low pressure draws the liquid in the accumulation riser into the mix chamber (Figure 2(b)), achieving gas-liquid kinetic energy exchange so that the liquid velocity increases. By recombining the gas-liquid phases through the ejector, the energy distribution of each phase in the pipe and the liquid content distribution in the cross-section are changed. When the liquid content of the treated section does not meet the conditions for the formation of slug flow [24], the slug disappears.

3. Experimental System

3.1. Experimental Procedure. Water and air are used as media for the experiment. The experimental fluid is supplied through a water pump and an air compressor. The high-pressure gas in the storage tank is dried and processed into the slug flow elimination device. The separated gas is directly discharged into the air, and the water is recycled. The experimental flow is as shown in Figure 3. In this experiment, an "L" riser is set at the inlet to simulate the slug flow, so that the flow pattern entering the separation device is a slug flow. The experimental setup is shown in Figure 4(d).

3.2. Experimental Equipment. The liquid flow rate is given by adjusting the pump inverter to change the liquid flow rate into the mixer. The gas flowmeter used in this experiment is a thermal gas mass flowmeter with a measurement range of 5 m^3/h to 400 m^3/h and an accuracy of ±1.5%. The liquid flow rate is measured by a Coriolis force mass flowmeter with a range of 0 to 1.5 kg/s and an accuracy of ±0.1%. Pressure sensors are installed at the inlet and outlet of the

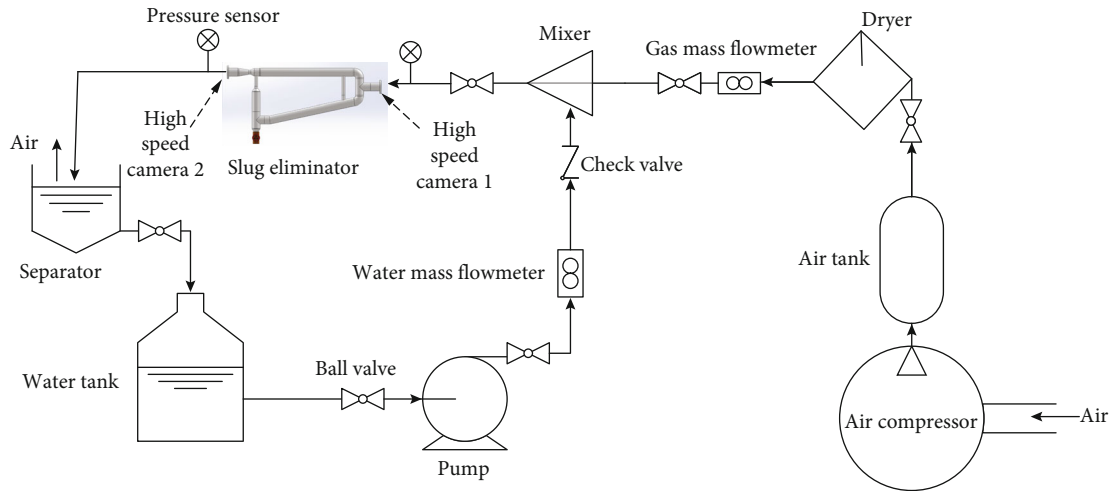

Figure 3: Experimental flow chart.

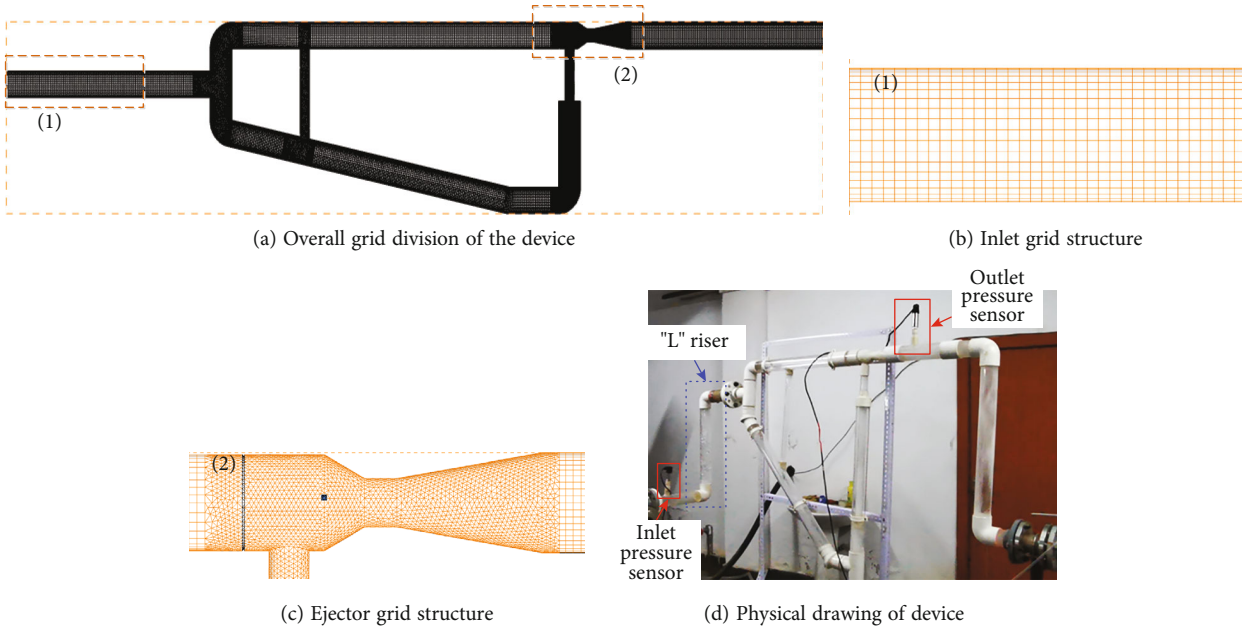

(a) Overall grid division of the device

(b) Inlet grid structure

(c) Ejector grid structure

(d) Physical drawing of device

Figure 4: Physical model and grid structure (the blue dotted box is the "L" riser).

elimination device to record the pressure change before and after entering the device, to judge the effect of slug flow elimination. The pressure sensors at the inlet and outlet have a range of 0~0.6 MPa and an accuracy of ±0.1%. The output of the flowmeter and differential pressure sensor is a 4-20 mA current signal, and all parameters are collected and stored using an NI PCI-6220 64-bit multifunctional data acquisition card with a 200 Hz data acquisition frequency.

3.3. Numerical Simulation. Slug flow is an intermittent flow between gas-liquid phases and requires specific operating conditions to be formed. Therefore, this simulation utilizes the user-defined function (UDF) to customize the gas-liquid flow at the inlet to ensure that the two phases can form a slug flow before entering the device. According to the experimental findings, the loading and unloading processes of the compressor lead to a sinusoidal variation of the gas flow [25]. So the inlet mass flow curve is defined as a sinusoidal fluctuation law during the numerical simulation. The numerical simulation results are verified by experiments with the same structure.

3.4. Physical Model and Grid. When building the physical model, the inlet and outlet pipe lengths were increased to observe the slug flow elimination effect. The inner diameters of both outlet and inlet pipes are 60 mm, the inner diameters of both descending and inducing pipes are 25 mm, and the throat diameter ratio of the ejector is 0.4. To improve the mesh quality and enhance the calculation accuracy, the structure is first divided into blocks, and the structured meshing method is used for the regular structure. The

ejector and the impacting tee use the tetrahedral meshing method, and the mesh structures are shown as follows in Figures 4(a)–4(c).

3.5. Multiphase Flow Model. The VOF model is chosen for this simulation to simulate the gas-liquid distribution law with the following control equation.

$$\frac{\partial \alpha_q}{\partial t} + \vec{v} \cdot \nabla \alpha_q = \frac{S\alpha_q}{\rho_q}. \tag{10}$$

By default, the source term at the right of Eq. (10) is zero, except when a constant or a user-defined mass source is specified for each phase. The volumetric ratio equation is not solved for the main phase. The calculation of the volume ratio for the main phase is based on the following constraint.

$$\sum_{q=1}^{n} \alpha_q = 1. \tag{11}$$

Solving for a single momentum equation over the entire zone, the resulting velocity field is shared by all phases. As shown below, the momentum equation depends on the volume ratio of all phases of ρ and μ.

$$\frac{\partial}{\partial t}\left(\rho\vec{v}\right) + \nabla \cdot \left(\rho\vec{v}\vec{v}\right) = -\nabla p + \nabla \cdot \left[\mu\left(\nabla\vec{v} + \nabla\vec{v}^{T}\right)\right] + \rho\vec{g} + \vec{F}. \tag{12}$$

In this simulation, the gas is used as the primary phase and the liquid as the secondary phase, and the density in each grid cell is calculated using the following equation.

$$\rho = \rho_g \alpha_q + \rho_l\left(1 - \alpha_q\right), \tag{13}$$

where $\vec{v}$ is the velocity of the fluid, α_q is the q-th phase volume fraction, ρ_q is the q-th density, p is the static pressure, μ is the fluid's dynamic viscosity, and $\vec{F}$ is the surface tension between the two phases.

3.6. Turbulence Model. The RNG $k-\varepsilon$ model is capable of simulating moderately complex flows such as jet impingement, separated flows, secondary flows, and cyclonic flows. The model is derived from the transient *N-S* equation using the mathematical method of the "renormalization group." The resolvability is converted from the standard $k-\varepsilon$ model, and new functions or terms appear in the equations, whose turbulent kinetic energy and dissipation rate equations are

$$\rho\frac{Dk}{Dt} = \frac{\partial}{\partial x_i}\left[\left(\alpha_k \mu_{\text{eff}}\right)\frac{\partial k}{\partial x_i}\right] + G_k + G_b - \rho\varepsilon - Y_M, \tag{14}$$

$$\rho\frac{D\varepsilon}{Dt} = \frac{\partial}{\partial x_i}\left[\left(\alpha_\varepsilon \mu_{\text{eff}}\right)\frac{\partial \varepsilon}{\partial x_i}\right] + C_{1\varepsilon}\frac{\varepsilon}{k}\left(G_k + C_{3\varepsilon}G_b\right) - C_{2\varepsilon}\rho\frac{\varepsilon^2}{k} - R, \tag{15}$$

where G_k is the turbulent kinetic energy due to the velocity gradient; G_b is the turbulent kinetic energy due to buoyancy; Y_M is the fluctuation due to the diffusion of the transition in compressible turbulence; $C_{1\varepsilon}$, $C_{2\varepsilon}$, and $C_{3\varepsilon}$ are constants; and α_K and α_ε are the inverse of the effective turbulent Prandtl number for the turbulent kinetic energy k and the dissipation rate ε, respectively.

3.7. Boundary Conditions. The inlet and outlet boundary types are set as the mass flow inlet and pressure outlet, respectively. The inlet pressure is 0.1 MPa, and the inlet mass flow rate is assigned by UDF. The turbulence definition method selects the turbulence intensity and hydraulic diameter; the no-slip wall condition is used; i.e., the wall velocity is 0. The gas-liquid surface tension is set to 0.0072 N/m. The parameters such as phase content, pressure, and phase velocity in the flow direction are recorded during the simulation.

4. Results and Discussion

4.1. Flow Pattern. Flow pattern variation is the main cause of pressure in the pipe [26]. As Figure 5(a) shows, the inlet is a slug flow, and bubbles are found in the liquid slug in the slug flow unit. The closer to the end of the liquid slug, the larger the bubble is. This is caused by the pressure between the liquid film and the liquid slug becoming smaller. When the slug flow enters the device, a large amount of liquid is initially separated into the descending pipe under the small gas-liquid ratio condition, and a small amount of liquid is carried to the horizontal pipe by the gas. The preliminary separation of the gas and liquid is obvious, in which a small amount of liquid in the gas pipe flows into the liquid collection pipe through the descending pipe. The gas imparts kinetic energy to the liquid in the mix chamber of the ejector, which improves the velocity of the liquid and reduces the accumulation of liquid in the riser. After passing through the elimination device, the liquid slug and Taylor bubble are separated, and the flow pattern formed after the second mixing is as Figure 5(b) shows. From Figure 5(b), it can be seen that the flow pattern at the outlet has changed from slug flow to transition flow and gradually transformed to annular flow. Due to gravity, the liquid phase at the outlet is deposited at the bottom of the pipe, forming a small wave, and a fine liquid flow is formed around the pipe wall, which temporarily fails to form a complete liquid film.

The liquid holdup is one of the main variables describing the slug flow. Therefore, the magnitude of the liquid holdup not only affects the pressure fluctuation but will also determine the slug flow elimination effect. According to the Gregory et al. [27] study, the liquid holdup of the pipe cross-section capable of slug flow is 48%. The experimental results show that when the gas-liquid ratio is greater than 380 m^3/m^3, it is difficult to form slug flow in the pipe. However, a large gas-liquid ratio still leads to a liquid-phase impact on the impacting tee and a significant wave pattern in the outlet pressure.

When the kinetic energy of the gas is small, it cannot pump the liquid in the accumulation riser in time, causing it to accumulate (Figure 6(a)). When the gas cannot continuously transfer its kinetic energy to the liquid, the liquid

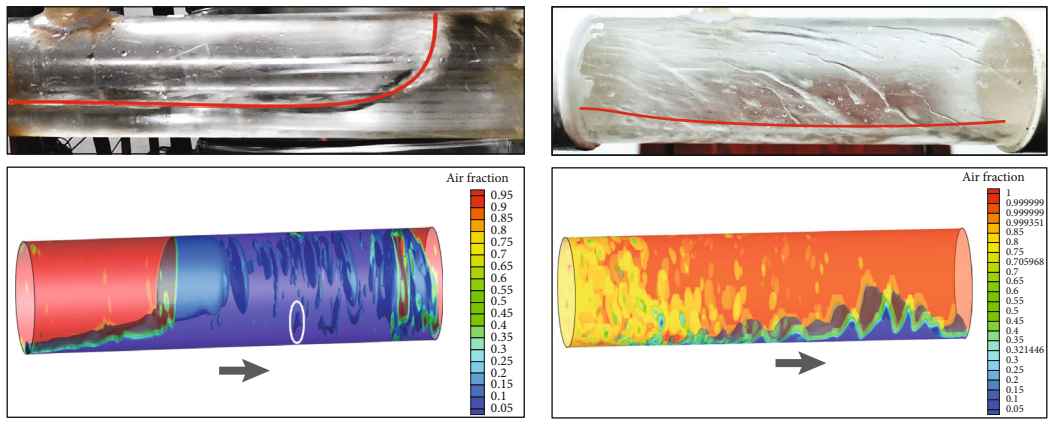

(a) Inlet flow pattern ($Q_l = 0.42\,m^3/h$, $Q_g = 41.6\,m^3/h$) (b) Outlet flow pattern ($Q_l = 0.42\,m^3/h$, $Q_g = 41.6\,m^3/h$)

Figure 5: Fluid motion at the inlet and outlet of the experimental setup.

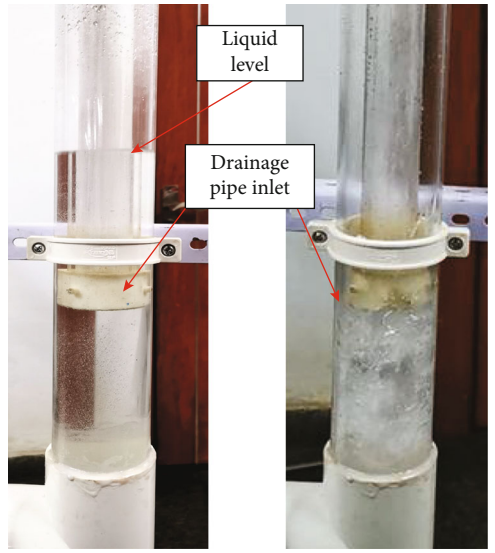

($Q_l = 1.67\,m^3/h$, $Q_g = 41.6\,m^3/h$) ($Q_l = 0.42\,m^3/h$, $Q_g = 41.6\,m^3/h$)

(a) (b)

Figure 6: Liquid state of the accumulation riser with a different gas-liquid ratio.

entering the priming chamber appears to oscillate at the inlet of the drainage pipe (Figure 6(b)). Figure 7 shows the distribution of the liquid phase at $t = 2.2\,s$ under different gas-liquid ratio conditions. As the gas-liquid ratio gradually increases, the initial separation effect of the impacting tee on the two-phase gas-liquid decreases, and a vortex is generated at the elbow. More liquid enters the gas pipe. The liquid phase entering the gas pipe makes the flow rate at the nozzle fluctuate, and the energy conversion between the gas and liquid phases is then affected. When the gas-liquid ratio is greater than $120\,m^3/m^3$, a complete slug flow is not formed at the inlet due to the reduced liquid content in the pipe. It can be seen from the outlet pressure curve that the gradual increase of the gas-liquid ratio increases the outlet pressure amplitude. Due to the small liquid content rate, a full pipe flow cannot be formed in the accumulation riser, and the intermittent supply of liquid from the riser to the inlet pipe results. Therefore, the pressure fluctuations generated at a gas-liquid ratio greater than $120\,m^3/m^3$ cannot be used to define the applicability of the device.

4.2. Pressure Fluctuation. From the experimental phenomena, it is clear that the slug flow pressure signal has the following characteristics.

(1) The pressure fluctuation time in the liquid film area is long, the amplitude is small, and there are obvious fluctuations in the pressure rise phase with a step-up pattern

(2) The pressure amplitude in the liquid slug area is large, has a short duration, and shows a vertical wave, and the pressure reaches the highest point when a precipitous drop occurs [25].

Combining Figures 5 and 8(a), it can be seen that the pressure at the outlet depends on the various flow patterns.

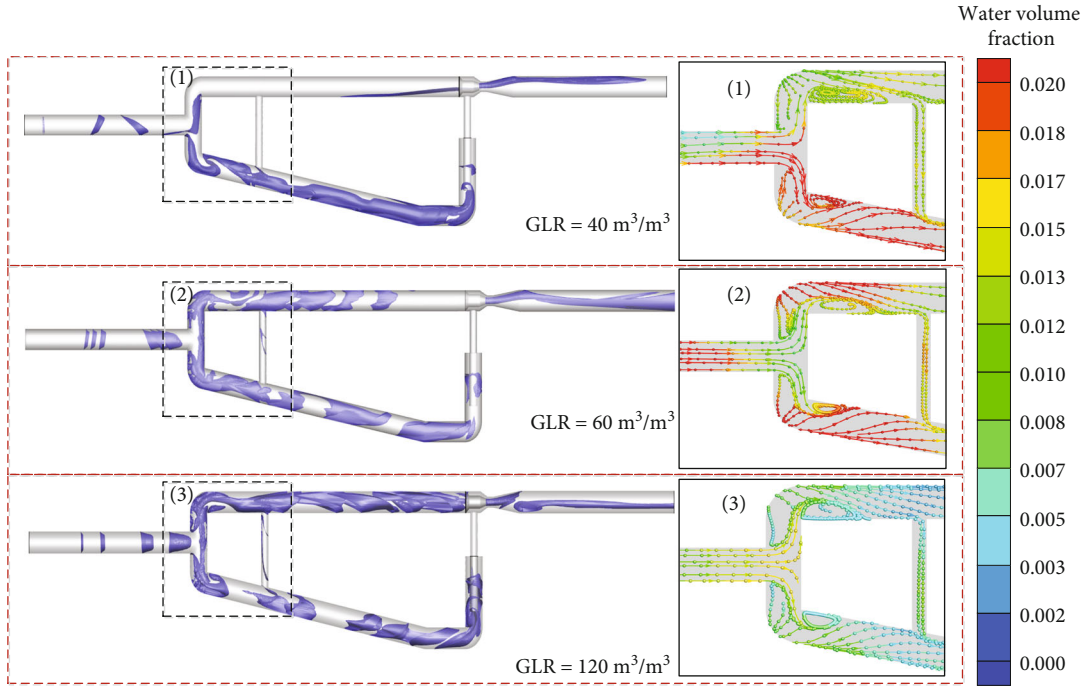

Figure 7: Gas-liquid distribution under different gas-liquid ratios ($t = 2.2$ s).

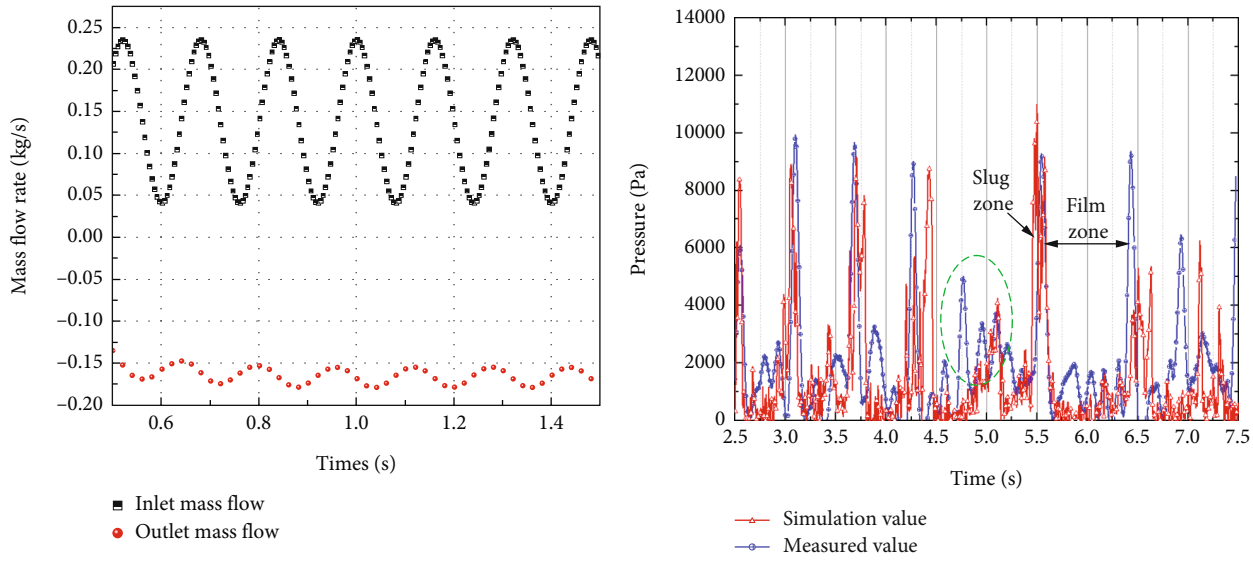

(a) Mass flow rate at inlet and outlet (GLR = 100 m³/m³)

(b) Experimental and simulated pressure curves

Figure 8: Variation of flow and pressure at the inlet and outlet.

Under non-slug flow conditions, both mass flow and pressure tend to stabilize, which can further improve the accuracy of the gas-liquid two-phase measurement device and its stability. From Figure 8(b), which shows various patterns of the inlet pressure, it can be seen that the various patterns of simulated and measured pressures are almost the same at the same time nodes. The two have a high degree of agreement. Due to the loading and unloading of the air compressor during the experiment, which leads to the unstable gas-liquid flow, it will form as shown in Figure 8(b) (green dashed line). That is, the measured pressure value occasionally shows large fluctuations at the position of the trough, and the pressure measurement is slightly higher than that of the simulated value. Comparing the variation laws of pressure, flow pattern, and other parameters under experimental and numerical simulation conditions, respectively, it is verified that the numerical simulation method can accurately describe the gas-liquid two-phase flow pattern and its motion law.

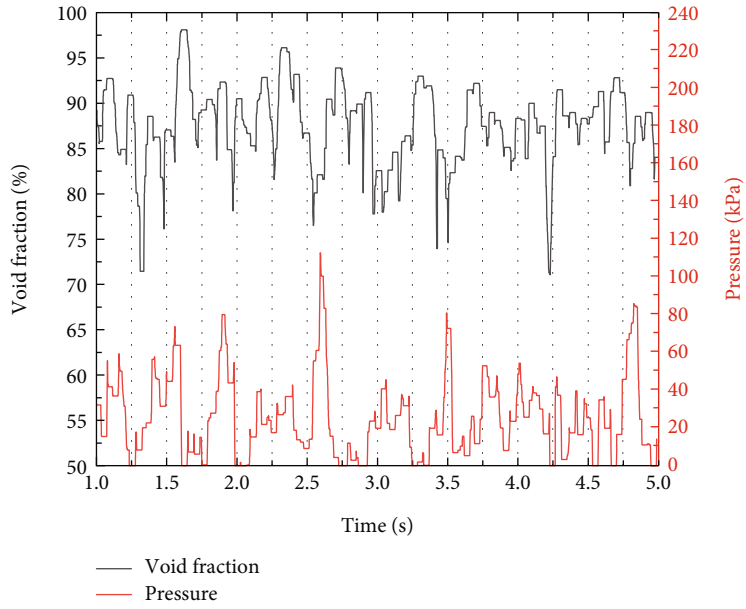

Figure 9: Variation curve of cross-sectional void ratio and pressure.

The relationship between the void fraction and pressure at the cross-section 400 mm from the inlet before the liquid slug enters the impacting tee (GLR = 60 m^3/m^3) was simulated in this study, as shown in Figure 9. The graph shows that the pipe pressure reaches its maximum value when the void fraction reaches its minimum value, i.e., when the cross-sectional liquid content is at its maximum. When the cross-sectional liquid content increases, the pressure starts to build up in the Taylor bubble at the moment when the liquid slug blocks the gas passage. When the pressure at the end of the slug is greater than the pushing force required for the movement of the slug, the slug is discharged. At this point, the Taylor bubble acts as a "piston" and pushes the liquid slug to move. Combined with Figure 9, it can be seen that the larger the gas-liquid ratio, the larger the void ratio, and the smaller the average cross-sectional liquid content, the smaller the pressure in the pipe and the smaller the amplitude of pressure fluctuation.

Combined with the flow pattern variation at the inlet and outlet, it shows that the magnitude of the pressure fluctuation depends on the velocity of the slug flow, and the length of the slug flow determines the duration of the pressure peak. From the results of Figure 10, it can be seen that the higher the liquid phase flow rate, the higher the pressure and the greater the amplitude of its fluctuation under the same gas flow rate. The smaller the gas-liquid ratio, the longer the duration of the pressure wave. The pressure fluctuations at the inlet and outlet have obvious differences. Among them, the high-frequency pressure signal at the inlet shows obvious slug flow characteristics, but the inlet slug flow pressure signal occasionally shows abnormal fluctuations at the trough during the experiment due to the influence of compressor loading (Figure 10(a) marked by a red solid line). During the experiment, it was found that when the liquid slug reached the top of the riser, the pressure reached a peak at that time. When the slug is discharged momentarily, the pressure suddenly decreases. As the gas-liquid ratio gradually decreases, the liquid slug stagnates at the riser and a small amount of liquid then flows back, causing the pressure signal at the inlet to fluctuate at the crest, as shown in Figures 10(b) and 10(c) marked by the red solid line. Combined with Figure 8(a), which shows the mass flow rate variation law, it can be seen that the stability of the outlet pressure depends on whether its mass flow rate is stable.

4.3. Velocity Distribution. From the internal streamline diagram of the ejector (Figure 11), it can be seen that the velocity is smaller near the pipe wall and is larger in the center where the liquid content is small. The velocity before entering the ejector is about 1.15 m/s and reaches 13.41 m/s inside the mix chamber (GLR = 40 m^3/m^3). The sudden increase in velocity caused a sharp drop in pressure in the mix chamber due to the reduced-flow cross-section of the nozzle. To maintain the local pressure balance, the pressure in the induced chamber also decreases simultaneously. The liquid in the accumulation riser is pumped into the mix chamber by negative pressure and then enters the expansion pipe after being accelerated by high-speed gas, forming a non-slug flow downstream. As the gas-liquid ratio increases, the flow rate in the mix chamber gradually increases, and the suction force continues to increase.

Due to the existence of friction between the liquid and the pipe wall, the flow rate gradually decreases from the center to the wall. Among them is the location of the thin layer near the inner wall, which is a thin layer of resistance; this thin layer is called the boundary layer. In the flow through the throat, the fluid increases the velocity and decreases the pressure, maintaining the original surface layer. Downstream of the throat, the flow area increases, the kinetic energy of the fluid is converted into pressure energy, and the boundary layer is subject to the force of the opposite direction of the mainstream, resulting in fluid backflow. Beyond the boundary layer of the fluid to maintain the

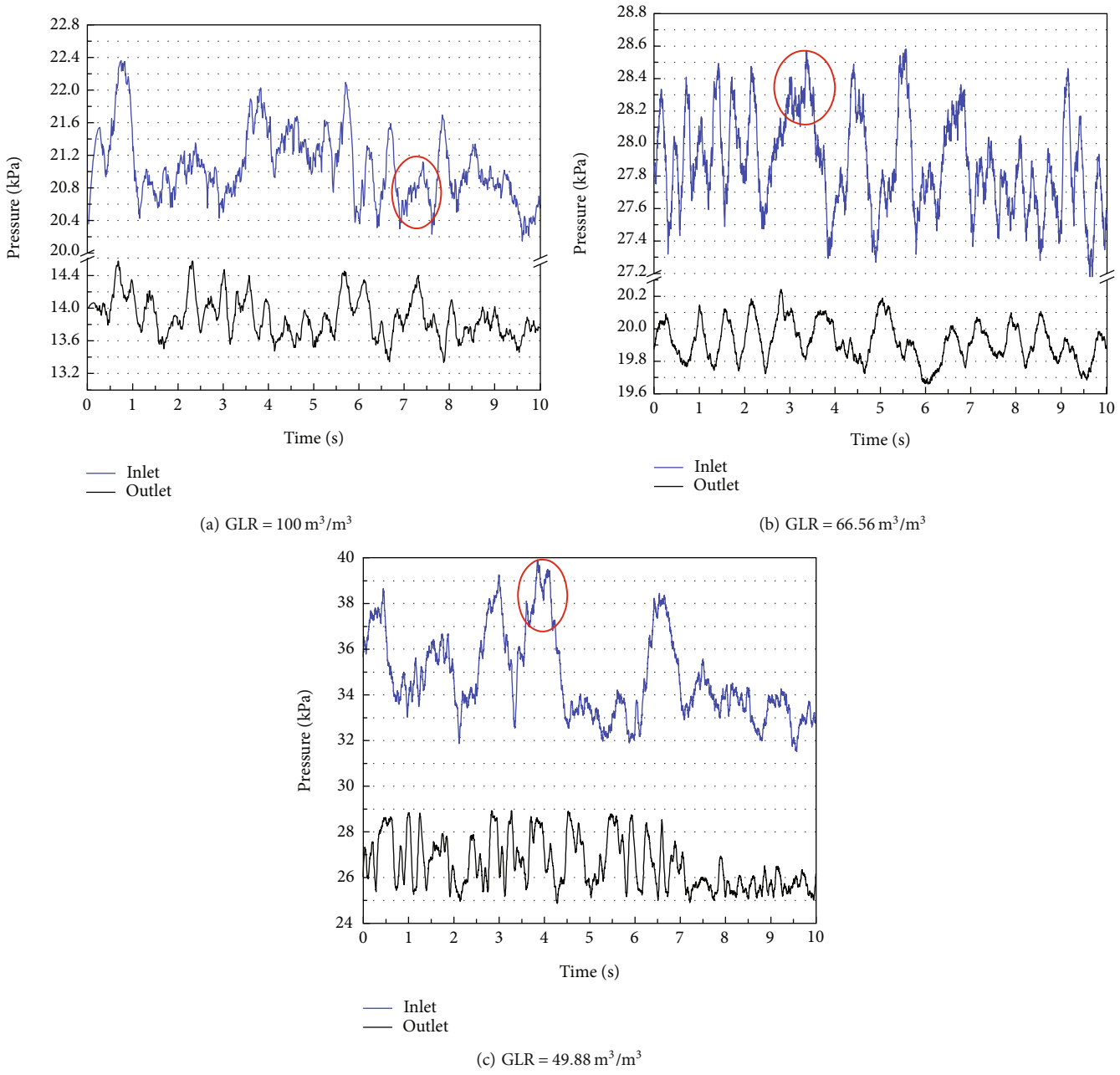

Figure 10: Pressure fluctuation curve of the inlet and outlet with a different gas-liquid ratio.

original direction of advance, the formation of the vortex phenomenon as shown in Figure 8 results in the separation of the boundary layer.

4.4. Pressure Drop Model. Through experiments and simulations, it can be seen that the pressure loss generated by this device mainly comes from the ejector, the inlet of the drainage pipe, the impacting tee, and the heavy pressure drop. The total pressure drop of the slug flow elimination device is

$$\Delta P = \Delta P_o + \Delta P_1 + \Delta P_v + \Delta P_h, \quad (16)$$

where ΔP_o is the pressure drop generated by the impacting tee, kPa. ΔP_1 is the pressure drop generated at the inlet of the drainage pipe, kPa. ΔP_v is the pressure drop generated by the ejector, kPa. ΔP_h is the repositioning pressure difference from the height difference, kPa.

Under the same conditions of the gas flow rate, the total pressure drop increases gradually as the liquid flow rate increases. As Figure 12(a) shows, the liquid-phase flow rate is related to the total pressure drop. According to the study, it is known that the frictional pressure drops upstream and downstream of the Venturi throat are equal under the condition of symmetry between the constriction and expansion sections [28]. In this study, due to the complex structure of the ejector, the differential pressure generated in the convergent section is significantly larger than that in the divergent section (as Figure 12(b)). From Figure 12(b), it can be seen

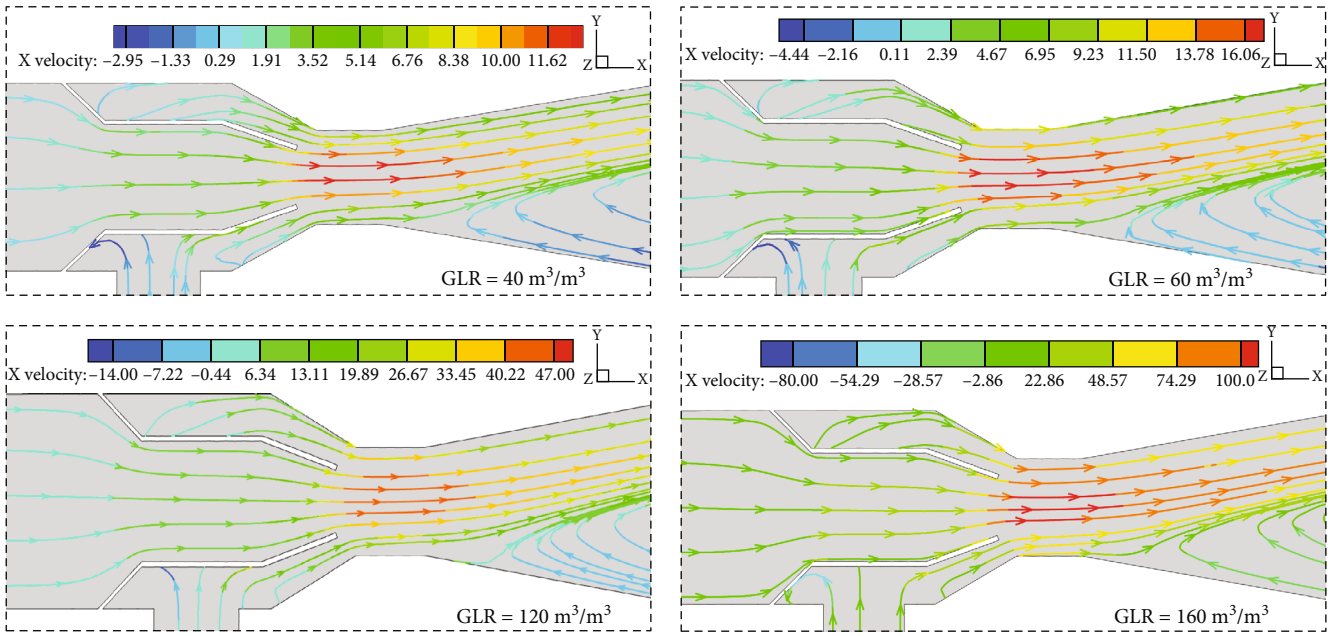

Figure 11: Streamline diagram of the ejector.

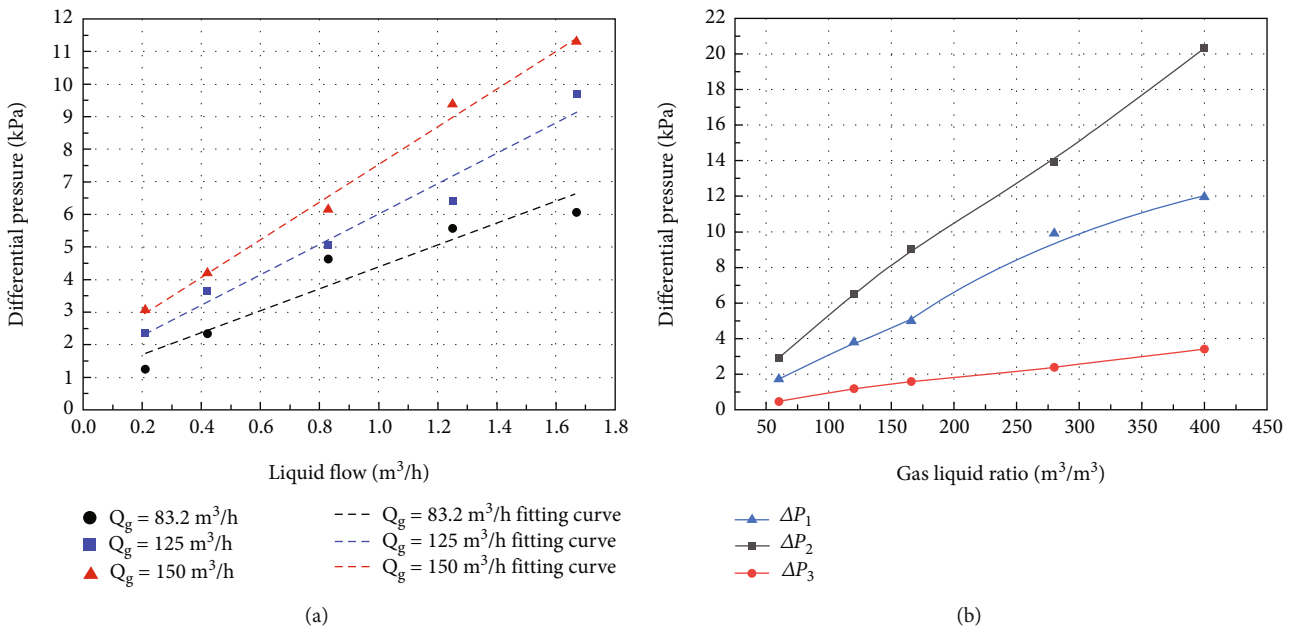

Figure 12: (a) Pressure drop variation at different liquid phase flow conditions; (b) differential pressure variation curves at different cross-sections (ΔP_1 sudden contraction structure, ΔP_2 Venturi-tapering section, ΔP_3 Venturi-expansion section).

that an increase in the gas-liquid ratio leads to a significant increase in the total pressure drop at constant pressure conditions. The differential pressure of the gas-liquid mixture passing through the Venturi nozzle is related to the magnitude of the flow rate and increases with increase of the gas-liquid ratio [29, 30].

4.5. Model Building

4.5.1. Venturi Differential Pressure. Based on the experimental and numerical simulation results, the pressure drop calculation model of this device is established. The pressure drop generated by the Venturi nozzle mainly includes an accelerated pressure drop and friction pressure drop [31]. Among them, the acceleration pressure drop accounts for the largest proportion and increases with the increase of the liquid content. The next is the frictional pressure drop, which is mainly generated at the nozzle. The frictional pressure drop is mainly generated at the nozzle. The frictional pressure drop increases due to the reduction of the flow channel. The experimental and simulation results show that the frictional pressure drop accounts for a small percentage

of the total pressure drop. Based on the installation location of the ejector and the focus of the study, the frictional pressure drop and the repositioning pressure drop are neglected in this calculation.

The accelerated pressure drop in the axial position of the Venturi [32] can be calculated by the following equation.

$$\Delta P_v = \frac{G_m v_{g,th}}{A\varphi} = \Delta P_2 + \Delta P_3, \tag{17}$$

where the gas velocity in the Venturi throat can be expressed as the following equation.

$$v_{g,th} = 0.135 X_{LM} \mathrm{Fr}_g^{1.27} \left(\frac{\rho_l}{\rho_g}\right)^{0.806}, \tag{18}$$

where G_m represents the mass flow rate of the mixture, kg/s; $v_{g,th}$ is the Venturi throat gas velocity, m/s; A represents the cross-sectional area, m^2; φ represents the cross-sectional gas content, dimensionless; and X_{LM} and Fr_g represent the Lockhart-Martinelli number and gas Froude number, respectively, dimensionless.

4.5.2. Differential Pressure of Drainage Pipe Inlet. The pressure drop at the inlet of the drainage pipe is mainly caused by the sudden shrinkage of the pipe diameter, as shown in the structure in Figure 2(c). Therefore, in this study, the pressure drop between section 1 and section 2 is investigated using the pressure drop calculation method of the abruptly shrunken pipe. Due to the small experimental pressure, it is assumed that there is no significant change in the density of the gas-liquid phase and no mass exchange.

The continuity equations for the gas and liquid phases on cross-section 1 and cross-section 2 are obtained from the conservation of mass.

$$G_{gs} = \rho_g A_g v_{gs} = \rho_g A_s \varphi_s, \tag{19}$$

$$G_{ls} = \rho_l A_l v_{ls} = \rho_g v_{ls} A_s (1 - \varphi_s), \tag{20}$$

where G_g and G_l represent the mass flow rate of the gas and liquid, respectively, kg/s; A_g and A_l represent the cross-section of the gas and liquid, respectively, m^2; φ_s represents the gas content of a section, dimensionless; v_{gs} and v_{ls} represent the flow rate of the gas and liquid of a section, respectively, m/s; and s represents any section of section 1 and section 2.

Since the section is very short and friction is neglected, the sum of the external forces on the two gas-liquid phases along the axial direction is $A_2(P_1 - P_2)$; then, the momentum equation is

$$P_1 - P_2 = \frac{1}{A_2}\left(G_{g2} v_{g2} + G_{l2} v_{l2} - G_{g1} v_{g1} - G_{l1} v_{l1}\right). \tag{21}$$

The subscript 1 represents the inlet section of the protruding joint and 2 represents the outlet section of the protruding joint.

From the analysis of simulation results, it is found that the streamline of the gas-liquid mixture is bent downstream of the sudden contraction pipe (Figure 2(c), section t). Therefore, the resistance loss of the sudden contraction pipe is mainly generated from section t to section 2 [33]. Based on the specificity of the structure, it is assumed that the gas content of the drainage pipe is equal to that of section 2; i.e., $\varphi_t = \varphi_2 = \varphi$. From the momentum equation, the pressure drop of the sudden contraction pipe can be calculated as

$$\Delta P_1 = \frac{0.235 G_m}{\rho_l {A_1}^2}\left[\frac{(1-\alpha)^2}{1-\varphi} + \frac{\alpha^2}{\varphi}\frac{\rho_l}{\rho_g}\right], \tag{22}$$

where α is the dryness fraction, dimensionless. G_m is the gas-liquid two-phase mass flow rate, kg/s.

4.5.3. Impacting Tee Differential Pressure. The pressure loss from the impacting tee is calculated according to the following Eq. (23) calculation [34].

$$\Delta P_o = \lambda \frac{{Q_m}^2}{2A^2\rho_l}\left[1 + x\left(\frac{\rho_g}{\rho_l} - 1\right)\right], \tag{23}$$

Where the local resistance factor λ is calculated using the following equation.

$$\lambda = c\lambda_o. \tag{24}$$

The correction factor c is obtained using the empirical equation:

$$c = 1 + 0.75\left[\frac{x(1-x)\left[1 + \rho_l/\rho_g\right]\sqrt{1 - \rho_g/\rho_l}}{1 + x\left(\rho_l/\rho_g - 1\right)}\right]. \tag{25}$$

4.5.4. Heavy Pressure Drop. According to the operating principle of the device, the repositioning pressure drop is mainly generated in the rising pipe section of the drainage pipe and the impacting tee. The calculation equation is

$$\Delta P_h = 2\rho_m g \Delta h. \tag{26}$$

Since the diameter of the drainage pipe is much smaller than the accumulation riser when the gas-liquid mixture enters the drainage pipe, the flow rate of the liquid phase suddenly increases, and when the superficial velocity of the gas-liquid two phases are equal, the slip ratio is 1. Therefore, referring to Eq. (12), the following equation is used to calculate the mixing density.

$$\rho_m = \rho_g \varphi + \rho_l (1 - \varphi). \tag{27}$$

4.6. Accuracy Verification. As per Figure 13(a), it can be seen that under atmospheric conditions, the Venturi nozzle pressure drop has the largest proportion in the total pressure drop, while the heavy pressure drop has the smallest proportion. In small-volume conditions, the pressure drop caused by sudden

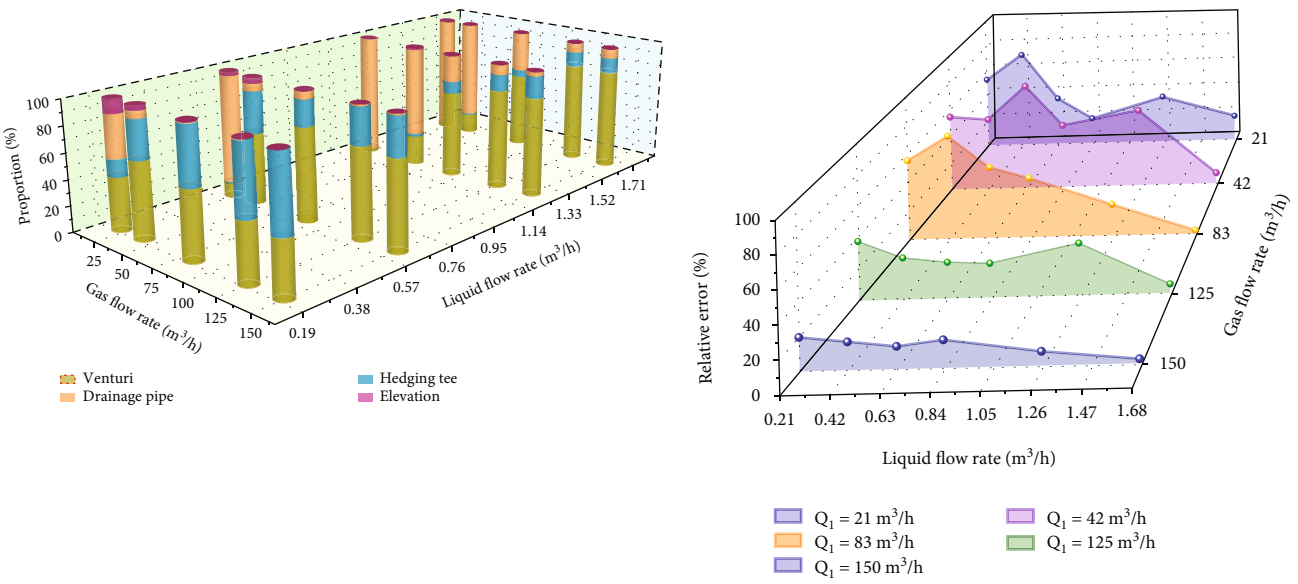

(a) Proportion of local pressure drop

(b) Comparison of pressure drop calculation error

Figure 13: Comparative analysis of the error of pressure drop calculation under different gas-liquid ratio conditions.

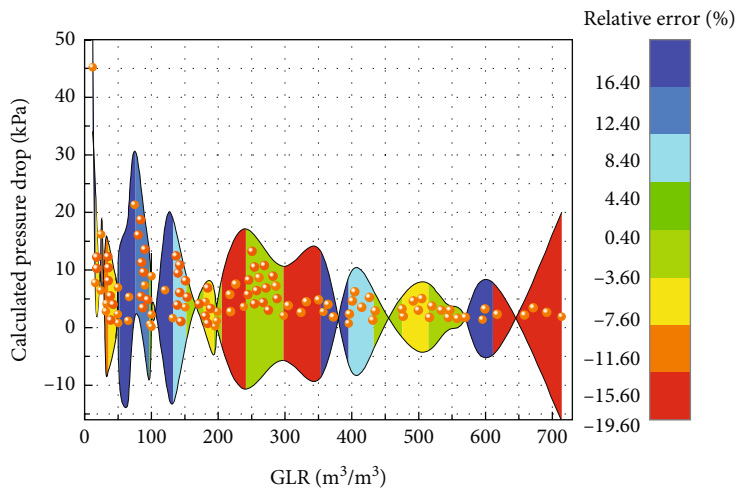

Figure 14: Relative error distribution of pressure drop calculation after correction.

changes in the diameter of the drainage pipe is the largest. The pressure drop of the Venturi nozzle increases with the liquid flow rate, and its average proportion is 52.82% of the total pressure drop. In the large liquid volume and small air volume conditions, the pressure drop at the inlet of the drainage pipe produced a maximum percentage of 95.83%.

According to the calculation results, it can be seen that the pressure drop calculation method obtained from this experiment can truly reflect the motion of the fluid. The error of the pressure drop calculation increases gradually with the decrease in the gas flow rate, as shown in Figure 13(b). The relative error is the smallest when the liquid flow rate is 1.67 m^3/h. As the gas flow rate decreases gradually, the relative error increases gradually. The gas-liquid rate is small, and the liquid phase is mostly deposited at the bottom of the accumulation riser due to gravity. As shown in Figure 7(c), the liquid level is higher than the inlet of the drainage pipe. The height difference of the liquid level provides energy for the liquid movement, and the gravitational potential energy is ignored in the calculation. This is the main reason for the large calculation results and the large error in the total pressure drop. When the gas flow rate increases, the Venturi produces a larger proportion of the pressure drop. The calculation accuracy of the total pressure drop depends on the Venturi nozzle. Under a large gas flow rate, the flow rate at the Venturi nozzle changes little, the measured results match the calculated results to a high coincidence, and the calculation error is small.

4.7. Model Correction. To further improve the calculation accuracy of the pressure drop under different gas-liquid ratios, the total pressure drop calculation method of the slug

flow elimination device is optimized based on the pressure drop ratio of different structures. The modified pressure drop calculation method is obtained as follows.

$$\Delta P = 0.804 + 0.957(\Delta P_o + \Delta P_1 + \Delta P_h) + 0.421\Delta P_v{}^{1.5}. \quad (28)$$

As Figure 14 shows, the pressure drop gradually decreases as the gas-liquid ratio increases. The accuracy of the modified pressure drop calculation method is significantly improved, and the error with the measured pressure drop is kept within 20%, among which 69.31% of the data points are within 10%.

5. Conclusion

According to the motion law of slug flow, the elimination device designed based on the kinetic energy conversion method can better solve the problem of large pressure fluctuations caused by slug flow. In this study, the flow field of the slug flow through the elimination device is analyzed. The energy losses generated during the operation of the device are evaluated. A pressure drop calculation method for this device is developed based on the share of different structures in the total pressure drop. The relative error of the pressure drop model is controlled within 20%, which meets the process production requirements. The optimal and most economical operating range of the device is to maintain the gas-liquid ratio within 120 m^3/m^3 (under operating conditions). The device can provide stable flow patterns and pressure conditions for gas-liquid two-phase flow measurements for the oil well.

Data Availability

Data can be obtained by contacting the corresponding author (Xingkai Zhang, zhangxingkai001@163.com).

Conflicts of Interest

The authors declare that they have no conflicts of interest.

Acknowledgments

The authors would like to acknowledge the support provided by the National Natural Science Foundation of China (Grant No: 62173049) and the open fund of the Key Laboratory of Exploration Technologies for Oil and Gas Resources (Yangtze University), Ministry of Education of China (Grant: K2021-17).

References

[1] H. L. Xue, X. Y. He, and H. J. Sun, "Research and application of flow type adjuster in multiphase metering system," *Instrumentation User*, vol. 47, 2018(09),39-40+44.

[2] A. Sqw, A. Kwx, and B. Hbka, "Slug flow identification using ultrasound doppler velocimetry - Science Direct," *International Journal of Heat and Mass Transfer*, vol. 148, 2019.

[3] K. Ran, K. Seungjin, B. Stephen, T. Kirk, and H. Chris, "Experimental investigation of horizontal air-water bubbly-to-slug and bubbly-to-slug transition flows in a 3.81 cm ID pipe," *International Journal of Multiphase Flow*, vol. 94, pp. 137–155, 2017.

[4] R. Deendarlianto, W. Andinusa, D. Arif, and W. A. Okto, "Experimental study on the hydrodynamic behavior of gas-liquid air-water two-phase flow near the transition to slug flow in horizontal pipes," *International Journal of Heat and Mass Transfer*, vol. 130, pp. 187–203, 2019.

[5] B. D. Woods, Z. Fan, and T. J. Hanratty, "Frequency and development of slugs in a horizontal pipe at large liquid flows," *International Journal of Multiphase Flow*, vol. 32, no. 8, pp. 902–925, 2006.

[6] T. K. Mandal, G. Das, and P. K. Das, "An appraisal of liquid-liquid slug flow in different pipe orientations," *International Journal of Multiphase Flow*, vol. 36, no. 8, pp. 661–671, 2010.

[7] Y. F. Meng, X. K. Zhang, R. Q. Liao, and D. Wang, "A two-parameter measurement method for moisture with the application of forced annular flow," *Journal of Xi'an Jiaotong University*, vol. 54, no. 10, p. 9, 2020.

[8] W. Zheng, R. Liang, X. Zhang, R. Liao, D. Wang, and L. Huang, "Wet gas measurements of long-throat Venturi tube based on forced annular flow," *Flow Measurement and Instrumentation*, vol. 81, p. 102037, 2021.

[9] B. T. Yocum, *Offshore riser slug flow avoidance: mathematical models for design and optimization*, SPE European Meeting. OnePetro, London, United Kingdom, 1973.

[10] L. Xing, H. Yeung, J. Shen, and Y. Cao, "A new flow conditioner for mitigating severe slugging in pipeline/riser system," *International Journal of Multiphase Flow*, vol. 51, pp. 65–72, 2013.

[11] P. Prickaerts, G. Haandrikman, and R. Henkes, "Two-phase flow behavior for a single flow pipe with a non-symmetric splitter to a dual riser," in *16th International Conference on Multiphase Production Technology*, BHR Group, Cannes, France, 2013.

[12] S. Cem and J. Tengesdal, "A new technique to eliminate severe slugging in pipeline/riser systems," in *Society of Petroleum Engineers SPE Annual Technical Conference and Exhibition - proceedings of SPE annual technical conference and exhibition*, pp. 633–641, USA, 2000.

[13] E. Schrama, R. Fernandes, and BHR Group, "The bubble breaker: breaking up slug flow into dispersed bubbly flow using a passive mechanical device," in *12th International Conference on Multiphase Production Technology*, pp. 283–296, Barcelonna, Spain, 2005.

[14] J.-X. Zhang, J.-Y. Zhang, Y. Zhou, Z.-Y.-Y. Cheng, and G.-D. Cao, "Investigation on the performance of a helico-axial multiphase pump under slug flow," *Petroleum Science*, vol. 19, no. 4, pp. 1812–1824, 2022.

[15] W. Schiferli, J. H. Hansen, B. J. Brasjen, and S. Belfroid, *Experimental Investigation of Terrain Slugging: Formation Mechanism and Potential Mitigation Methods*, TNO, 2013.

[16] N. Echebarrena, P. D. Mininni, and G. A. Moreno, "Empirical mode decomposition of multiphase flows in porous media: characteristic scales and speed of convergence," *Petroleum Science*, vol. 17, no. 1, pp. 153–167, 2020.

[17] A. B. Ehinmowo, O. O. Ogunleye, and O. D. Orodu, "Experimental investigation of hydrodynamic slug mitigation potential of an intermittent absorber," *Chemical Engineering Research and Design*, vol. 113, pp. 50–60, 2016.

[18] L. Xiaoming, *Study on Flow Characteristics of Gas-Liquid Two-Phase and Oil-Gas-Water Three-Phase Section Slug Flow*, China University of Petroleum (East China), Shandong, 2007.

[19] S. Mo, A. Ashrafian, J.-C. Barbier, and S. T. Johansen, "Quasi-3D modelling of two-phase slug flow in pipes," *The Journal of Computational Multiphase Flows*, vol. 6, no. 1, pp. 1–12, 2014.

[20] S. T. Johansen, S. Mo, E. Meese, J. Oliveira, J. Reyes, and J. Carneiro, "CFD simulations of multiphase flows containing large scale interfaces and dispersed phases with selected production technology applications," in *Offshore Technology Conference*, pp. 2076–2090, Brasil-Rio de Janeiro, Brazil, 2015.

[21] L. Hongqi, *Theory and Application of Spraying Technology*, Wuhan University Press, Wuhan, 2004.

[22] Z.-K. Gao, M.-X. Liu, W.-D. Dang, and Q. Cai, "A novel complex network-based deep learning method for characterizing gas–liquid two-phase flow," *Petroleum Science*, vol. 18, 2021.

[23] G. A. Gregory, "Comments on the prediction of liquid holdup for gas-liquid flow in inclined pipes," *The Canadian Journal of Chemical Engineering*, vol. 52, 1974.

[24] Y. Taitel and A. E. Dukler, "A model for predicting flow regime transitions in horizontal and near horizontal gas-liquid flow," *AICHE Journal*, vol. 22, no. 1, pp. 47–55, 1976.

[25] Z. Wang, W. Luo, R. Liao, X. Xie, F. Han, and H. Wang, "Slug flow characteristics in inclined and vertical channels," *Fluid Dynamics & Materials Processing*, vol. 15, no. 5, p. 13, 2019.

[26] D. Meng, N. D. Jin, Z. K. Gao, Z. Y. Wang, and L. S. Zhai, "Flow pattern and water holdup measurements of vertical upward oil-water two-phase flow in small diameter pipes," *Multiphase Flow*, vol. 41, pp. 91–105, 2012.

[27] G. A. Gregory, M. K. Nicholson, and K. Aziz, "Correlation of the liquid volume fraction in the slug for horizontal gas-liquid slug flow," *International Journal of Multiphase Flow*, vol. 4, no. 1, pp. 33–39, 1978.

[28] L. D. Fang, T. Zhang, and Y. Xu, "Slit Venturi-based gas-liquid two-phase flow measurement," *Journal of Sensing Technology*, vol. 8, pp. 1458–1465, 2008.

[29] F. Al-Ruhaimani, E. Pereyra, C. Sarica, E. Al-Safran, S. Chung, and C. Torres, "A study on the effect of high liquid viscosity on slug flow characteristics in upward vertical flow," *Journal of Petroleum Science & Engineering*, vol. 161, pp. 128–146, 2018.

[30] M. O. Elobeid, A. Ahmad, A. Al-Sarkhi et al., "Pressure drop measurements in Venturi meters of different beta ratios for oil-water flow experiments," *Arabian Journal for Science and Engineering*, vol. 43, no. 11, pp. 6355–6374, 2018.

[31] Y. Xu, Y. D. Wang, T. Zhang, and J. H. Wang, "Moisture flow characteristics and structural optimization of Venturi expansion section," *Mechanical Science and Technology*, vol. 37, no. 8, pp. 1272–1279, 2018.

[32] J. Wang, Y. Xu, T. Zhang, H. Wu, and X. Huo, "A pressure drop model for the annular-mist flow in vertical Venturi," *Journal of Natural Gas Science and Engineering*, vol. 76, pp. 103168–103168, 2020.

[33] J.-L. Chen, *Petroleum Gas-Liquid Two-Phase Pipe Flow*, Petroleum Industry Press, 1989.

[34] C.-J. Li and W.-L. Jia, *Multiphase Flow in Oil and Gas Pipes*, Chemical Industry Press, 2015.